



HAL
open science

Electron microscopy contribution in the comprehension of interaction mechanisms between nanoparticles and biological cells

Wael Rima

► **To cite this version:**

Wael Rima. Electron microscopy contribution in the comprehension of interaction mechanisms between nanoparticles and biological cells. Other. INSA de Lyon, 2012. English. NNT : 2012ISAL0131 . tel-00876351

HAL Id: tel-00876351

<https://theses.hal.science/tel-00876351>

Submitted on 24 Oct 2013

HAL is a multi-disciplinary open access archive for the deposit and dissemination of scientific research documents, whether they are published or not. The documents may come from teaching and research institutions in France or abroad, or from public or private research centers.

L'archive ouverte pluridisciplinaire **HAL**, est destinée au dépôt et à la diffusion de documents scientifiques de niveau recherche, publiés ou non, émanant des établissements d'enseignement et de recherche français ou étrangers, des laboratoires publics ou privés.

Apport de la Microscopie Electronique dans la Compréhension des Mécanismes d'Interactions entre Nanoparticules et Cellules Biologiques

Electron Microscopy Contribution in the Comprehension of Interaction Mechanisms
between Nanoparticles and Biological Cells

Thèse présentée devant
L'Institut National des Sciences Appliquées de Lyon

Pour obtenir
Le grade de Docteur
École Doctorale Matériaux de Lyon

Par
Wael RIMA
(Ingénieur)

Jury

BEGIN-COLIN Sylvie	IPCMS Strasbourg	Professeur	Rapporteur
MILLOT Nadine	ICB Dijon	Professeur	Rapporteur
RODRIGUEZ-LAFRASSE Claire	Faculté de Médecine Lyon-Sud	Professeur	Examineur
ROUX Stéphane	UTINAM Besançon	Professeur	Examineur
TILLEMENT Olivier	LPCML Lyon	Professeur	Examineur
PERRIAT Pascal	INSA Lyon	Professeur	Directeur thèse
JOLY-POTTUZ Lucile	INSA Lyon	M.C.F.	Directrice thèse
POURCHEZ Jérémie	ENSM Saint Etienne	C.R.	Directeur thèse
ALOY Marie-Thérèse	Faculté de Médecine Lyon-Sud	I.R.	Membre invité
BURDIN Béatrice	CTμ Lyon	I.R.	Membre invité
LUX François	LPCML Lyon	M.C.F.	Membre invité
SANCEY Lucie	LPCML Lyon	C.R.	Membre invité

Laboratoire de recherche: MATEIS, INSA-Lyon

Axe Principal de Recherche

Résumé

L'objet de cette thèse concerne l'étude à l'échelle microscopique des interactions de **nanoparticules** à visée thérapeutique avec les cellules et les tissus biologiques. Précisément, il s'agit de fournir des caractérisations de ces interactions en utilisant principalement les différentes techniques d'imagerie et de spectroscopie de la **microscopie électronique**.

Parmi les nanoparticules aptes à accompagner la radiothérapie en clinique, les nanoparticules à base d'oxyde de **gadolinium** paraissent pertinentes, de part leur multimodalité en imagerie et leur effet radiosensibilisant prouvé *in vitro* et *in vivo*.

Cet effet de **radiosensibilisation** est exceptionnel notamment sur des cellules cancéreuses radiorésistantes de la lignée SQ20B (carcinome squameux tête et cou) et uniquement pour des doses modérées de nanoparticules (aux alentours de 0.6 mM en Gd). Pour parfaire la compréhension de ce phénomène, l'étude *in vitro* à l'échelle microscopique (échelle peu exploitée en biologie) des **mécanismes d'internalisation** des particules de gadolinium dans les cellules SQ20B a été nécessaire. Cette étude a constitué la partie principale de ce travail. En particulier, nous avons montré grâce aux clichés de microscopie électronique que ce maximum de radiosensibilisation est dû à une internalisation maximale des particules dans le cytoplasme, notamment par **macropinocytose**. Ce mécanisme d'internalisation est caractérisé par la formation de vésicules de grandes tailles, ou macropinosomes. Il se produit suivant deux étapes : la formation d'agglomérats de nanoparticules à proximité de la membrane cellulaire puis la récupération de ceux-ci par les lamellipodes de la cellule. La première étape est fortement dépendante des caractéristiques physicochimiques des particules, plus particulièrement leur potentiel zêta qui détermine la taille de l'agglomérat, et de la distance les séparant de la cellule. Dans des gammes de taille et de distance à la membrane optimales aux concentrations modérées, l'agglomérat peut être récupéré par les lamellipodes de la cellule. Il s'en suit une protubérance sur la membrane plasmique formant un macropinosome contenant les agglomérats de nanoparticules. Cet endosome précoce suivra ensuite le schéma d'endocytose classique dans le cytoplasme en fusionnant avec des corps multivésiculaires, uniquement visible en microscopie électronique à transmission, pouvant contenir des enzymes de dégradation détruisant leur contenu. Ces enzymes rendent le pH acide à l'intérieur de la vésicule. Plus les nanoparticules sont proches du noyau cellulaire plus leur effet radiosensibilisant sera efficace. Les espèces oxygénées réactives (ROS) et les électrons Auger et secondaires peuvent atteindre l'ADN du noyau plus facilement. A faibles doses (< 0.4 mM) très peu de nanoparticules sont internalisées et un effet linéaire de la radiosensibilisation est observé jusqu'à 0.6 mM. A fortes doses (> 0.7 mM) les nanoparticules forment une couronne autour de la membrane cellulaire agissant comme écran, empêchant ainsi les ROS et les électrons générés de pouvoir atteindre l'ADN et induire des cassures, le noyau étant situé à quelques micromètres de la membrane cellulaire.

Les résultats obtenus posent des challenges intéressants quant à l'utilisation clinique des nanoparticules à base d'oxyde de gadolinium. Ils ouvrent la voie sur la nécessité de contrôler leur internalisation cellulaire en contrôlant leur chimie, laissant envisager ainsi des opportunités prometteuses dans le domaine de la **radiothérapie assistée par nanoparticules** délivrant de faibles doses de radiation aux patients.

Abstract

Over the last few decades, **nanoparticles** have been studied in theranostic field with the objective of exhibiting a long circulation time through the body coupled to major accumulation in tumor tissues, rapid elimination, therapeutic potential and contrast properties. In this context, sub-5 nm **gadolinium**-based nanoparticles (GBNs) were developed for imaging-guided radiotherapy. These particles possess an *in vitro* efficient **radiosensitizing effect** even at moderate concentration when incubated with head and neck squamous cell carcinoma cells (SQ20B). To further understand this phenomenon and optimize it, we use diverse types of microscopy techniques, in particular **electron microscopy** that possesses a resolution sufficient to determine the mechanisms responsible for particle uptake. Two main cellular **internalization mechanisms** were then evidenced and quantified: passive diffusion and **macropinocytosis**. Whereas the amount of particles internalized by passive diffusion is not completely sufficient to induce, *in vitro*, a significant radiosensitizing effect, the cellular uptake by macropinocytosis, which is only significant in a limited range of GBNs incubation concentration, may lead to a successful radiotherapy. Macropinocytosis processes in two steps: formation of agglomerates at vicinity of the cell followed by recuperation of the agglomerate by the lamellipodia (i.e. the “arms”) of the cell. The first step is strongly dependent on the physicochemical characteristics of the particles, especially their zeta potential that determines the size of the agglomerates and their distance from the cell, which are the parameters that render possible their collect *via* the lamellipodia. These results pose interesting challenges for clinical use of GBNs. They emphasize on the importance of the quantity of particles internalized in the cell and the localization of particles within the cytoplasm, promising thus ambitious opportunities towards a **particle-assisted radiotherapy** using lower doses of radiation.

Résumé de Thèse en Français

Les matériaux nanostructurés sont de plus en plus utilisés aussi bien en recherche pour l'élaboration de matériaux innovants qu'en applications médicales à aboutissements cliniques. Ils posent de ce fait une problématique nouvelle : leur interaction avec le vivant. En effet, ces matériaux aux propriétés inimaginables il y a encore quelques années, sont capables d'interagir, à une échelle similaire, avec des entités biologiques.

Cette thèse inscrite dans le cadre de plusieurs projets pluridisciplinaires centrés sur l'étude des interactions nanoparticules/vivant, vise à fournir une caractérisation de ces interactions, particulièrement à l'échelle nanométrique, grâce aux différentes possibilités d'imagerie et de spectrométrie de la microscopie électronique. Cette technique implique l'utilisation d'une source d'électrons accélérés sous vide qui interagit avec l'échantillon à analyser. Les signaux issus des interactions électrons matière sont ensuite utilisés pour imager l'échantillon, l'analyser chimiquement ou explorer sa structure. Selon l'échelle et la nature de l'information souhaitée, on utilisera la microscopie électronique à balayage MEB (topographie, morphologie) et/ou la microscopie électronique à transmission MET (structure, composition chimique). Cette approche permet d'identifier les nanoparticules, de visualiser leur éventuel état d'agglomération sur la membrane cellulaire et de détecter précisément leur localisation dans le cytoplasme des cellules et dans les tissus, ce qui est complémentaire avec d'autres techniques d'imagerie telle que la microscopie confocale, limitée en résolution. Cette localisation et ses propriétés fournissent également des informations précieuses sur le mode d'entrée des nanoparticules dans les cellules. Mais le vide en microscopie électronique classique ne permet pas l'observation directe d'échantillons hydratés, en particulier les matériaux biologiques. Ils devront donc être préalablement fixés et déshydratés, avant d'être inclus dans la résine (EPON) et coupés en sections ultrafines par ultramicrotomie. Toutes ces étapes doivent être accomplies avec soin afin d'éviter des artefacts de préparation et/ou la destruction de l'ultrastructure du matériau biologique étudié.

Nous avons porté notre attention sur deux aspects touchant aux interactions nanoparticules/vivant : en oncologie, où le contact des nanoparticules avec les cellules et les tissus est volontaire dans la perspective de mieux diagnostiquer et soigner le cancer, et en risques sanitaires où l'inhalation involontaire des nanoparticules impose l'évaluation de leur toxicité.

Deux types de nanoparticules ont été principalement utilisés suivant l'application souhaitée :

(1) les nanoparticules d'oxyde de gadolinium de taille inférieure à 5 nm pour le diagnostic et le traitement du cancer, *in vitro* et *in vivo*, et pour l'étude *in vitro* des mécanismes d'internalisation dans les cellules cancéreuses radio-résistantes,

(2) les nanoparticules de silice de tailles différentes avec une fonctionnalisation de surface identique pour étudier, *in vitro*, l'effet du paramètre taille sur la toxicité et l'internalisation dans des macrophages murins. Une variante des nanoparticules de silice consistant à leur inclure un cœur d'or a également été utilisée pour améliorer la détection *in vivo* du cancer colorectal chez l'homme.

Dans le cas de l'étude des mécanismes d'internalisation, les nanoparticules à base d'oxyde de gadolinium développées pour la radiothérapie guidée par l'imagerie, possèdent un effet significatif de radiosensibilisation *in vitro*, même à concentration modérée, lorsqu'elles sont incubées avec des cellules cancéreuses tête et cou (carcinome épidermoïde, lignée SQ20B) (**Figure 1**).

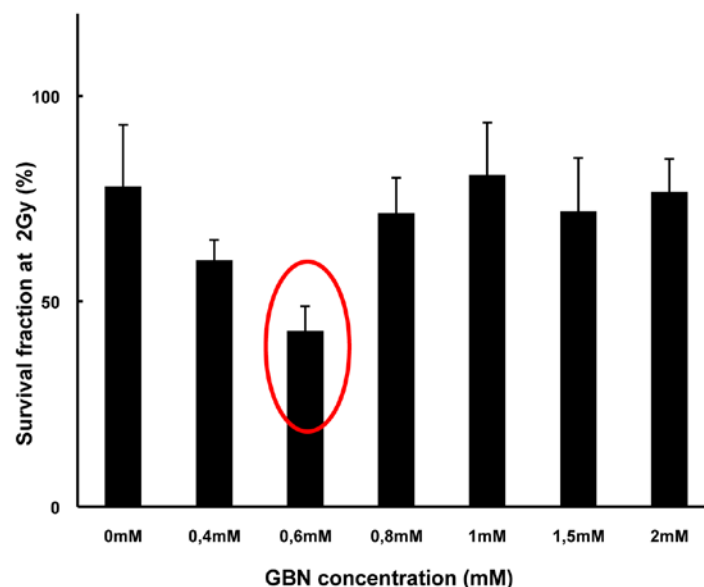


Figure 1: Pourcentage de fraction de survie de cellules radio-résistantes de la lignée SQ20B déterminé par test de clonogénicité après irradiation à 2 Gy pour différentes concentrations d'incubation en nanoparticules à base d'oxyde de gadolinium.

Pour comprendre plus profondément ce phénomène et l'optimiser, nous avons utilisé diverses techniques de microscopie et en particulier la microscopie électronique. Cette dernière possède une résolution suffisamment élevée pour déterminer les mécanismes responsables de

l'internalisation des particules. Deux principaux mécanismes d'internalisation cellulaire ont alors été observés puis étudiés : la macropinocytose et la diffusion passive. Considérant que la quantité de particules internalisées par diffusion passive ne suffit pas à induire un effet radiosensibilisant satisfaisant *in vitro*, l'internalisation par macropinocytose, significative seulement dans une gamme limitée de concentrations en nanoparticules, pourrait participer à la réussite de la radiothérapie. La macropinocytose se produit après la formation d'agglomérats de nanoparticules à proximité de la cellule suivie de la récupération de l'agglomérat par les lamellipodes (i.e. les "bras") de la cellule (**Figure 2**).

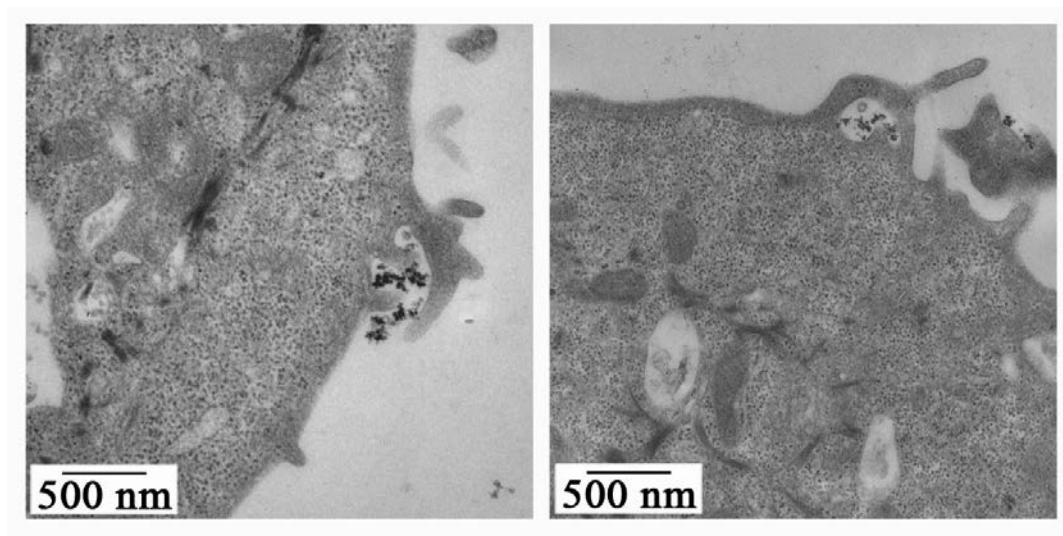


Figure 2: Clichés de microscopie électronique à transmission de coupe ultramicrotomique d'une cellule de la lignée SQ20B internalisant des nanoparticules à base d'oxyde de gadolinium par macropinocytose. Figure de gauche: soulèvement et pliage d'une lamellipode formant un début de protubérance circulaire (ou courbée) contenant les nanoparticules. Figure de droite: protubérance après effondrement de la lamellipode sur la membrane plasmique formant une vésicule (macropinosome précoce) qui fusionnera avec la membrane afin de pénétrer dans le cytoplasme.

La première étape est fortement dépendante des caractéristiques physico-chimiques des particules, en particulier leur potentiel zêta qui détermine la taille des agglomérats et leur distance de la cellule. Ces résultats proposent des défis intéressants pour envisager un usage clinique des nanoparticules à base de gadolinium. En contrôlant leur chimie, il est possible de maîtriser la quantité de particules internalisées dans le cytoplasme cellulaire. Ce contrôle de l'internalisation cellulaire par la concentration et le temps d'incubation des nanoparticules avec les cellules ouvre des perspectives prometteuses à l'égard d'une radiothérapie assistée par nanoparticules. Ceci permettrait une réduction de la dose d'irradiation délivrée au patient.

Les caractéristiques physico-chimiques des nanoparticules peuvent non seulement jouer un rôle important dans leurs mécanismes d'internalisation dans les cellules, mais également

déterminer leurs niveaux de toxicité. Dans le cadre d'une collaboration avec l'Ecole des Mines de Saint Etienne (thèse Lara Leclerc), une étude a été initiée afin de déterminer l'impact de la taille sur l'internalisation cellulaire et l'activité biologique. Les nanoparticules utilisées sont des billes de silice fabriquées par la société Nano-H. Elles sont fluorescentes et possèdent des tailles submicroniques variables (850, 500, 250 et 150 nm) avec une fonctionnalisation de surface unique (COOH). Après une caractérisation complète des particules, elles ont été incubées avec des macrophages, les principales cellules cibles de l'appareil respiratoire, responsables de la phagocytose des particules, de la lignée RAW 264.7. Les particules ont facilement été visualisées dans le cytoplasme des macrophages par MET (**Figure 3**) et microscopie confocale.

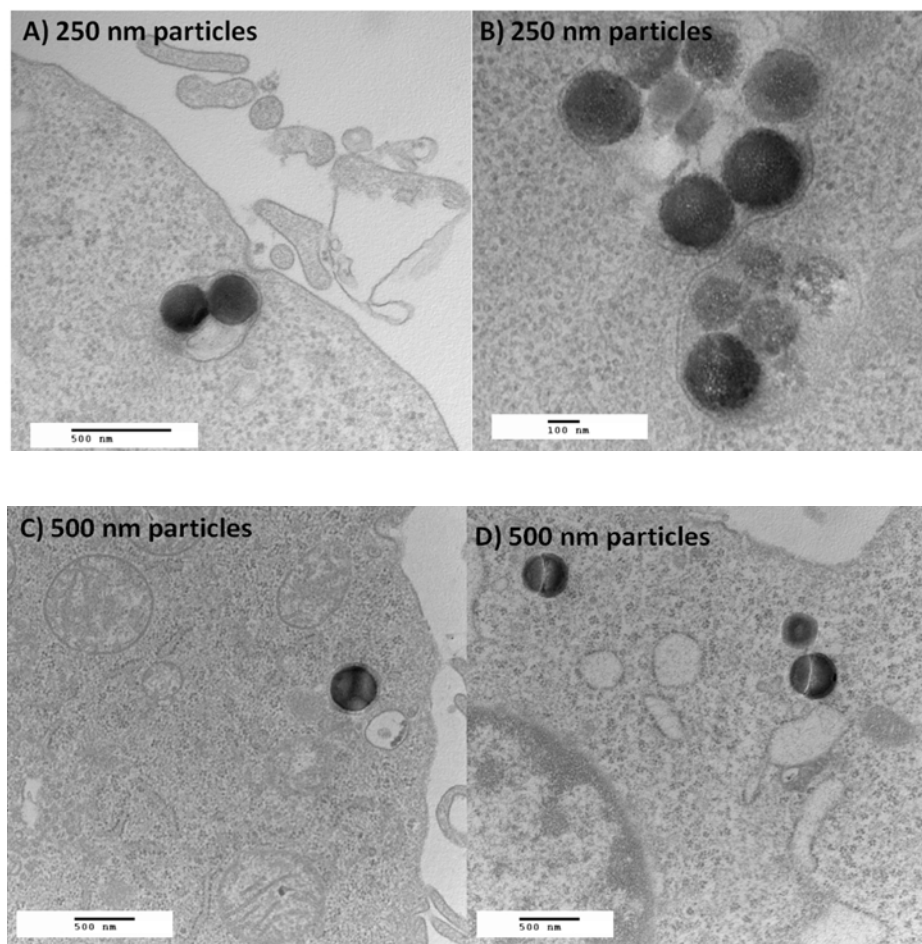


Figure 3: Clichés de microscopie électronique à transmission des particules de silice de 250 nm (A-B) et de 500 nm (C-D) de taille après leur internalisation dans des macrophages de la lignée RAW 264.7. Les images montrent les particules présentes dans des vacuoles à double membrane dans le cytoplasme cellulaire. Les particules de 500 nm de taille semblent être internalisées d'une manière individuelle tandis que celles de 250 nm de taille sont souvent internalisées par groupe dans une même vésicule.

Après ces observations, une évaluation quantitative de l'internalisation a été réalisée. La fluorescence détectée après une extinction avec du bleu trypan nous a permis de distinguer et

de quantifier les particules réellement internalisées de celles adhérentes à la membrane cellulaire. Ces données ont enfin été comparées à la toxicité *in vitro* et évaluées en termes de dommages aux cellules, d'inflammation et de stress oxydatif (évaluation par libération de lactate déshydrogénase LDH, Tumor Necrosis Factor TNF- α et production de ROS, respectivement). Ces travaux nous ont permis de souligner que les nanoparticules de plus petite taille (150 nm) sont plus internalisées pour la dose employée de 1000 nanoparticules/cellule. Aucune relation directe entre l'internalisation cellulaire des nanoparticules et les données biologiques de toxicité n'a été observée d'une manière significative.

L'objectif final étant de proposer les nanoparticules sur le marché comme un produit possédant une activité pharmacologique, les tests *in vitro* utiles et nécessaires deviennent vite insuffisants. En effet, la culture cellulaire, facile à mettre en œuvre avec un matériel standardisé, peut constituer un avantage lorsqu'il s'agit d'isoler un phénomène ou d'expliquer un mécanisme d'action. Et bien que l'utilisation de cellules humaines à moindre coût soit possible sans se soucier des barrières inter-espèces, la complexité des modèles, les problèmes techniques (milieu de culture, contaminants biologiques, Sérum de Veau Fœtal SVF) ainsi que l'utilisation d'une monocouche de cellule d'un même type, constituent entre autres des limites importantes au modèle *in vitro*. Les cellules en culture ne sont pas représentatives de la complexité de l'organisation du vivant dans sa globalité. L'expérimentation animale (principalement sur les rongeurs), dernière étape avant les essais cliniques sur l'homme, reste indispensable pour comprendre les mécanismes intimes qui régissent le fonctionnement des organes et des tissus en contact des nanoparticules.

Dans cette perspective, deux études *in vivo* ont impliqué l'utilisation des nanoparticules de gadolinium et de silice. L'exploitation du contraste positif induit en IRM par les nanoparticules de gadolinium et leur effet radiosensibilisant a conduit à une augmentation de la durée de vie de rats porteurs de tumeur de cerveau (gliosarcome). L'effet radiosensibilisant des nanoparticules de gadolinium peut être activé par les microfaisceaux de rayons X (délivrés par le synchrotron, ESRF) quand le gadolinium est en quantité suffisante dans la tumeur et en faible quantité dans le tissu sain environnant. A l'échelle microscopique, après perfusion de l'animal avec un fixateur (glutaraldéhyde) et préparation des morceaux de cerveaux prélevés pour la MET, il était très difficile de repérer les nanoparticules dans les coupes de cerveaux inclus dans de la résine. Après l'observation d'un grand nombre de

coupes de tumeur contenant des nanoparticules, deux hypothèses ont été émises : soit (i) les nanoparticules sont présentes mais elles ne sont pas agglomérées (comme c'est le cas *in vitro*) ce qui rend leur détection en MET quasiment impossible, soit (ii) les nanoparticules ont été éliminées lors des étapes de lavage de l'animal avant sa perfusion. Cette étude est toujours en cours. Une des perspectives serait de prélever la tumeur du cerveau et de la fixer par immersion sans lavage. Ceci permettrait d'augmenter les chances d'observer les particules dans le cerveau en MET même si la structure de ce dernier n'est pas aussi bien conservée qu'avec une fixation par perfusion.

En ce qui concerne les nanoparticules de silice à cœur d'or, une variante des nanoparticules de silice permettant le renforcement de leur signal de fluorescence, elles ont été pulvérisées *ex vivo* sur des pièces anatomiques de colon prélevées sur des patients souffrant d'un adénocarcinome. Les prélèvements ont été préparés pour la microscopie électronique. Les observations au MEB après abrasion ionique au FIB (Focused Ion Beam) des blocs de résine imprégnant les pièces de colon contenant les nanoparticules fonctionnalisées de 40 nm de taille ont montré que ces nanoparticules seraient accumulées préférentiellement sur les zones tissulaires cancéreuses. Les nanoparticules seraient visibles dans les microvillosités de l'intestin sans pour autant s'internaliser dans les cellules. Ces observations confirment les résultats obtenus en fluorescence par sonde Fluobeam pour ces nanoparticules destinées à guider le chirurgien dans son choix d'élimination des zones cancéreuses de l'intestin. L'abrasion par FIB a permis de s'affranchir de l'ultramicrotomie et l'observation au MEB basse tension a permis de s'affranchir des étapes de contraste à l'acétate d'uranyle et au citrate de plomb. Ces métaux lourds rendaient très difficile l'interprétation des clichés MET classique et le repérage des nanoparticules sur le tissu. L'or, le plomb et l'uranium présentent un contraste similaire sous le faisceau d'électrons.

Ces observations systématiques par microscopie électronique des interactions nanoparticules/vivant contribuent, de façon majeure, à l'avancée des recherches en nanomédecine et nanotoxicologie, et confirment la pertinence de cette technique dans ce type d'étude. L'imagerie par microscopie électronique fournit des caractérisations fines importantes non seulement pour mieux comprendre et mieux maîtriser l'internalisation des nanoparticules et leur trafic intracellulaire mais également pour améliorer leur synthèse et leur caractéristiques physico-chimiques, les rendant de plus en plus aptes aux applications cliniques.

List of Papers

This thesis is based on following publications:

1. **W. Rima**, L. Sancey, L. Joly-Pottuz, P. Perriat, G.B. Alcantara, “Uptake of Therapeutic Nanoparticles into Cells: Review”, **2012**, draft.
2. **W. Rima**, L. Sancey, M. T. Aloy, E. Armandy, G. B. Alcantara, T. Epicier, A. Malchère, L. Joly-Pottuz, P. Mowat, F. Lux, O. Tillement, B. Burdin, A. Rivoire, C. Boulé, I. Anselme-Bertrand, J. Pourchez, M. Cottier, S. Roux, C. Rodriguez-Lafrasse, P. Perriat, “Internalization Pathways of Gadolinium-Based Radiosensitizing Nanoparticles into Cancer Cells”, **2012**, submitted.
3. P. Mowat, A. Mignot, **W. Rima**, F. Lux, O. Tillement, C. Roulin, M. Dutreix, D. Bechet, S. Huger, L. Humbert, M. Barberi-Heyob, M.T. Aloy, E. Armandy, C. Rodriguez-Lafrasse, G. Le Duc, S. Roux, P. Perriat, “*In vitro* radiosensitizing effects of ultrasmall gadolinium based particles on tumour cells”, *J. Nanosci. Nanotechnol.*, **2011** Sep; 11(9): 7833-9.
4. L. Leclerc, **W. Rima**, D. Boudard, J. Pourchez, V. Forest, V. Bin, P. Mowat, P. Perriat, O. Tillement, P. Grosseau, D. Bernache-Assolant and M. Cottier, “Size of submicrometric and nanometric particles affect cellular uptake and biologic activity of macrophages *in vitro*”, **2012**, Accepted for publication in *Inhalation Toxicology*.

Contributions of the Author

Paper 1. Participating in initiating and developing the idea, writing the main parts of the article.

Paper 2. Participating in initiating and developing the idea, preparing the materials, characterization of the samples, planning and performing the major parts of the experiments, evaluation of the results and writing the main parts of the article.

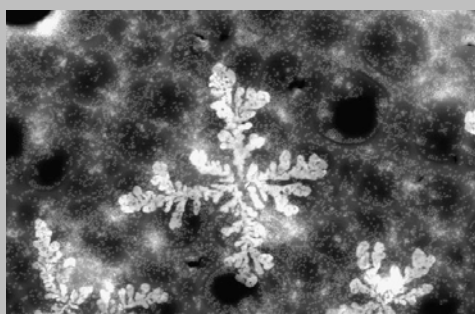
Paper 3. Planning and performing electron microscopy experiments, evaluation of the corresponding results and writing the corresponding parts of the article.

Paper 4. Participating in developing the idea, planning and performing electron and confocal microscopy experiments, evaluation of the results and writing the corresponding parts of the article.

Conference Presentations

1. **W. Rima**, M. Martini, P. Mowat, L. Joly-Pottuz, A. Malchère, L. Leclerc, J. Pourchez, T. Epicier, M. Cottier, D. Boudard, K. Masenelli-Varlot, P. Perriat, “Development of innovative electron microscopy techniques to study nanoparticles and biological cells interactions” (poster) – 4th annual seminar of MACODEV Research Cluster, Rhône-Alpes Region, March 22-23, **2010**, Annecy, France.
2. M. Martini, **W. Rima**, P. Mowat, S. Roux, O. Tillement, P. Perriat, “Robust universal biotracers based on hybrid GDS (Gold “Dye” Silica) nanosondes (Meeting Abstract: 82), Bulletin du Cancer, 98, March **2011**.
3. **W. Rima**, L. Leclerc, L. Joly-Pottuz, J. Pourchez, A. Malchère, T. Epicier, M.T. Aloy, E. Armandy, C. Rodriguez-Lafrasse, P. Mowat, F. Lux, O. Tillement, P. Perriat, “Apport de la microscopie électronique dans la compréhension des mécanismes d’interactions entre nanoparticules et cellules cancéreuses” (oral) – 5th annual seminar of MACODEV Research Cluster, Rhône-Alpes Region, April 4-5, **2011**, Annecy, France.
4. **W. Rima**, L. Leclerc, L. Joly-Pottuz, J. Pourchez, A. Malchère, T. Epicier, M.T. Aloy, E. Armandy, C. Rodriguez-Lafrasse, P. Mowat, F. Lux, O. Tillement, P. Perriat, “Apport de la microscopie électronique dans la compréhension des mécanismes d’interactions entre nanoparticules et cellules cancéreuses” (oral) – Nanohybrides 8 Seminar, June 5-9, **2011**, Corse, France.
5. **W. Rima**, L. Leclerc, L. Joly-Pottuz, J. Pourchez, A. Malchère, T. Epicier, M.T. Aloy, E. Armandy, C. Rodriguez-Lafrasse, P. Mowat, F. Lux, O. Tillement, P. Perriat, “La microscopie électronique dans la compréhension des mécanismes d’interactions nanoparticules/vivant” (oral and poster) – 12th seminar of Société Française des Microscopies (SFμ), June 27 - July 1, **2011**, Strasbourg, France.

First Prize in the Seminar Micrograph Competition for “Flocons d’or” STEM-in-SEM Image



Nanoparticules de polysiloxane à cœur d’or observées en mode STEM-in-SEM avec impuretés cristallisées

6. L. Leclerc, **W. Rima**, J. Pourchez, D. Boudard, V. Forest, V. Bin, P. Mowat, P. Perriat, P. Grosseau, D. Bernache-Assolant, M. Cottier, “Size effect of fluorescent nanoparticles on uptake by macrophages and in vitro toxicity” (oral) – International Conference on “Biological responses to nanoscale particles” SPP1313, September 11-15, **2011**, Essen, Germany.

7. **W. Rima**, L. Sancey, M.T. Alloy, E. Armandy, P. Mowat, A. Malchère, T. Douillard, T. Epicier, L. Joly-Pottuz, C. Rodriguez-Lafrasse, P. Perriat, “Interactions des nanoparticules de gadolinum radiosensibilisantes avec les cellules cancéreuses” (poster), La Journée de la Recherche Médicale 2012, may 4, **2012**, Grenoble, France.
8. **W. Rima**, L. Sancey, G. B. Alcantara, P. Mowat, M. T. Aloy, E. Armandy, T. Epicier, A. Malchère, B. Burdin, A. Rivoire, C. Boulé, I. Anselme-Bertrand, F. Lux, O. Tillement, S. Roux, C. Rodriguez-Lafrasse, J. Pourchez, M. Cottier, L. Joly-Pottuz, P. Perriat, “Portals of Entry of Radiosensitizing Nanoparticles into Cancerous Cells: Electron and Confocal Microscopy Approaches” (oral - Nanohybrides 9 Seminar, May 20-24, **2012**, Come, Italy.
9. **W. Rima**, L. Sancey, L. Joly-Pottuz, M.T. Alloy, E. Armandy, T. Epicier, F. Lux, A. Malchère, C. Rodriguez-Lafrasse, O Tillement, P. Perriat, “Electron microscopy contribution in the comprehension of interactions mechanisms between radiosensitizing nanoparticles and cancerous cells” (poster), 15th European Microscopy Congress, September 16-21, **2012**, Manchester Central, United Kingdom.
10. L. Sancey, J. Morlieras, **W. Rima**, A. Mignot, G. Braga-Alcantara, S. Dufort, P. Mowat, S. Roux, P. Perriat, F. Lux, O. Tillement, “Theranostic Ultrasmall Rigid Platforms: biological characterization from sub-cellular to organ level” (poster), World Molecular Imaging Congress WMIC 2012, September 5-8, **2012**, Dublin, Ireland.

Outline

Axe Principal de Recherche	2
Résumé	2
Abstract.....	3
Résumé de Thèse en Français	4
List of Papers	10
Contributions of the Author.....	10
Conference Presentations	11
General Introduction	17
1 Part One. The Framework	19
1.1 Introduction of Part One.....	19
1.2 Article I. Uptake of Therapeutic Nanoparticles into Cells: Review.....	22
1.2.1 Introduction	22
1.2.2 Uptake Mechanisms of Nanoparticles.....	24
1.2.2.1 Phagocytosis Pathway.....	24
1.2.2.2 Pinocytosis Pathway	26
1.2.2.2.1 Clathrin-Mediated Endocytosis Pathway	27
1.2.2.2.2 Caveolae-Mediated Endocytosis Pathway.....	29
1.2.2.2.3 Macropinocytosis Pathway.....	31
1.2.2.2.4 Clathrin- and Caveolae-Independent Endocytosis Pathway	33
1.2.2.3 Passive Diffusion	34
1.2.3 Cellular Toxicity Assays of Nanoparticles used for Radiosensitization	34
1.2.3.1 Cell Survival Assays	35
1.2.3.2 Cell Stress Assays	36
1.2.3.3 Cell Viability Assays	37
1.2.4 Characterization Techniques for Nanoparticles Uptake.....	39
1.2.4.1 Analytical Spectroscopy.....	39
1.2.4.2 Optical Microscopy.....	40
1.2.4.3 Electron Microscopy	42
1.3 Conclusion of Part One	44
2 Part Two. Biological Sample Preparation Protocols for Electron Microscopy Observations	45
2.1 Introduction of Part Two	45
2.2 Methodology and Principles of Chemical Fixation.....	49
2.2.1 Primary Fixation.....	50
2.2.2 Washing.....	52
2.2.3 Secondary Fixation.....	53
2.2.4 Dehydration.....	54
2.2.5 Infiltration.....	56
2.2.6 Embedding or Inclusion	57
2.2.7 Ultramicrotomy Sectioning	58
2.2.8 Positive Staining Contrast	60
2.3 Artifacts in Transmission Electron Microscopy: Main Changes Specific to Biological Materials	61
2.4 Techniques Used	65
2.4.1 Protocol of Sample Preparation for TEM Observations.....	65
2.4.2 Protocol of Sample Preparation for SEM Observations.....	66
2.5 Conclusion of Part Two.....	67

3 Part Three. Internalization Studies of Sub-5 nm Gadolinium-Based Nanoparticles Used as Radiosensitizers	68
3.1 Introduction of Part Three.....	68
3.2 Article II. Internalization Pathways of Gadolinium-Based Radiosensitizing Nanoparticles into Cancer Cells	70
3.2.1 Abstract.....	70
3.2.2 Introduction.....	71
3.2.3 Results and Discussion.....	73
3.2.3.1 Need of a Microscopic Study to Understand the Correlation Between Internalization and Radiotherapy Results	73
3.2.3.2 Particle and Cell Characterizations	75
3.2.3.2.1 Particle Characterization	75
3.2.3.2.2 Cell Characterization.....	77
3.2.3.3 TEM Observations of Nanoparticle Cellular Uptake as a Function of Concentration and Incubation Time.....	78
3.2.3.3.1 Lecture Key of TEM Micrographs.....	78
3.2.3.3.2 Effect of Concentration	81
3.2.3.3.3 Effect of Incubation Time	84
3.2.3.4 Macropinocytosis as the First Entry Mechanism of GBNs at a Moderate Dose.....	86
3.2.3.4.1 First Indication of a Macropinocytosis Process	86
3.2.3.4.2 General Description of the Complete Entry Mechanism Involving Two Successive Steps: GBNs Agglomeration at Vicinity of the Cell and Internalization via Lamellipodia (Macropinocytosis)	87
3.2.3.4.3 Confirmation of Macropinocytosis by Confocal Microscopy Using Inhibitors	89
3.2.3.5 Passive Diffusion as a Second Mechanism for GBNs Entry	91
3.2.3.6 Relative Quantification of the Different Internalization Mechanisms and Explanation of Radiotherapy Efficiency at Moderate Dose	92
3.2.3.6.1 Determination of the Quantity of Particles Entered by Macropinocytosis.....	92
3.2.3.6.2 Determination of the Quantity of Particles Entered by Passive Diffusion	94
3.2.3.6.3 Recapitulation of the Quantities of Gd Internalized by the Different Entry Pathways (Macropinocytosis and Passive Diffusion) and Adherent on Cell Surface	95
3.2.4 Conclusions.....	98
3.2.5 Experimental Section	99
3.2.5.1 Nanoparticle Characterization	99
3.2.5.1.1 Size Measurement and Structural Characterization	99
3.2.5.1.2 Fluorescence Correlation Spectroscopy (FCS)	99
3.2.5.1.3 Zeta Potential	100
3.2.5.1.4 Relaxivity.....	100
3.2.5.1.5 Absorbance	100
3.2.5.2 Cell Lines and Culture Conditions.....	100
3.2.5.3 Particles Internalization in SQ20B Cells	100
3.2.5.4 Determination of Uptake by Inductively Coupled Plasma (ICP).....	101
3.2.5.5 Clonogenic Survival Assay at 2 Gy	101
3.2.5.6 Transmission Electron Microscopy	101
3.2.5.7 Scanning Electron Microscopy.....	102
3.2.5.8 Confocal Laser Scanning Microscopy	102
3.2.6 Supporting Information.....	103
3.2.6.1 Radiosensitizing Efficiency of Particles upon another Type of Cells (U87)	103
3.2.6.2 Determination of the Size Distribution of the Cells From that of the Cell Sections Obtained by Electron Microscopy: Mathematic Formulation	104
3.2.6.2.1 Case of a Homogeneous Distribution of Cells	104
3.2.6.2.2 Case of a Heterogeneous Distribution of Cells	105
3.2.6.2.3 Size Distribution of the SQ20B Cells	106
3.2.6.3 Description of the Cell Cycle.....	108
3.2.6.3.1 The Different Phases of a Cell Cycle	108
3.2.6.3.2 Relative Duration of Cell Cycle Phases for Rapidly Replicating Human Cells.....	108
3.2.6.4 Confocal Imaging of the Vesicles Containing Agglomerates as a Function of the Incubation Concentration.....	109

3.2.6.5	Determination of Optimal Concentration of Inhibitors in Order to Evaluate the Entry Process of GBNs into Cells.....	109
3.2.6.6	Additional FCS Results	111
3.3	Article III. <i>In Vitro</i> Radiosensitizing Effects of Ultrasmall Gadolinium-Based Particles on Tumour Cells.....	113
3.3.1	Introduction	114
3.3.2	Materials and Methods	115
3.3.2.1	Chemicals.....	115
3.3.2.2	Gadolinium Oxide Nanoparticles Synthesis.....	115
3.3.2.2.1	Preparation of Gadolinium Oxide Cores	115
3.3.2.2.2	Coating of Gadolinium Oxide Cores by a Polysiloxane Shell.....	116
3.3.2.3	Particles Internalization in U87 Cells.....	116
3.3.2.4	Determination of Intracellular Gadolinium Content by Inductively Coupled Plasma - Optical Emission Spectroscopy	117
3.3.2.5	Single-Cell Gel Electrophoresis Comet Assay	117
3.3.2.6	γ -H2AX Assay	117
3.3.2.7	Measurement of Cell Survival After Irradiation of Cells Containing Gd-Based Particles	118
3.3.2.8	Statistical Analysis.....	119
3.3.3	Results and Discussion.....	119
3.3.4	Conclusion.....	124
3.3.5	Supporting Information.....	125
3.3.5.1	Characterization of Gd-Based Particles	125
3.3.5.2	Viability of the U87 Cells after Particles Internalization	125
3.3.5.3	Location of the Particles within the Cytoplasm	126
3.3.5.4	Details upon Comet Assays	126
3.3.5.5	Formation of Particles Aggregates within the Cells	127
3.3.5.6	Details on Transmission Electron Microscopy	127
3.3.5.7	Mechanisms of DNA Repair.....	128
3.4	Gadolinium-Based Nanoparticles: Towards <i>in vivo</i>.....	130
3.5	Conclusion of Part Three	134
4	Part Four. Internalization Studies of Silica Particles of Variable Sizes.....	135
4.1	Introduction of Part Four	135
4.2	Article IV. Size of Submicrometric and Nanometric Particles Affect Cellular Uptake and Biological Activity of Macrophages <i>in vitro</i>	137
4.2.1	Abstract	137
4.2.2	Introduction	138
4.2.3	Materials and Methods	139
4.2.3.1	Fluorescent Silica-Based Particles	139
4.2.3.1.1	Synthesis	139
4.2.3.1.2	Characterization	140
4.2.3.1.2.1	Dynamic Light Scattering (DLS) and Zeta Potential Measurement	140
4.2.3.1.2.2	Transmission Electron Microscopy	140
4.2.3.1.2.3	Scanning Electron Microscopy	140
4.2.3.1.2.4	Fluorescence Spectral Analysis	140
4.2.3.2	Cellular Assays	140
4.2.3.2.1	Macrophage Cell Culture and Dose of Particles.....	140
4.2.3.2.2	Confocal Imaging.....	141
4.2.3.2.3	Transmission Electron Microscopy (TEM).....	141
4.2.3.2.4	Quantitative Uptake Assessment.....	141
4.2.3.2.5	Toxicity Assessment.....	142
4.2.3.2.6	Statistical Analysis	142
4.2.4	Results.....	143
4.2.4.1	Physicochemical Characterizations.....	143
4.2.4.2	Qualitative Uptake Assessment by Microscopy.....	146
4.2.4.3	Quantitative Uptake Assessment by Fluorometry.....	147
4.2.4.4	Toxicity Assessment	149
4.2.5	Discussion	150
4.2.6	Conclusion.....	152

4.3	Silica Nanoparticles: Towards <i>in vivo</i>	153
4.3.1	<i>Ex vivo</i> Human Models from Colectomy Specimens for the Diagnosis of Colorectal Cancer with Functionalized Fluorescent Nanoparticles	153
4.3.1.1	Utilization of the FIB-SEM Technique.....	154
4.4	Conclusion of Part Four	159
5	General Conclusions and Perspectives	160
6	References	163

General Introduction

This thesis concerns electron microscopy contribution in the comprehension of interaction mechanisms between nanoparticles and biological materials. It is motivated on one hand by the lack of microscopic description of these interactions and on the other hand, by health risks and cancer treatment considerations concerning contact of nanoparticles with living matter.

Thanks to its resolution, various imaging methods and associated analytical tools, electron microscopy constitutes a key technique for characterizing materials and finds fully its relevance in the multidisciplinary field of use of nanoparticles in nanomedicine and nanotoxicology. Electron microscopy overcomes the limited resolution of confocal microscopy, widely used in biology, and enables the visualization of eventual nanoparticles agglomeration, their location on the cellular membrane, and their traffic within the cytoplasm. But conventional electron microscopy involves observing in vacuum conditions, critical for hydrated biological samples considered as a multiphase material in liquid solution. High vacuum induces dehydration or evaporation of water leading to the complete collapsing of the structures making impossible their observations in their native state. An extra difficulty has to be taken into account when using transmission electron microscopy for microstructural investigations. Even when highly accelerated, electrons transit only a very small material thickness. The sample must be stable under vacuum and it must be very thin (on the order of 100 nm). These problems require complex and time consuming preparation procedures, leading to the elimination of the liquid phase and the complete shutdown of the vital process, in order to prevent changing the original structure. The challenge with these observations is to evaluate the results and interpret images taking into account the artifacts that may be caused by the samples preparation techniques and/or produced due to irradiation under electron beam.

In this project, *in vitro* and *in vivo* approaches were considered to provide microscopic description of nanoparticles-living matter interactions. *In vitro* aspects of nanoparticles-cells interactions presented are: internalization mechanisms of ultrasmall gadolinium based nanoparticles in human head and neck squamous cells carcinoma SQ20B cell line, their radiosensitizing effects on human glioblastoma cell line U87, and the influence of the size parameter of silica nanoparticles of variable size on cellular uptake and biological activity of macrophages. Participation to two *in vivo* studies including gadolinium based nanoparticles and silica particles was also carried out for electron microscopy observations.

Our main objective is to make observations at a smaller scale than is normally used in biology to assess to what extent these new data will help to better understand nanoparticles-living matter interactions and to determine the mechanisms responsible for nanoparticles toxicity and radiosensitizing effects. This approach allows us to precisely detect the location of nanoparticles in biological cells and consequently remove a lock key to advancing research in nanomedicine and nanotoxicology

To achieve this objective, the work programs integrated the contribution of different laboratories. It was divided into four key scientific aspects:

- Task 1: synthesis of nanoparticles
- Task 2: characterization of nanoparticles
- Task 3: *in vitro* performance and biocompatibility studies
- Task 4: *in vivo* performance and biocompatibility studies

Considering their domains of expertise, the researcher partners were assigned to one or several of those tasks. This PhD project was part of tasks 2, 3 and 4 and consists in a part of different mutual and multidisciplinary projects including physicists, chemists and biologists.

This manuscript is divided into four parts:

After a brief introduction, the framework based on selected pieces of literature will recall a basic knowledge concerning uptake mechanisms of nanoparticles, the cellular toxicity assays of nanoparticles used for radiosensitizing and the techniques used to characterize their interactions with cells. This work is written as a review article, here called Article I.

In the second part, the electron microscopy experimental techniques used in this work will be detailed.

The main part of the thesis (parts 3 and 4) contains 3 articles that highlight the scientific results that were obtained. Article II focuses on the internalization pathways of gadolinium-based radiosensitizing nanoparticles into SQ20B cancer cells. Article III presents the investigation of *in vitro* radiosensitizing effect of gadolinium particles on the human glioblastoma radioresistant cell line U87. Article IV synthesizes the investigation of the size effect of submicrometric and nanometric silica particles on cellular uptake and biological activity of macrophages *in vitro*.

1 Part One. The Framework

1.1 Introduction of Part One

This part intends to report selected pieces of information on the uptake of nanoparticles into the cells. After a focus on the framework, a state-of-art presented as a review article describes the internalization mechanisms of nanoparticles into cells, the tests usually used to assess toxicity of nanoparticles and the main techniques used to characterize nanoparticles/cells interactions.

Development of devices at the nanoscale dimension can be considered as one of the main evolutions of recent science. All over the world, laboratories are trying to study and control matter on molecular and atomic scales. Prestigious editorials focus on nanotechnology describing it as a promising field with a considerable potential.^{[i][ii]} In the United States, the budget allocated to the National Nanotechnology Initiative has been specified at 1.64\$ billion for 2010, it is 7.3% more than the budgetary proposal for 2009.^[iii] In France, the government announced two support programs for nanotechnology: Nano 2012 (2.3 billion Euros) and Nano-Innov (70 million Euros).^[iv] Things ‘nano’ in size are causing a general euphoria. This is most probably thanks to their expected significant advances in many applications (optoelectronics,^[v] tribology,^[vi] lithography^[vii]), especially human health care and cancer treatment.^{[viii][ix]}

Indeed, cancer remains a major public health problem worldwide. According to the last report of the International Agency for Research on Cancer (IARC), for the year 2008, it is estimated that there were 12.4 million incident cases of cancer, 7.6 million deaths from cancer and 28 million persons alive with cancer within five years from initial diagnosis. By 2030, it is estimated that there will be more than 26 million incident cases of cancer each year.^[x] In France, during the year 2011, it is estimated that there were 365 thousand incident cases of cancer and 147 thousand deaths from cancer.^[xi]

In the multimodality and multidisciplinary management of cancer treatment, the therapeutic mainstays remain surgery, radiotherapy and chemotherapy, the relative contribution of each being prescribed following the kind of tumor. Radiation therapy (external-beam therapy or radiotherapy, brachytherapy or systemic radiation therapy) is one of the major treatment options in cancer management. It kills cancer cells by damaging their DNA (DeoxyriboNucleic Acid) but can also damage normal cells leading to side effects and a risk of second cancer.

To improve cancer-fighting techniques, nanotechnology is a promising strategy. Due to their unique physical and chemical properties, nanoparticles (NPs), colloidal particles having a size of 1 to 1000 nm,^[xii] are one of most promising leads explored for medical applications including anti-tumor activities.^[xiii] But even if nanoparticles have been used in several applications such as diagnostics, prognostics and management of targeted cancer, drug delivery and imaging,^{[xiv][xv]} they still a question of science to be deepened. Indeed, medical applications imply materials and devices designed to interact with biological cells. So understanding the interactions of nanoparticles with cells is a key gap that needs to be filled. Among techniques used to characterize these interactions, electron microscopy (EM) constitutes a key technique because of its various imaging and spectrometry options. It involves the interaction of accelerated electron source with the sample to be analyzed under vacuum conditions. The light microscope (LM) is limited in its resolution to about 0.25 micrometers. If two objects are closer together than that, they blur and cannot be distinguished by the LM. Electron microscopes overcome this limitation and achieves theoretical resolutions down to 0.2 nanometers, allowing useful magnifications of biological material up to several hundred thousand times. Resolution is governed by the wavelength of illumination, and an electron beam has a much shorter wavelength (3.70 pm at 100 kV of acceleration voltage)^[xvi] than visible light (about 400 to 750 nanometers).

In biology field, electron microscopy has profoundly influenced our understanding of tissues organizations and cell structure. Since 1934, when Marton^[xvii] published the first electron micrograph of a biological sample (a 15- μ m thick specimen of a sundew leaf that was impregnated with osmium tetroxide), where the image resolution was inferior to conventional light microscope images, till 1981 when BJ Poiesz *et al.*^[xviii] used the transmission electron microscope (TEM) to characterize a new Retrovirus (HTLV) in primary cultured cells of a patient with Sezary's T-cell leukemia, discoveries in cell biology that were made possible by the electron microscope did not stop to follow on. Historical milestones in the development of the electron microscope and key dates of major contributions of electron microscopy in biology field are well summarized in the first chapters of "Electron Microscopy: Principles and Techniques for Biologists", by John J. Bozzola and Lonnie D. Russel.^[xix]

Considering the association of nanotechnology with life science, electron microscopy appears to be a relevant technique to describe the interactions of these two nanometric entities. Many nanoconstructs have been shown localized within the cell cytoplasm. They are injected through various methods in the human body, and their uptake by the cellular environment has been observed in several internalization pathways. After uptake, nanoparticles interact with

cells to different extents, depending on their size, shape, surface properties, receptors and ligands grafted on their surface and tumor architecture. A deeper understanding of such cellular internalization mechanisms, intercellular trafficking and interactions of nanoparticles is important for their cytotoxicity and their effective therapeutic potential.

The next paragraph carefully describes the internalization routes of nanoparticles into cells, the cellular toxicity assays of nanoparticles used for radiosensitization and different techniques usually used to characterize nanoparticles/cells interactions by highlighting selected information from literature.

1.2 Article I. Uptake of Therapeutic Nanoparticles into Cells: Review

W. Rima, L. Sancey, L. Joly-Pottuz, P. Perriat and G.B. Alcantara

Status: Draft

1.2.1 Introduction

Development of devices at nanoscale dimension can be considered as one of the main evolutions of recent science, because of their huge range of applications, as for instance optoelectronics,^[v] tribology,^[vi] lithography^[vii] and human health care.^{[viii][ix]} Nanoparticles (NPs), colloidal particles having a size inferior to 1000 nm,^[xii] are one of most promising leads explored especially for medical applications including the anti-tumor activities,^[xiii] due to unique physical and chemical properties. Medical applications imply materials and devices designed to interact with biological cells. One example is the new Ti-based implants prepared from biodegradable metal^[xx] or polymer^[xxi] for medical devices, which under mechanical stress or altered physiological conditions such as low-pH, can release large amounts of nanoparticles in the biological medium.^[xxii] The cellular responses to degradation products from these kinds of materials are important indicators for the biocompatibility of these widely used implantable medical devices.^[xxiii] Each cell can interact differently with a particular nanoparticle leading to a different adapted response to the desired application. Interaction of nanoparticles with cells is a key question in nanotechnology that needs to be clarified. Furthermore, understanding the internalization pathways and intracellular trafficking of nanoparticles into different types of cells is a key gap in nanotechnology that needs to be filled for enhanced bio functionalities and future developments as oral delivery of drugs and vaccines.^{[xxiv][xxv]} Therefore, we review the uptake model of the nanoparticles into diverse types of cells, their main internalization pathways, and their toxicology within the cells, supported with good established characterization techniques.

Due to their small size, nanoengineered particles could be viewed as biological entities, such as protein, DNA or viruses,^[xxvi] and are internalized into the cells *via* the same biological pathways. There are three main mechanisms: “phagocytosis” or cell eating (conducted mostly by macrophages, monocytes and neutrophils), “pinocytosis” or cell drinking, and passive diffusion.^[xxvii] Pinocytosis occurs in mammalian cells by four main mechanisms:

macropinocytosis, clathrin-mediated endocytosis (CME), caveolae-mediated endocytosis (CvME), and clathrin- and caveolae-independent endocytosis (**Figure 4**).

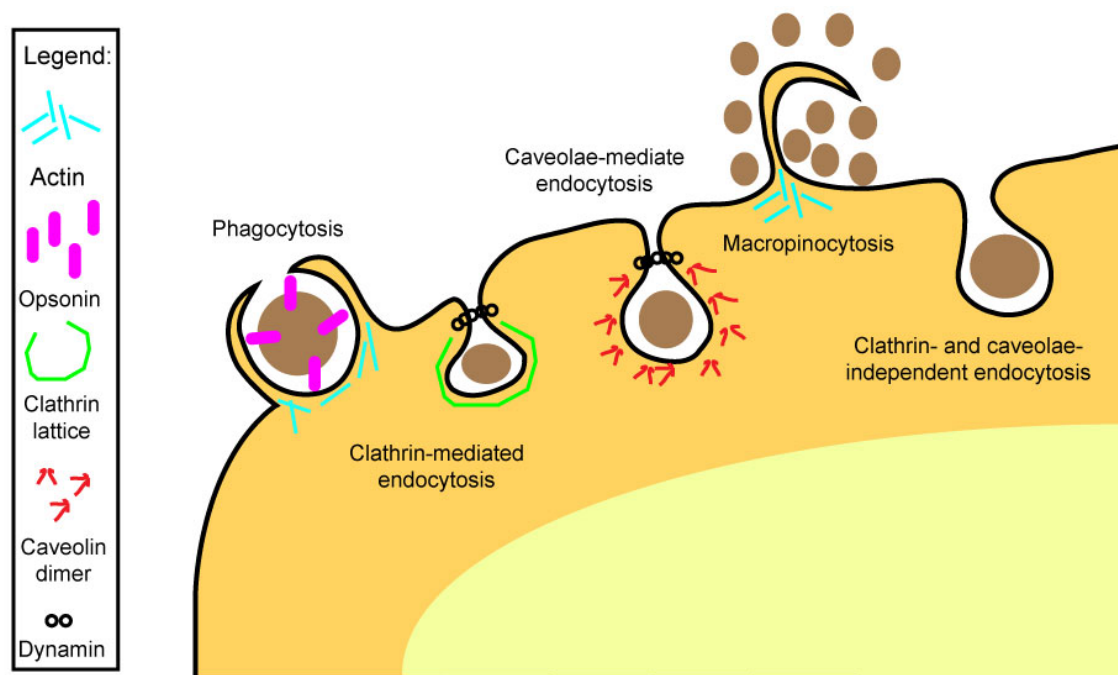


Figure 4: Schematic representation of the main endocytic pathways in mammalian cells: phagocytosis - actin regulated process and associated with opsonisation; clathrin-mediated endocytosis – associated with a clathrin lattice and GTPase dynamin dependent; caveolae-mediated endocytosis – dynamin dependent and associated with caveolin dimers; macropinocytosis – actin-based with poor selectivity and other endocytosis pathways independent of clathrin and caveolae.

Besides these main endocytic pathways, free particles can be internalized by passive diffusion through the cell membrane. This non-metabolic energy phenomenon is mainly related to a chemical concentration gradient between intra and extracellular milieu.^[xxviii]

The competitiveness between uptake mechanisms of the nanoparticles will depend on the cell line, physical and chemical composition of manufactured NPs including specific targeting moieties (functional groups) and the contact parameters (concentration, incubation time, temperature, etc) between these two entities.

For the predicted use on humans, the same principles applied to toxicology of the biologically based or naturally occurring molecules in living organisms should be implemented on these nanodevices. Different human exposure routes to NPs are possible, as blood circulation, respiratory and gastrointestinal tract.^[xxx] Each of those administration routes possess its own inconvenient and possible side effects. Little is known about the fate of inhaled nanoparticles after deposition upon respiratory epithelium and whether the translocated nanoparticles might cause inflammatory adverse effects.^{[xxx][xxxi]} Due to the enormous quantity of toxicology assessments, the results seem to be not conclusive. After the determination of the nanoparticles' toxicology, it is necessary to use several techniques to elucidate the uptake

mechanisms, including optical techniques (confocal and fluorescence microscopy) and electron microscopy techniques (transmission and scanning electron microscopy). We propose to highlight the process of internalization of diverse nanoparticles supported by optical and electron microscopies, their impact on toxicological assays such as cell survival, cell stress and cell viability, showing the difficulties among the literature.

1.2.2 Uptake Mechanisms of Nanoparticles

The uptake of particles and solutes into cells is shared among six common routes: phagocytosis, clathrin-mediated endocytosis (CME), caveolae-mediated endocytosis (CvME), macropinocytosis, clathrin- and caveolae-independent endocytosis, and passive diffusion. Concerning the phagocytosis, relatively large particles (> 300 nm) are internalized by specialized cells such as macrophages and monocytes. In CME pathway, particles are internalized into coated pits, formed by clathrin protein. After invagination and scission, the coated vesicle is released from the plasma membrane into the cell. Caveolae are 55-60 nm invaginations at the cell surface that can pinch off to form vesicles. Macropinocytosis pathway occurs by membrane ruffling creating cytoplasmic vacuoles, i.e. macropinosomes, distinct from endosomes by their ability for regulated exocytosis and other membrane properties. Non-clathrin-coated pit uptake is related to rafts, cholesterol microdomains having 40-50 nm of diameter.^{[xxxii][xxxiii]} Finally, passive diffusion, associated to a chemical concentration gradient between intra and extracellular milieu, is correlated to small size particles. Understanding the details of these pathways is essential for the future use of nanoparticles in biomedicine applications.

1.2.2.1 Phagocytosis Pathway

Against infectious agents and exogenous inert particles, the organism possesses several defense mechanisms and phagocytosis (**Figure 5**) process is one of them. Phagocytosis is conducted by specialized cells, professional phagocytes, as macrophages, monocytes and neutrophils.^[xxxiii] It is an actin-dependent process that can be described by the following steps: recognition by opsonization, adhesion of the opsonized particles to the phagocyte, ingestion of the particle, phagosome formation, and after a series of fusion and fission events, a phagolysosome. The opsonization (Figure 5-A) consists in tagging the foreign particle by proteins, opsonins, making them visible to the phagocytes. The opsonized particles bind to the phagocyte surface through specific recognition (Figure 5-B), triggering actin assembly and

ingestion of the particle (Figure 5-C). The actin is depolymerized from the phagosome (Figure 5-D) and the latter fuses, through a series of fusion and split events, with lysosomes leading to the enzyme-rich phagolysosomes (Figure 5-E) and later to particle degradation.^[xxxiii]

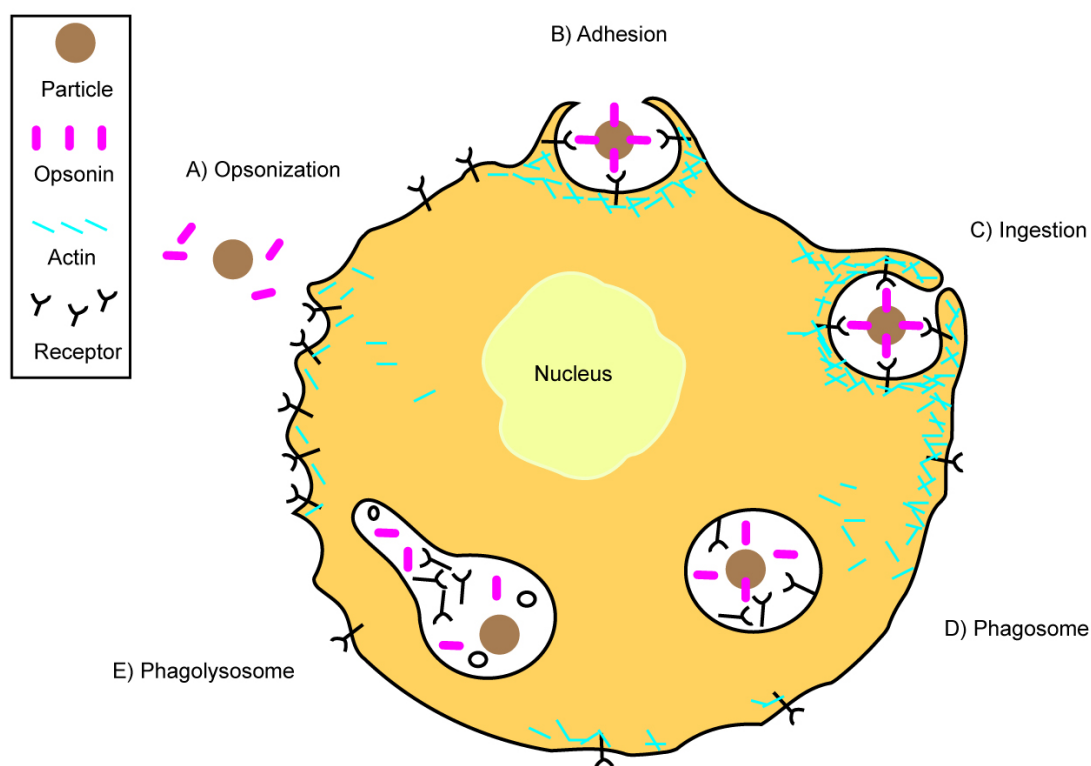


Figure 5: Schematic representation of phagocytosis in mammalian cells. A) Opsonization - tagging the foreign particle by opsonins to make them visible to the phagocytes. B) Adhesion to the phagocyte surface through specific recognition of the opsonized nanoparticles. C) Ingestion of the particle. D) The actin is depolymerized from the phagosome. E) An enzyme-rich phagolysosomes is created through a series of fusion and split events, with lysosomes and later to particle degradation.

The particle size and composition are key factors for the drug delivery vehicles and those parameters will be determinant on particles interaction with the macrophage membrane and opsonins prior to phagocytosis.^[xxxiv] Nanoparticles must be prepared to prevent the recognition by cellular defense system and persist enough in the body, increasing the probability for the nanoparticles to reach their target. One example is the poly-ethylene glycol (PEG)-adsorbed nanoparticles (< 100 nm) of which hydrophilic adsorbed protective layer is able to delay the first step in the opsonization process and thus allowing an increase half-life of the particles in the blood circulation.^[xxxiv]

In literature, it is generally reported that a particle size range of 200 nm to several microns, is capable of being phagocytosed.^{[xxxv][xxxvi]} This is explained by the fact that large particles have larger surface area to perform a chain reaction necessary for efficient opsonization mechanism than smaller ones.^[xxxvii] For example, new recourses for drug delivery systems of HIV/AIDS therapy are originated on non-polymeric nanocarrier-based antiretroviral treatment by

functionalized liposomes, nanosuspensions, and nanoemulsions. Because of phagocytosis by monocytes/macrophages, the side effects of the drugs both *in vitro* and *in vivo* should be reduced.^[xxxviii] The proper geometric configuration of the drug-functionalized nanoparticles will be determinant for the complement activation on the macrophages mechanism.

Besides the size, other important nanoparticle parameters that contribute to their uptake into the cells are the physicochemical characteristics of its surface. As for the phagocytosis, it will be the nature of the surface that determinates the interaction with the macrophage membrane and with opsonins. Interactions between particles and body fluids can lead to surface modifications, with attraction of immunoglobulin and complement receptors leading to a phagocytosis pathway.^[xxiv]

As already mentioned, particles above 200 nm are suitable for the drug carrier studies, however to prevent the particles with size below 100 nm to be eliminated from the blood stream, some surface modifications are required. Wang *et al.*^[xxxix] prepared superparamagnetic magnetite nanoparticles with average diameters of 6-8 nm functionalized with poly(N-isopropylacrylamide) followed by immobilization of heparin (a widely used polymer as an injectable anticoagulant). The heparinized magnetite nanoparticles are effective in delaying phagocytosis by preventing the bound heparin on protein adsorption and cell membrane association process, enabling their use in biomedical applications.

For a model of drug delivery system, PGLA (poly(lactic co-glycolic) microspheres were synthesized with a lung surfactant DPPC (dipalmitoylphosphatidylcholine), which was observed to reduce phagocytosis, minimizing the microspheres uptake by all cell types.^[xi] Entry mechanisms inhibition is a regular approach to determine the ultimate sub-cellular fate and to better understand the characteristics of their uptake pathways. The inhibitors could be molecules that inhibit the electron transport chain (sodium azide) or the actin formation (cytochalasin D) blocking the phagocytosis process or even a bacteria as for example the *Streptococcus pyogenes* bacteria, which are able to inhibit both the secretion of azurophilic granules to phagosomes and pinosome constitution.^[xii]

1.2.2.2 Pinocytosis Pathway

The cell drinking mechanism is conducted by four independent mechanisms: clathrin-mediated endocytosis (CME), caveolae-mediated endocytosis (CvME), macropinocytosis, and clathrin- and caveolae-independent endocytosis. The pinocytosis mechanisms can be specific

or nonspecific, and the most prominent cell drinking mechanism given by the cell type will drive to the nanoparticles engulfment.^[xliii]

1.2.2.2.1 Clathrin-Mediated Endocytosis Pathway

CME regulates the cell surface levels such as the uptake of growth factors and receptors, entry of pathogens, and synaptic transmission.^[xliiii] Its endocytosis characteristic vacuole, the clathrin coat, serves not only to shape the budding vesicle, but also to pack of the cargo. Thus, the protein sorting and vesicle budding are functionally integrated. Clathrin is the main protein component of the coat and its basic architecture is regulated by a three-legged structure termed a triskelion. Clathrin is an ubiquitary polymerized-soluble protein and the rate of endocytic activity of a given cell is inversely proportional to the correlation of these two states.^{[xli][xliiv]} When the coated pit becomes deeply invaginated, a membrane scission event is keen to release the coated vesicle. It is established in the literature that this is the role of the GTPase protein dynamin.^[xli] The coated vesicles are rapidly uncoated. They are then fused and docked with their target organelles, the endosomes. They fuse with one another producing a sorting endosome, the first main branch point in the CME pathway, targeting molecules to their correct destinations, late endosomes also called multivesicular bodies. Lysosomes constitute the main terminal compartment reached by molecules internalized along the endocytic pathway.^[xliiv] These vesicles release their cargo in cell cytoplasm or specific compartment depending on the nature of the carrier. For example, positive charged nanoparticles were rapidly internalized into HeLa (cervical cancer cells) *via* CME pathway, improving their potential as drug delivery carriers.^[xliiv] **Figure 6** shows a scheme of the CME internalization mechanism.

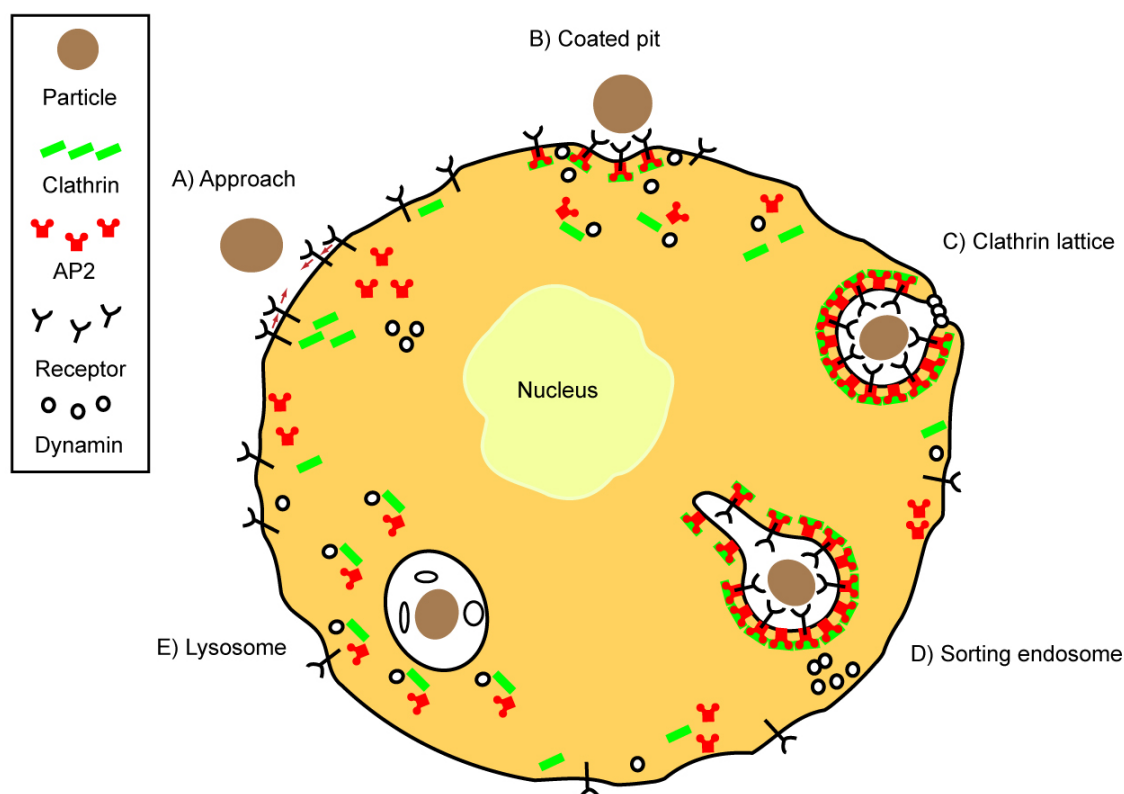


Figure 6: Scheme of CME pathway in mammalian cells. B) Approach of the target particle. b. Adhesion to the clathrin pit. C) Ingestion of the particle, by a clathrin lattice. D) After shedding its clathrin coat, and fusion with another endosomes, a sorting endosome is produced. E) The lysosome is the final destination reached by molecules or particles internalized along the endocytic pathway.

The layered double hydroxide (LDH) nanoparticles are anionic clay materials with low toxicity, charged surface and good biocompatibility, being good candidates for drug delivery system and their uptake mechanisms into cells are well studied.^{[xlvii][xlviii]} There are several possible endocytic pathways by which this kind of nanoparticle-based drug carrier enters the cell. Choy *et al.* reported that LDH nanoparticles have a concentration dependent cellular uptake based on principally clathrin-mediated endocytosis with an endosomal escape by means of immunofluorescence and confocal microscopic studies.

Contrary to the LDH particles, the internalization of titanium dioxide (TiO₂) particles is still unclear, possibly depending on the different shapes and sizes and exact composition of the TiO₂ particles. Singh *et al.*^[xlix] studied the initiating pro-inflammatory effects on A549 cells treated with different model TiO₂ particles *in vitro*. They demonstrated a rapid uptake in A549 cells for each of the TiO₂ samples, generally as membrane bound aggregates and large intracellular aggregates in vesicles, vacuoles and multivesicular bodies. The large aggregates of TiO₂ particles appeared to enter in the cells by phagocytosis. Small aggregates of 20-30 nm nanoparticles were observed in clathrin-coated vesicles indicating the clathrin-mediated endocytosis. Thus, the size seems to be an important parameter that controlled the endocytic

pathway, with large particles engulfed by the cell eating mechanism and small particles by the cell drinking mechanism.

1.2.2.2 Caveolae-Mediated Endocytosis Pathway

The caveolae-mediated endocytosis (CvME) is a highly regulated endocytic pathway with a three-step trafficking process: accumulation of molecular cargo in endothelial caveolae, budding mechanisms and fusion machinery of caveolae.^[i] Caveolae invaginations are flask-shaped membrane invaginations, enriched in glycosphingolipids, cholesterol and lipid-anchored proteins. They can be easily identified by transmission electron microscopy. Their shape and structural composition are provided by caveolin, a dimeric protein that forms a striated caveolin coat on the surface of the membrane invaginations.^[ii] CvME is a highly regulated process with complex signaling. Cargo fuses with caveolin coated spherical vesicular structures yielding to caveosomes, with size range between 50 and 80 nm.^[xxxiii] The endocytosed molecules internalized by caveolae converge later with the same fate of the CME pathway molecules reaching the endoplasmic reticulum and eventually lysosomes.^{[lii][liii]}

Figure 7 presents the particularities of the CvME pathway.

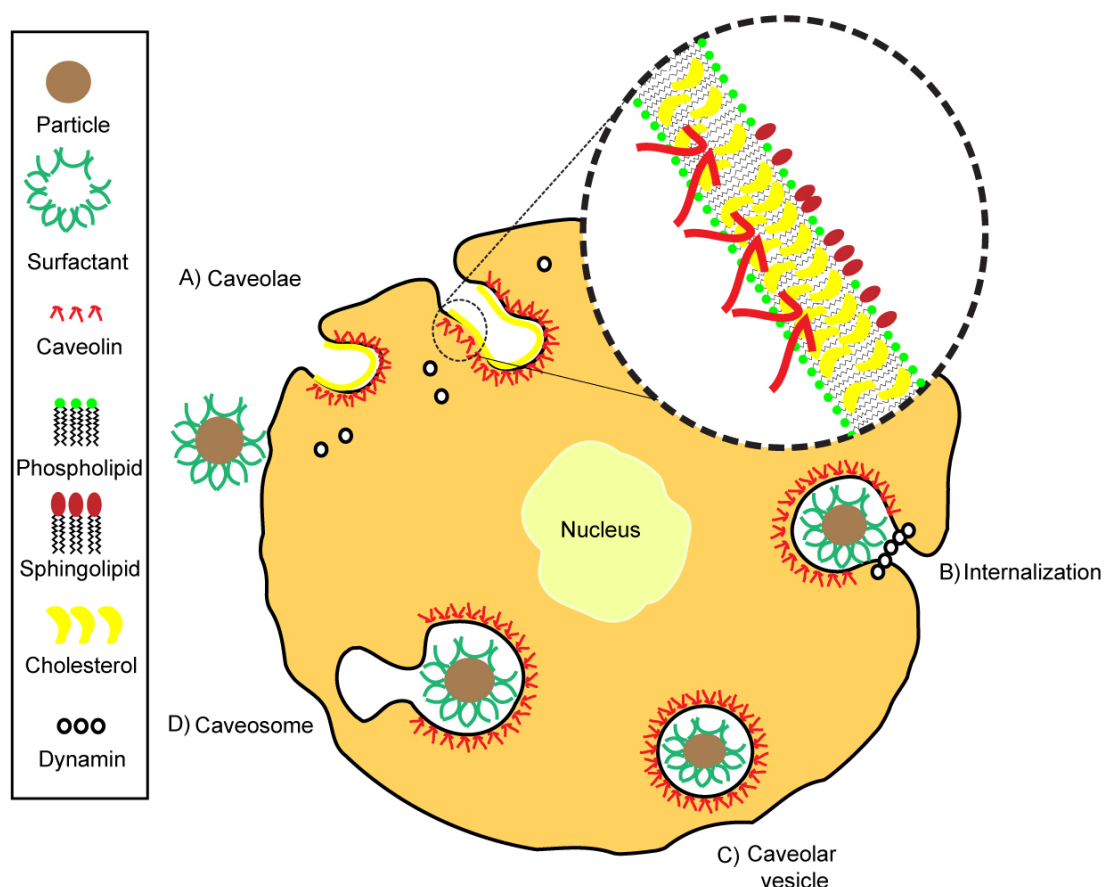


Figure 7: Scheme CvME in mammalian cells. A) Caveolae is a regular invagination in the cells, enriched in glycosphingolipids and cholesterol (in detail). B) Internalization of the particle. C) Formation of a caveolae vesicle. D) After fusion process, with no caveolin uncoating, the vesicular cargo is transferred to more complex tubular organelles, caveosomes.

The protein associated with caveolae structures is caveolin-1, important for the formation and stability of mature caveolae in the cell membrane. This dimeric protein delineates cholesterol and inserts as a loop into the inner leaflet of the plasma membrane forming a striated caveolin coat on the membrane invaginations. During the endocytosis process, the caveolin-1 moves along with the vesicles into the cytosol leaving no residue in the plasma membrane. However, its true role in the endocytic process is not clear yet.^[ii] A prototypical ligand for CvME has been examined during Simian Virus 40 (SV40, a virus having the potential to cause tumors) entry to understand this process.^[liv] First, the particles bind to the plasma membrane and move along to caveolar invaginations. The new assembled vesicles move through the cytoplasm with the help of an activated signaling transduction cascade, and then the vesicular cargo is transferred by membrane fusion, to larger and more complex tubular membrane organelles called caveosomes. These vesicles are delivered intracellularly among microtubules to the endoplasmic reticulum (ER) from which SV40 will travel to the nucleus. Then SV40 uptake through caveolae is ligand triggered, meaning that this pathway could be used for targeted

macromolecular delivery into cells through the binding of caveolae-associated membrane receptors, for example, into nanoparticles surface.

The nanoparticles should be functionalized because of the CvME specificity with well-regulated ligands known to be internalized through nondestructive receptor-dependent caveolae-mediated endocytosis.^[lv] An attempt to enhance an effective gene transfection was performed introducing ligands that lead gene vectors to target CvME on nanoparticle surface. A non-viral peptide vector was used to target gene loaded poly(lactic acid)-poly(ethylene glycol) nanoparticles for highly receptor-mediated intracellular delivery. The physicochemical and biological properties, the transfection efficiency, the cellular cytotoxicity and several selective inhibitors were used to determine the internalization pathways. The non-viral peptide could mediate rapid and efficient nanoparticle uptake by CvME, leading to significant gene transfection, fundamental for the intracellular delivery of therapeutic agents.^[lvi]

Nevertheless, even with a great interest in caveolae, little is done to understand the molecular basis for the linking between cargo molecules, caveolae-localized receptors, triggered endocytosis and different types of nanoparticles.

1.2.2.2.3 Macropinocytosis Pathway

Macropinocytosis is assigned to cell surface ruffling giving rise to discrete cytoplasmic vacuoles,^[lvii] the macropinosomes, circular or curved ruffles shapes followed by an aperture well sealed (**Figure 8**). They are relatively large, with diameters from 500 to 2000 nm, providing an efficient route to internalize non-selective solute macromolecules, as viruses,^[lviii] bacteria,^[lix] and apoptotic cell fragments.^[lx] Macropinosomes not only regulates the membrane traffic along the intracellular pathway, but also, in contrast to endosomes, regulates exocytosis and other membrane properties.^[lxi]

Macropinocytosis is associated with considerable cell-wide plasma membrane ruffling induced by the activation of actin and microfilaments connected to the plasma membrane.^[lxii] Different cells ruffle to various extents, and can take forms of planar lamellipodia, circular ruffles or blebs. A ruffle is formed by a linear band of actin polymerization near the plasma membrane,^[lvii] which lengthens into a roughly planar extension of the cell surface (Figure 8). For the invagination of the molecular/particle cargo, only a very small membrane fusion event is required, yielding irregular vesicles known as macropinosomes. The fate of the uptake cargo depends on the cell type. Usually, a sorting endosome is produced after fusion and fission processes, targeting molecules to late endosomes and lysosomes, their final destination.

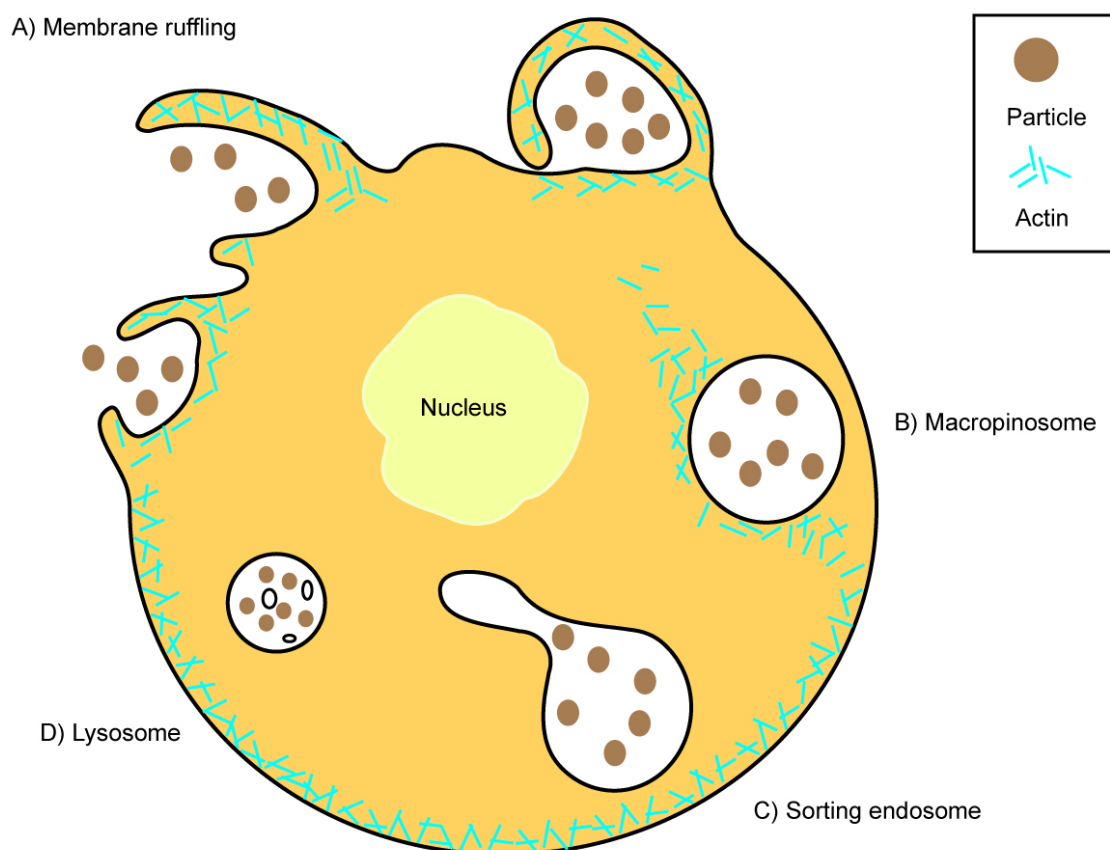


Figure 8: Schematic view of macropinocytosis in mammalian cells. A) Membrane ruffling induced by the activation of actin and microfilaments can take diverse forms. B) After a very small membrane fusion event, a macropinosome is formed. C) After fusion and fission events, a sorting endosome is produced. D) The lysosome is the final destination reached by molecules or particles internalized along this endocytic pathway.

Titanium dioxide (TiO_2) nanoparticles have attractive photocatalytic properties that led them in different applications as nanotoxicology studies.^{[xxix][xlix]} Although nanoparticle internalization is metabolically dependent, when it comes to a particular endocytic mechanism, it becomes nonspecific. In Thurn KT studies,^[xlii] PC-3M cells have two primary endocytic mechanisms: macropinocytosis and clathrin-mediated endocytosis. The internalization of TiO_2 NPs in the cells will depend on the size, shape, and charge of the nanoparticles, and also on the cell type treated.

Thurn KT *et al.* studied NPs with size under 20 nm, with surface-conjugated fluorescent Alizarin Red S (ARS), and the endocytic pathways involved in their uptake into prostate cancer PC-3M cells. They demonstrated that the TiO_2 nanoparticles uptake was dependant on CME, CvME and macropinocytosis. One explanation could be the nanohybrids' size, which is smaller than any of the vesicles formed during endocytosis process: macropinosomes from 500 to 2000 nm; clathrin-coated vesicles with 120 nm and caveosomes range between 50 and 80 nm.^[liii] Macropinocytosis is a transient response to growth factors and mitogenic agents

leading to massive membrane internalization from the cell surface via large macropinosomes. The intracellular fate of those vacuoles varies depending on the cell type, but usually they collapse onto and fuse with the plasma membrane. Macropinocytosis does not exhibit any selectivity of the different type of nanoparticles, but it is a key mechanism for the drug nanocarriers delivery.^{[xxxiii][liii]}

1.2.2.2.4 Clathrin- and Caveolae-Independent Endocytosis Pathway

Clathrin- and caveolae-independent mechanism of endocytosis is related to dynamic cholesterol- and glycosphingolipids-rich microdomains having a 40-50nm diameter presented in the lateral plane of membranes that can be captured by, and internalized within any endocytic vesicle.^[lxiii] Those rafts are lipid rich, detergent-resistant areas of the membrane where interacting molecules are destined to be engulfed as part of the intracellular trafficking pathway. Specific ligands, like cholera toxin B, will bind receptors within these lipids rafts and can be taken up either through caveolae-, or through clathrin-independent mechanism, indicating that different types of raft exist, classified for each cell type.^[lxiv]

One strategy for the nondegradative intracellular drug delivery is coating macromolecules to these lipid raft-associated ligands allowing the cellular uptake and vesicular trafficking to non-lysosomal subcellular compartment. Lipid-coated perfluorocarbon nanoparticles deliver lipophilic substances to target cell plasma membrane via lipid raft-mediated pathway.^[lxv] The delivery of the drug-loaded nanoparticles is dependent on the feature of specific ligand-based targeting to the cell surface and undergoes firstly into the plasma membrane with subsequent traffick of the lipophilic substances to the cytosol.

The independent-mediated mechanisms might contribute to dependent-mechanisms. For example, hydrophobically-modified chitosan (N-palmitoyl chitosan, NPCS) nanoparticles are internalized via lipid raft-mediated routes with an increase of the degree of substitution (DS) of palmitoyl groups on the surface of nanoparticles.^[lxvi] With this DS increasing, the CvME become more relevant, growing the quantity of particles internalized. These NCPS nanoparticles are good candidates as a carrier for intracellular delivery of therapeutic agents. However, even with some examples in the literature, the mechanisms that govern the clathrin- and caveolae-independent endocytosis pathways remain poorly understood and need further investigations.

1.2.2.3 Passive Diffusion

Free particles can be internalized through the cell membrane by passive diffusion, a non-metabolic energy phenomenon related to a chemical concentration gradient between intra and extracellular environment. For example, circulating molecules gain access to the brain through the blood-brain barrier by passive diffusion. Due to the tightness of the endothelial barrier, paracellular transport of substances is negligible under physiological conditions and one possible pathway for drugs and other substances enter the brain is the passive transcellular diffusion.^[xxviii]

Another example of the importance of the passive diffusion is the doxorubicin (DOX) delivery system using a di-block copolymer composed of doxorubicin conjugated PGLA (poly(DL-lactic-co-glycolic acid) and PEG (polyethyleneglycol) in human hepatoblastoma (HepG2) cell line. The enhanced uptake of DOX-PGLA-PEG was attributed not only by an endocytosis mechanism but also by passive diffusion of free doxorubicin through the cell membrane.^[lxvii] Doxorubicin was also used to explore the capability of obtained MFNEs (multifunctional nanoellipsoids) as anticancer drug delivery vehicles. MFNEs are novel mesoporous silica-based multifunctional DDS (drug delivery systems) with ellipsoidal morphology using nano-sized Fe₂O₃ as the magnetic core precursor, with modified Stöber processes for silica and mesoporous silica coatings on the core. Passive diffusion process was observed for free DOX as well as for the DOX-loaded carriers; an electrostatic attraction-induced endocytosis by the positively charged surface of MFNEs was involved, which was more effective than the passive diffusion.^[lxviii]

1.2.3 Cellular Toxicity Assays of Nanoparticles used for Radiosensitization

Numerous investigations have shown that slight modification of physicochemical features have great consequences on the cellular entry and biological processes.^[lxix] Different industrial engineered nanoparticles, such as iron oxide, silica, carbon nanotubes, and layered double hydroxides (LDHs) have been reported to be internalized into mice's red blood cells,^[lxx] HeLa cells^{[lxxi][lxxii]} and tumorigenic osteosarcoma MNNG/HOS^[lxxiii] by different internalization mechanisms. The study of the uptake ability of particles with a size range of 1 to 100 nm into cells is directly related to their potential toxicity to human exposure. Nanoparticles are engineered with bioconjugates coatings such as DNA, proteins or specific

antibodies. Non-targeted cells should be preserved from intracellular dysfunctions, as disruption of organelle integrity or gene alterations or even other deleterious features when interactions with cells and subcellular structures are envisaged.^[lxxiv]

Classical toxicology assays for diverse molecules interacting with cells are used for the equivalent processes with nanoparticles. However, due to their composition and particular physiochemical properties, nanoparticles can interact with assay components or even interfere with the detection systems resulting inconclusive data. Thus, to study the nanoparticles behavior in the cells and minimize animal use, various assays are used to valid conclusions about their safety for biomedical applications. Those *in vitro* investigations are the first step in NPs toxicity studies but cannot be substitute to *in vivo* experiments.

A lot of reviews describe the cytotoxic effects of commonly used nanoparticles; those reviews might help for the design of new nanoparticles dedicated to biomedical applications.^{[lxxiv][lxxv]}

In vitro cytotoxicity studies of nanoparticles use diverse cell lines, incubation times, and quantitative assays. Therefore controlling the experimental conditions is crucial to ensure the correct interpretation of the data obtained, i.e., if the measured cell death is a consequence of the nanoparticle introduction in the cell culture or the unstable culturing conditions as absorption or color due to the nanoparticle itself.^[lxxiv]

Three main categories of assays, including cell survival, cell stress, and cell viability will be detailed giving guidelines for enhanced nanotoxicity evaluation of manufactured nanoparticulate materials

1.2.3.1 Cell Survival Assays

Cell survival assays are very useful to determine the cell reproductive death after treatment with nanoparticles. The clonogenic or colony forming assay, one of the main assays, is a test using ionizing radiation to determine the effectiveness of cytotoxic agents.^[lxxvi] Puck and Marcus^[lxxvii] initiated the description of this technique. They used a cell culture technique to test the clone formation ability of single mammalian cells in a suitable medium. The colony formation assay has been used for diverse type of cells; complex culture media and they could detect all cells damaged that may cause cell reproductive death.

The clonogenic assays have been also developed for other systems as for stem cells and for tumor cells in animals. Those studies have settled important information about differences in sensitivity to radiation and chemotherapeutic agents among tumors and normal tissues and modification of the treatment effectiveness.^[lxxviii]

Usually, the clonogenic assay has been chosen to be the optimal assay for discovering survival after radiation. Nevertheless, this technique requires long incubation times to form colonies from isolate cells, and shows poor reliability in cells with low cloning efficiencies or long doubling time. The clonogenic assays were used to attain the dose enhancement ratio required to give the same surviving fraction in the absence or the presence of nanoparticles^[lxxxix]. The ability of cells to form viable colonies was taken into account and the striking cells sensitization to ionizing radiation may have clinical implications for the gold nanoparticles in the prostate cancer treatment. XX *et al.* developed some 50 nm size NPs, manufactured with a yellow polyphenol, curcumin forming a “nanocurcumin”. In a clonogenic assays on MiaPaca pancreatic cancer cells, they demonstrated a significant growth inhibition in presence of 10 to 15 μM of nanoparticles, compared to the irradiated condition alone.^[lxxx]

1.2.3.2 Cell Stress Assays

The objective of the cell stress assays is to identify changes in cellular behavior and non-lethal injuries to cells due to environmental exposure. Different composition and size particles have been shown to create reactive oxygen species (ROS), as C60 fullerenes, carbon nanotubes, and nanoparticles.^{[lxxxii][lxxxiii]} The uptake of those particles by the cell could be seen as a reaction to foreign species including the nanoparticles, an environmental stress generating chemically ROS species such as superoxide, hydrogen peroxide, and hydroxyl.^[lxxxiv]

The quantity of ROS species produced by cells is a consequence of their interaction with the nanoparticles. In general, small and transient increases in ROS can be tolerated by most cell types, whereas higher levels that stay longer in the medium may result in cell damage.^[lxxxv]

Nanoparticles induce ROS species production due their large surface area coated with reactive molecules, giving rise to oxidizing capabilities. The exact mechanisms by which nanoparticles generate ROS are not yet fully clarified, but some explanations could be found in the literature: i) the reactivity of the surface coating of the nanomaterials as polymers, complexing ligands or biocompatible shell produce ROS and oxidative stress;^{[lxxxii][lxxxvi]} ii) nanoparticles mobilize mitochondria, to red-ox active organelles, altering ROS production and interfering with antioxidant defenses, and iii) photoexcitation of nanoparticles releasing oxyradicals that can interact with the antioxidant defenses.^[lxxx]

Ultrafine carbon particles (range size < 100 nm) were investigated by means of their ability to induce oxidative stress in macrophages and epithelial cells. These nanoparticles are

internalized in mitochondria due their small size, where they induce major structural damage and contributed to oxidative stress. These nanoparticles are related to the content of red-ox cycling organic chemicals and their ability to damage mitochondria. The ability to generate ROS renders these nanoparticles more damaging at cellular level and a potential risk to health.^[lxxxvii] The survival cell assays can corroborate the biocompatibility of the nanoparticles, as for example in superparamagnetic iron oxide (SPIO) nanoparticles for cellular magnetic resonance imaging (MRI).^[lxxxviii] For MRI detection, SPIO-containing contrast agents should be internalized to label the cells; the potential toxicity related to SPIO internalization has not yet been studied and require some investigations. The authors performed some ROS assays that can regulate a variety of cellular responses as the ability of SPIO to promote cell growth due to their ability to diminish intracellular hydrogen peroxide (ROS specie) through intrinsic peroxidase-like activity. Thus, the possible evaluation of elevated ROS levels is crucial in the toxicological profile of nanoparticles. It is also important to have accurately assays to determine the maximal ROS levels and if their effects are transient or more long lasting, a key issue for the cell viability and cell death.

1.2.3.3 Cell Viability Assays

Cell viability assays aim to study the cellular metabolism by quantifying the cell response to a particle exposure. Most of these tests involve differential inclusion, exclusion or conversion of an added dye and sensitive pathways indicating apoptotic DNA fragmentation and leakage from cells.^[lxxxix] Assays with dye dependency include the formazan-dye-based assay (MTT), lactate dehydrogenase (LDH) assay and for the fragmented DNA, the comet assay.

MTT assays have been used to measure proliferation, cell viability, and drug cytotoxicity *in vitro* and for radiosensitivity experiment.^{[xc][xci]} In order to distinguish between live and dead cells by detecting damaged plasma membranes, this colorimetric cytotoxicity assay attempts to determine the mechanism involved in an induced cell death. MTT is a simple colorimetric method first developed by Mosmann in 1983.^[xcii] Its process is based on the ability of metabolically active cells to convert this dye to a purple water insoluble formazan in cells bearing functional mitochondria. The formed fluorescent signal can be quantified and the resultant value related to the number of living cells. The MTT process depends on enzymatic cellular activities that may be conducted to modifications during different cellular phases. That assay overcomes the need for cell lines to form colonies because it measures the reduction of tetrazolium salts to a formazan end product and is rapid. Nevertheless, the MTT

assay requires low cell numbers due to non-linear relationship between absorbance and cell number at higher cell densities and is limited by the time required for substrate incubation.^[xciii]

Cytotoxicity assays are performed on a lot of manufactured inorganic nanoparticulate materials including multiwall carbon nanotube aggregates, Ag, TiO₂, Fe₃O₄, Al₂O₃, and MnO₂ with dimensions ranged from 2 nm to few μm.^{[lxxv][cxv]} Results demonstrated that only cells exposed to Ag nanoparticles have their mitochondrial function reduced at 5-50 μg/mL. At the same doses, the other nanoparticles had no observable effect while they present significant toxicity at higher levels (100 – 250 μg/mL). Thus, the data observed on MTT assays suggest that Ag nanoparticles (15 and 30 nm) are highly toxic while Fe₃O₄, Al₂O₃, TiO₂ and MnO₂ displayed no toxicity at the tested doses.

The MTT assays were implemented by means of manufactured nanoparticles in a murine alveolar macrophage cell line, a human lung macrophage and a lung epithelial cell line. It was observed that there is no correlation between the particle morphology with the cytotoxicity response for all the cell lines since a variety of morphologies within the nanorange exhibit equivalent or similar cytotoxicities. However, the difference of sensitivity between cell types and cytotoxicity assays has to be taken into account when assessing nanoparticles toxicity.^[xciv]

For better understanding of the result data, other cell viability assays are necessary. The colorimetric lactate dehydrogenase (LDH) release monitoring based on the oxidation of the yellow tetrazolium salt INT to a red formazan, is traditionally used to evaluate tissue or cell damage.^[xcv] LDH assays using INT as substrate have been performed with various nanoparticles to assess their cytotoxic effect.^{[xcvi][xcvii]} LDH is highly dependent on the pH conditions, being significantly deactivated under low pH conditions, and destabilizing the substrate under high basic pH. However, metal ions have been shown to interfere with the LDH assay and single-walled nanotubes usually do not interact with the substrate INT.^[xcvi]

One example of LDH assay on nanoparticles is the study of 30 nm silica nanoparticles developed by Yo KU *et al.* in mouse keratinocytes.^[xcviii] LDH is an enzyme widely present in cytosol and when plasma membrane integrity is altered or disrupted by nanoparticles uptake, it leaks into media and its extracellular levels elevate depending upon the nanoparticle toxicity. Thus, higher LDH values in the medium indicate higher toxicity levels. Some size-dependent toxicity was observed due to direct physical disruption of membranes through materials interaction or other unknown mechanisms.

Other consequence of the interactions between the nanoparticles and the cell is the DNA damage. This genotoxic potential of the particles can be examined by comet assays^[lxxiv] where the gel electrophoresis is used to detect fragmented DNA. Cells with damaged DNA will appear as a “comet”, with a broken DNA pieces migrating away as a tail in an intact DNA residing head. Comet assays were first discovered by Östling and Johanson in 1984^[xcix] with the objective to analyze DNA strand breaks under neutral conditions. Later, this version was optimized for alkaline version with an increased sensitivity. The cellular studies with nanoparticles show that the majority of the nanoparticles cause DNA strand breaks or oxidative DNA lesions, principally due the high surface area reactivity of many nanomaterials and the sensitivity of the method. Apart of the many factors that can differ between studies, as cell type, dose, dispersion technique and exposure time, the SiO₂ nanoparticles showed no or low increase in DNA damage while CuO and ZnO induced DNA stand breaks.

The measurements of the numbers of DNA damage that occurs during irradiation can determine the radiosensitizing properties of the nanoparticles. Gadolinium-based radiosensitizing nanoparticles designed to efficiently enter into the human glioblastoma radioresistant cell line U87.^[c] By means of the single-cell gel electrophoresis comet assay, gadolinium-based nanoparticles can behave as *in vivo* radiosensitizers in small animals out of the [10-100 keV] range where photoelectric effect is predominant.

Ambiguity results from these diverse assays can be frequently interpreted either as toxicity or adverse reactivity. This is why an assembly of answers from many different assays is central to conclude what type of nanoparticles is suitable for biomedicine use.

1.2.4 Characterization Techniques for Nanoparticles Uptake

Both uptake mechanisms and cytotoxic tests depend on the nanoparticles physicochemical properties. Thus, without good established characterization techniques, the biomedical target applications may not achieve their initial objective.

Among the high quantities of characterization tools, analytical spectroscopy, optical microscopy and electron microscopy seem relevant for a better understanding of the cytotoxicity of nanoparticles and their uptake mechanisms by cells.

1.2.4.1 Analytical Spectroscopy

Quantifying and identifying concentrations of different composition elements of the nanoparticles, inside and outside the cells, is a crucial step to optimize their synthesis.

Inductively coupled plasma (ICP) is used to detect different trace metals in environmental samples by light emitted from elements in the sample. However, ICP is often performed in conjunction with other analytical tools such as Mass Spectroscopy (MS) and Atomic Emission Spectroscopy (AES). The ICP is used as a vaporization/ionization source for inorganic mass spectrometry (ICP-MS) and vaporization/excitation source for atomic emission spectroscopy (ICP-AES).

The ICP-MS is capable to measure trace metal impurities and to follow the nanoparticle uptake process.^{[lxxxix][ci]} The impurities could be deleterious to the biocompatibility of nanoparticles and hide the cell toxicity that could be due the impurities and not to the introduction of the nanoparticles themselves.

To verify the cytotoxicity of 15- and 46- nm silica nanoparticles in cultured human bronchoalveolar carcinoma-derived cells, some ROS and LDH assays were performed^[cii] However, a previous ICP-MS was made to quantify the metal impurity levels in SiO₂ nanoparticles and prevent any misinterpreted toxicity data. The ICP-MS data showed that SiO₂ nanoparticles contain ultra-low levels impurities, indicating no metal trace on the ROS species.

For the internalization studies, a particular example is a hybrid gadolinium oxide nanoparticle developed as cell-labeling tracers. The nanoparticle distribution within cells was analyzed by confocal analysis and the Gd concentration within cells was quantified by ICP-MS.^[ci] There was no observed exocytosis and the amount of particles internalized represented 8% of the cell volume indicating the nanoparticle uptake into human fibroblasts and human adenocarcinoma cell lines.

To determinate the concentration of atoms as such gold or even MnO nanoparticles in cell suspensions, ICP-AES was performed in intracellular uptake of different size and shaped colloidal gold nanoparticles^[ciiii] and in biocompatible MnO nanoparticles T₁ MRI contrast agent for various body.^[civ] However, this technique does not discriminate the size and shape of the nanoparticles before use in cell experiments.

1.2.4.2 Optical Microscopy

As a general rule, light microscopy techniques are still the principal choice for the observation of nanoparticles uptake. With its enhanced resolution and contrast promoted by the fluorescent stains, the confocal microscopy allows the detection of interaction of intracellular

structures as such macrophages and endocytosis characteristic vacuoles with the nanoparticles.^[cv]

Carbon nanotubes with high 700- to 1100- nm near-infrared (NIR) absorbance can be used for optical stimulation of nanotubes inside living cells leading to new classes of novel nanomaterials for drug delivery and cancer therapy.^[lxxiii] Single-walled carbon nanotubes (SWNTs) were mixed with an aqueous solution of Cy3-labeled single-stranded DNA and later exposed to HeLa cells. Confocal images confirmed that the nanotubes were internalized inside the cells as transporters, with an energy-dependent endocytosis mechanism, and that the DNA cargoes from SWNT transporters were released and located in the cell nucleus.

Superparamagnetic iron oxide nanoparticles (SPIO) have been used due their potential applications such as in nanoelectronics,^[cvi] delivery systems for cancer therapy^[cvii] and magnetic resonance imaging (MRI).^[cviii] Post-synthesis coating strategies include the use of silica,^[cix] carboxylate acids,^[cx] and polymers for stabilization and functionalization of the SPIO. In particular, PEG-modified phospholipid micelle magnetite was developed for MRI contrast agent for intracellular measurements of gene expression in deep tissue.^[cxi] Confocal microscopy was applied on both human dermal fibroblast (HDF) and Madin-Darby bovine kidney (MDBK) cells incubated with SPIO for 1 hour, resulting in an intracellular delivery of micelle-coated SPIO in both cell lines. The surface of these nanoparticles provides a flexible platform to which a variety of ligands for cell delivery and targeting can be attached.

Fluorescence microscopy can also be assigned to more understand the nanoparticles uptake by various cancer cells. For example, fluorescent mesoporous silica nanoparticles were used for the delivery of the hydrophobic anticancer drug camptothecin (CPT).^[cxii] Fluorescence microscopy confirmed the cellular uptake of the nanoparticles due the monitoring of the emission of the fluorescein molecules coating. Mainly, the nanoparticles were taken up into the acidic organelles of the cancer cell lines, causing growth inhibition and cell death due the delivery of CPT.

The light microscope (LM) is limited in its resolution to about 0.25 micrometers. If two objects are closer together than that, they blur and cannot be distinguished by the LM. The electron microscope (EM) overcomes this limitation and achieves theoretical resolutions down to 0.2 nanometers, allowing useful magnifications of biological material up to several hundred thousand times. Resolution is governed by the wavelength of illumination, and an electron beam has a much shorter wavelength (about 0.005 nanometers) than visible light (about 400 to 750 nanometers).

1.2.4.3 Electron Microscopy

Thanks to its resolution, various imaging methods and associated analytical tools, electron microscopy constitutes a key technique for characterizing materials and finds fully its relevance in the multidisciplinary field of use of nanoparticles in medicine.

Electron microscopy overcomes the limited resolution of confocal microscopy, widely used in biology, and enables the visualization of eventual nanoparticles agglomeration, their location on the cellular membrane, and their traffic within the cytoplasm.

Transmission electron microscopy (TEM) is an established technique for micro- and nano-imaging where morphological and structural biological mechanisms are observed. The presence of several cytoplasmic protrusions and abundant phagolysosomes containing internalized multi-wall carbon nanotubes (MWCNTs) has been reported by Di Giorgio ML *et al.*^[cxiii] and could be observed by means of TEM. They studied the effects of 0.7 to 2.0 nm single and 2-170 nm multi-walled carbon nanotubes on the mouse macrophages RAW 264.7 cells by TEM for 24h, 48h or 72h incubations time. A phagocytic activity of RAW cellules was increased with both 24h and 48h-treatments and did not produce relevant ultrastructural modifications. However, after 72h, the authors observed apoptotic cells exhibiting disorganized mitochondrial crests, condensed chromatin and a large number of necrotic cells, indicating RAW cell ultrastructural modifications. This occurs because of the fibrous shape of the SWCNT that damages phagolysosomes membranes, dispersing in the cell cytoplasm and across the nuclear envelope. The TEM analyses demonstrated that carbon nanotubes were internalized in the cells by phagolysosomes, indicating the phagocytic pathway. Thus the TEM technique can support the uptake study of nanoparticles into cells and helps to elucidate its particularity for further analysis.

Simon-Deckers A. *et al.*^[cxiv] studied the response of A549 human pneumocytes after exposure to aluminum oxide or titanium oxide nanoparticles or multi-walled carbon nanotubes (MWCNT) using transmission electron microscopy (TEM). They observed A549 thin sections after 6h and 48h to NPs exposure, and 48h to MWCNT. Only 2-3 μm isolated nanoparticles were observed inside cells. If compared with control cells, the morphology of A549 cells changed with their exposure to MWCNT nanoparticles. A549 cells were also exposed to

different kind of nanoparticles. NPs were internalized after 6h of exposure, whatever their chemical composition and size. NPs were observed in the cytoplasm and never inside the cell nuclei; either isolates or inside vacuoles or cytoplasmic compartments as lysosomes, mostly agglomerated and/or aggregated than isolated. After 48h of exposure, all the nanoparticles were found entrapped in lysosomes or inside intracytoplasmic vacuoles. Apparently, the amount of intracellular accumulation was not correlated to NPs size or chemical composition.^[cxiv] Two mechanisms could explain this uptake of the nanoparticles: a) cells would engulf large agglomerates and then dissociate them in their cytoplasm as result of surface-tension-mediated disaggregation of electrostatically or loosely agglomerated particulates^[cxv] or b) nanoparticles would be entrapped in cytoplasmic vesicles as defense reaction by two-independent internalization pathways: phagocytosis and pinocytosis. These pathways could be derived from non-specific interaction of cargoes with plasma membrane or specific linking via membrane receptors. The NPs were accumulated in cells as isolated tubes, and the majority of them localized in vesicles via endocytosis, particularly macropinocytosis due their size.

1.3 Conclusion of Part One

As noticed in part one and to our best knowledge, no studies about internalization pathways of nanoparticles used as radiosensitizers were reported in literature. Knowing the nature of the entry pathway of radiosensitizing nanoparticles into cancer cells and determining their localization within the cytoplasm (near nucleus or other organelles) are nevertheless important aspects to understand furthermore their mechanism of action.

Thanks to its resolution, various imaging methods and associated analytical tools, electron microscopy constitutes a key technique for characterizing materials and finds fully its relevance in the multidisciplinary field of use of nanoparticles in medicine. Electron microscopy overcomes the limited resolution of confocal microscopy, widely used in biology, and enables the visualization of eventual nanoparticles agglomerates, their location on the cellular membrane, their internalization mechanisms, and their traffic within the cytoplasm.

Successful electron microscopy mainly depends on the initial quality and then the preparation of the specimen observed, especially for biological samples. For this reason, a particular attention has to be paid when preparing cells and tissues for electron microscopy observations. These time consuming preparations have to be performed rigorously and are catalogued in a wealth scientific literature detailing specific protocols and numerous excellent books on the preparation steps of biological thin and bulk specimens. A general description of principles and specific experimental protocols used in this work will be detailed in the next part.

2 Part Two. Biological Sample Preparation Protocols for Electron Microscopy Observations

2.1 Introduction of Part Two

Development of preparative techniques to apply the technology of electron microscope to biological problems began about fifteen years after the development of electron microscope by Knoll and Ruska.^[cxvi] Nowadays, protocols of biological sample preparation for electron microscopy are numerous, well established and have been catalogued in reference books (Glauert 1975, Hayat 1981, Pottu-Boumendil 1989, Ayache 2007) including classical protocols and less used variations on the general ones. The protocols described below are based on techniques detailed in these four books.

Natural materials such as minerals and organic matter are trained in a particular environment, in various conditions that we observe in nature. These materials can be studied in their original state or after modification. The original state can hardly be preserved for biological materials usually very hydrated. They have to be always stabilized physically or chemically to support the TEM observations. Regardless of the complexity of the material, its properties and functions, to study biological material, we must master all the stages of preparation techniques used, know the limitations, disadvantages and especially artifacts that can lead to ensure that the analysis reveals well the intrinsic nature of the materials.

The big difference between the materials of physics and of biology is that living systems are dynamic. The cell continuously adapts to its environment. Moreover, biological materials are in liquid solution, which introduces a difference of a point of view of reaction kinetics and interactions between different actors.

Ultrastructural investigations of biological materials using electron microscopy involve three main constraints: sample's stability under vacuum, its thickness and its countenance in water. The first two issues are due to the illumination source of the microscope. Indeed, high vacuum is indispensable for electrons displacement and very small material thickness is essential for electrons transit, even when highly accelerated. The third difficulty, the need to eliminate water before observation, is also very important otherwise ultrastructure will collapse under the electron beam. Problems to be solved when using an electron beam to observe biological samples is well summarized in the "Sample Preparation Handbook for Transmission Electron Microscopy" by Jeanne Ayache *et al.*^{[cxvii][cxviii]} These problems require complex preparation processes to block molecules that constitute the living biological structures, either through

freezing while immobilizing the water (cryo-microscopy) or through the creation of bridges with chemical fixing agents, so as to manufacture long insoluble chains that will enable subsequent dehydration (classical techniques). During preparation, the biological sample will become rigid and appear as a multiphase, organized, non-crystalline material. An overview of classical techniques used to prepare common materials to TEM observations are presented in **Figure 9**. Methodology and principles of each step of the protocol are detailed in paragraph 2.2.

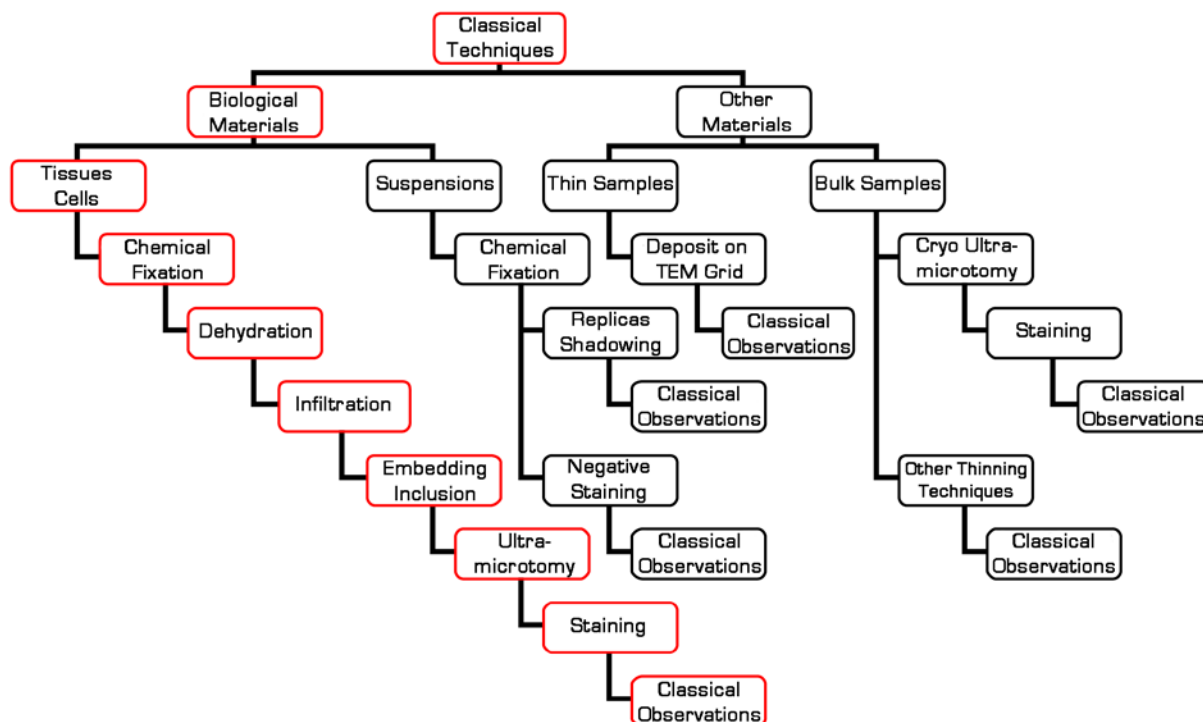


Figure 9: Overview of classical techniques for preparation of materials for classical TEM observations.

Basically, the sample prepared is an animal cell that can be considered as an organized homogenous structure that is not textured. It can be compared to the amorphous materials of materials science. Physically speaking, it is a hydrated gel. It presents a complex functional organization. An outer phospholipid membrane surrounds it, and internal membranes partition it into different compartments called organelles. These are defined by their morphology, size, function, and location within the cell. The intracellular space containing the organelles is called the cytosol or the cytoplasm and it contains many enzymes, ribosomes, and proteins, as well as the cytoskeleton. The main organelles are the nucleus, the Golgi apparatus, the endoplasmic reticulum, and the mitochondria. Most of the organelles in eukaryote cells and the double-layered structure of the plasma membrane were first observed by electron microscopy. DNA replication and messenger RNA synthesis occur in the nucleus, the place where the continuity of the cell's different functions is ensured. Ribosomes, which are either

bound to the endoplasmic reticulum or not, carry out the replication of proteins. The Golgi apparatus is the site of protein-lipid or protein-sugar coupling and acts as a filter for proteins to direct them toward their final destination. Lysosomes specialize in intracellular digestion. Vesicles ensure transport of products (either synthesized or degraded) within the cell or to its periphery so that they can be secreted to the cell's exterior. Cellular compartments are connected to each other and two-way exchanges occur. In transmission electron microscopy, specimens are cut into very thin sections (between 50 and 100 nm) and placed under a high vacuum, precluding examination of living cells. The resolution of transmission electron microscopes, about 0.1 nm, permits fine structural details to be distinguished. Investigation of intracellular structures begins with micrographs of fixed, sectioned cells in which all the cell movements are frozen. Such static pictures of the cell reveal the organization of the cytoplasm into compartments and stereotypic location of each type of organelle within the cell.

Chemical fixation results in a rigid image of a continuous barrier that has long been attributed to the membrane surrounding the cell, but which is in fact a preparation artifact. In biology, observations are made on an organic material that has been profoundly reworked in comparison to the initial living matter. This gives the material a rigid and identifiable structure, but does not help the microscopist to understand its real structure and remodeling. However, by establishing comparisons between different samples that have been prepared using the same protocol, inestimable information can be deduced, and thanks to labeling techniques, the cell's functions can be determined.

Cryo-observations (at low temperatures) are made frequently in a liquid-nitrogen-cooled (77 k) specimen holder. Cryomicroscopy is a technique developed mainly for biological materials and especially for the investigation of isolated particles such as viruses and macromolecules prepared by the frozen hydrated-film technique or the cryo-ultramicrotomy technique (**Figure 10**).

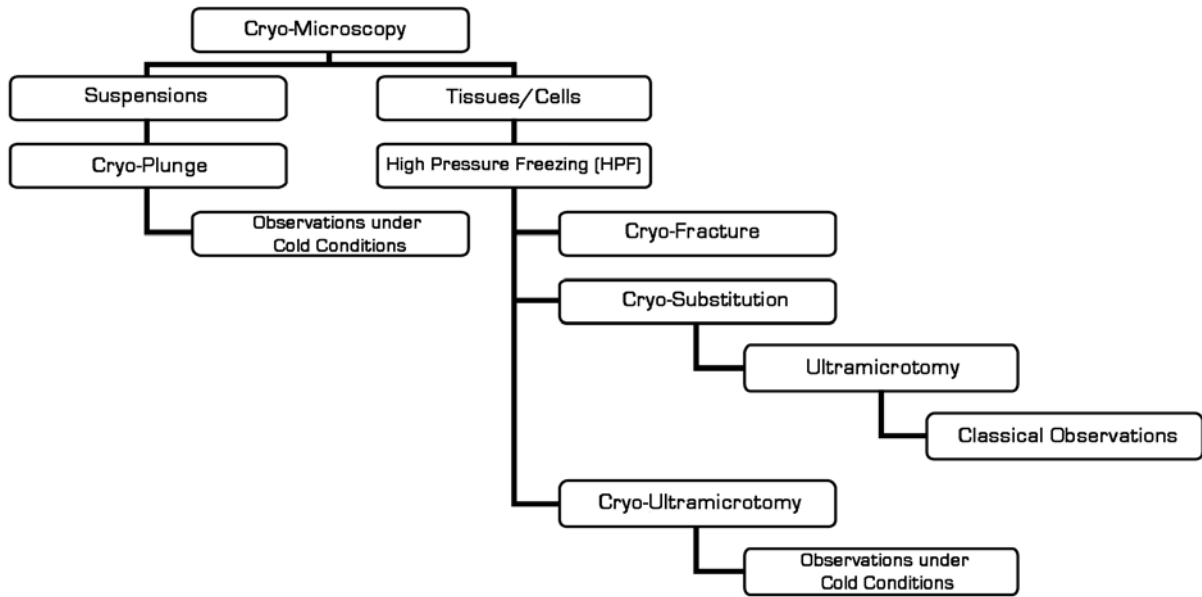


Figure 10: Overview of Cryo-preparation of biological materials for TEM observations under cold conditions.

In addition to the cooled specimen holder, the cryofixed sample itself is cryo-transferred in the microscope in order to be observed under cold conditions. Breaking the cold chain during these transfers must be avoided at all costs, since it leads to ice formation and sample deterioration.

Methodology and principles of each step of the chemical fixation protocol are detailed in the next paragraph.

2.2 Methodology and Principles of Chemical Fixation

Chemical fixation requires the use of chemical solutions to stabilize the biological material. It creates actual chemical bonds between the biological sample and the chemical compound added, which modifies definitively the chemical composition of the material. Fixation should preserve the structure of living tissue with no alteration from the living state. This means that an ideal fixative must also halt potentially destructive autolytic processes at the time of fixation. Furthermore, fixation should protect tissues against disruption during embedding and sectioning and subsequent exposure to the electron beam. Most fixation protocols use two-steps procedure: primary fixation with glutaraldehyde followed by secondary exposure (postfixation) to osmium tetroxide. Indeed, aldehydes are good fixatives for proteins and nucleic acid but they do not fix lipids and phospholipids, which compose the plasma membrane. In some cases, primary fixation can combine glutaraldehyde and a low concentration of paraformaldehyde (up to 4%), which allows more rapid initial fixation of the tissue. Indeed, paraformaldehyde, a monoaldehyde, penetrates tissue more readily than glutaraldehyde does (karvovsky, 1965).

Classical chemical fixation consists in eight steps: (1) primary fixation using glutaraldehyde mixed with buffer, (2) washing, (3) secondary fixation using osmium tetroxide mixed with the buffer, (4) ethylic dehydration, (5) infiltration, (6) embedding, (7) inclusion in EPON resin and (8) curing.

2.2.1 Primary Fixation

Routinely, fixative agents used for pre-fixation of biological matter are aldehydes (paraformaldehyde and glutaraldehyde). They are good fixatives for proteins and nucleic acids. Glutaraldehyde is a dialdehyde with the formula $\text{OHC}-(\text{CH}_2)_3\text{COH}$. It can react twice with the H^+ 's and create bridges between the molecules. Paraformaldehyde is a monoaldehyde of an indefinite formula $(\text{CH}_2\text{O})_n$ ($n = 8-100$), because its degree of polymerization is variable, explaining the n index. Glutaraldehyde can result in artificial bridges between proteins and free amine groups through the addition phenomenon. It also causes a change in protein spatial conformation, which could prevent the detection of enzymatic sites. This is why the use of paraformaldehyde is preferred as a fixative in immunocytochemistry. Paraformaldehyde has just one aldehyde ending. Furthermore, because of this it establishes unstable bonds with proteins, and the paraformaldehyde fixative mix is often supplemented with a weak concentration of glutaraldehyde.

The structure of glutaraldehyde (MW 100.12) is shown in **Figure 11**.

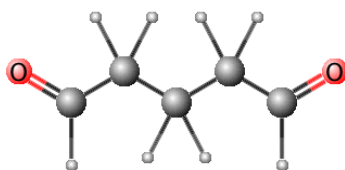


Figure 11: Glutaraldehyde Structure (MW 100.12).

Glutaraldehyde is a five-carbon compound containing terminal aldehyde groups. Glutaraldehyde's attribute as a fixative is in its ability to cross link protein by virtue of the terminal aldehyde groups that make the molecule bifunctional. Specifically, the aldehyde groups react with ϵ -amino groups of lysine in adjacent proteins, thereby cross-linking them. The general reaction, which takes place between protein and glutaraldehyde, is illustrated in **Figure 12**.

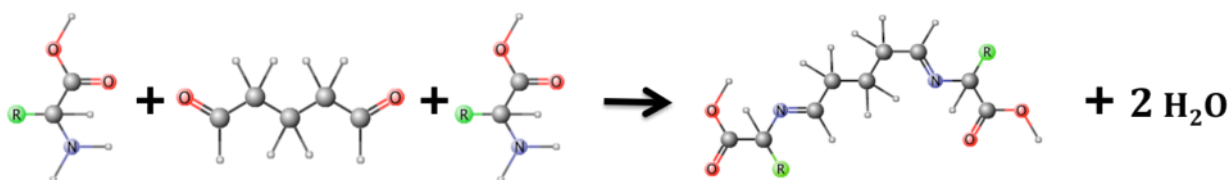


Figure 12: General reaction between protein and glutaraldehyde during primary fixation step.

Taking into account the scale of observation in TEM (on the order of a nanometer), it is essential to respect the physical-chemical characteristics of cellular fluids as much as possible to minimize the movements of water or ions in the tissue and the cells before cross-linking. This is why the fixative will be placed in solution in an appropriate “vector” liquid that aims to reproduce the internal medium of the cells. This entire ensemble constitutes a fixative mixture. The physical chemical characteristics taken into consideration for balancing the vector liquid are pH, molecular concentration, and ionic concentration.

2.2.2 Washing

After primary fixation with glutaraldehyde, the tissue is usually washed in the same buffer vehicle used in the glutaraldehyde fixation step. Because the fixation step is accompanied with H^+ ions release, the buffer pH must be adjusted to the biological one, between 7.2 and 7.4. Washing is extremely important because it eliminates any free unreacted glutaraldehyde that remains within the tissue. Aldehydes remaining from the primary fixation will be oxidized by osmium tetroxide. Some protocols call for one or two 10-minute washes of the tissue in buffer. Unreacted glutaraldehyde will diffuse as slowly outward from the tissue as inward so that a minimum of a few hours of washing with at least three changes of buffer recommended. Residual glutaraldehyde or partially polymerized aldehyde may generate a “peppery” background upon combination with osmium tetroxide. Several rinses with at least overnight wash in buffer will eliminate most of the unreacted glutaraldehyde. It is desirable to fill the vial to the top with buffer to extract as much as glutaraldehyde from the tissue as possible. Washing is usually performed at 4°C.

2.2.3 Secondary Fixation

Aldehydes do not fix lipids and phospholipids, which mainly compose the plasmic membrane. This is why a post fixation with osmium tetroxide (or ruthenium tetroxide) is much recommended. Osmium tetroxide is a powerful oxidant due to its four oxygens (**Figure 13**); it reacts with the double bonds situated between the two carbons, C=C.

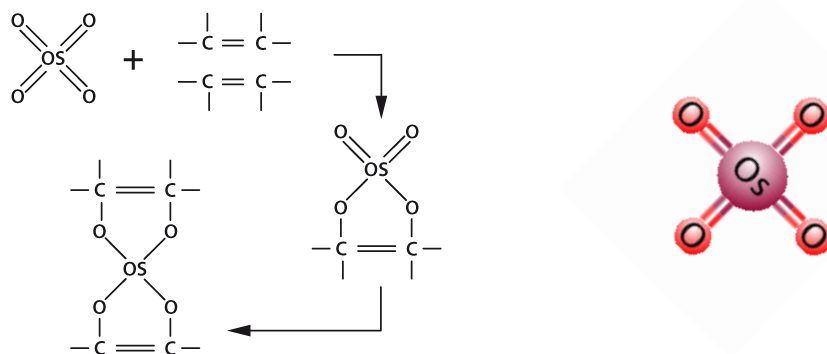


Figure 13: Diagram of Osmium tetroxide.

Osmium tetroxide is a fixing agent for proteins and amino acids; it reacts partially with nucleic acids. It strongly fixes itself in compounds containing double bonds and in particular unsaturated lipids such as the triglycerides and phospholipids of membranes. This last action is represented by the images of unbroken lines that are observed by TEM on chemically fixed membranes. Since osmium tetroxide has a strong affinity for double bonds, it can split up molecules. As it is more soluble in alcohol than in water, it risks dissolving in alcohol during dehydration, causing ruptures in the long protein chains that become soluble. This phenomenon is called overfixing.

Osmium has the advantage of being a chemical element with a high Z. It increases the contrast of the preparation.

2.2.4 Dehydration

Materials containing an aqueous phase cannot be observed directly under the electron beam because of the high vacuum required in the microscope. There are several methods for removing the water contained in a material: by desiccation (passing from the liquid phase to the gaseous phase), by sublimation (passing from the solid phase to the gaseous phase), or by dehydration (replacing the water with a solvent). Desiccation is the simplest method; it consists of letting the water evaporate in the open air at room temperature, but this method destroys delicate biological ultrastructures because it is far from equilibrium between the vapor tension of the water and the pressure of the water vapor that dissipates into the atmosphere.

Desiccation can be conducted correctly only at the critical point (where the two previous pressures cited are equivalent). The water phase diagram shows that the critical point is very high in temperature (647 K) and pressure (221×10^5 Pa), and therefore is technically difficult to reach. The critical point of carbon dioxide is technically easier to reach. This technique is widely used for preparation of bulk biological material for SEM by removing water from the specimen, and replacing it with acetone, which then can be exchanged with liquid carbon dioxide during the critical-point drying process, using a critical point drying apparatus.

Sublimation consists of making ice evaporate. It first assumes the transformation of water into ice through freezing, and then sublimation of the ice. Since the surface tension of the ice is very poor at low temperature, it is necessary to apply a strong depression.

Dehydration that consists of replacing the water with a solvent that can be mixed with water is the most commonly method used for removing water from a sample. The solvent can be allowed to evaporate, because its critical point is easy to reach. Also, the solvent can be replaced (substituted) with a resin that is then hardened.

Therefore there are two possible approaches for treating hydrated samples:

- Saving the water and transforming it into ice, following a purely physical procedure. The material is then directly cut by cryo-ultramicrotomy, or cryo-embedding is done. To carry out the latter, the ice must be eliminated beforehand by cryo-substitution (freeze substitution) or cryo-sublimation (freeze drying).
- Eliminating the water and embedding the sample in order to make it solid; this is a procedure that employs dehydration agents.

Usually, two successive dehydration agents must be used, the first one miscible with water and the second (also called intermediary solvent) miscible with the water and the resin. Common dehydration agents are ethanol or acetone. Ethanol is the most widely used dehydration agent. It is preferred to acetone because this latter is more harmful to organic molecules since it is a more powerful extractor of lipids within the cell. Generally speaking, dehydration agents coagulate proteins and dissolve lipids, unless an appropriate chemical fixation is carried out beforehand. Lipid droplets may appear no homogenous or may have lost their electron density due to dehydration steps. Osmium tetroxide used during tissue fixation will help stabilize unsaturated lipids during the dehydration process.

The general philosophy of the dehydration step is to replace water within the cells/tissues gradually by using graded series of ethanol. Usually 30 or 50 % ethanol is the first solvent cells/tissues are exposed to after secondary fixation followed by 70 %, 80 %, 95 %, and absolute ethanol or acetone. As mentioned before, replacement of the dehydration solution by another intermediary solvent that is highly miscible with the plastic embedding medium is usually necessary to interface with the embedding media. The standard solvent used is propylene oxide. It will also further dehydrate the tissue. Usually more than one change of propylene oxide is necessary to replace the alcohol. Although most embedding media are directly miscible with dehydrating agents, most protocols employ a transitional solvent between the dehydration agent and the resin to speed up the infiltration process.

2.2.5 Infiltration

Infiltration is the process by which dehydration agents or transition solvents gradually replace fluids by resin. Epoxy mixtures are introduced gradually into the tissues block after dehydration. Since it is difficult to make a more or less viscous liquid penetrate cavities or porosities, several mixing bath are carried out with an increasing ratio of resin to solvent. The solvent, propylene oxide, is mixed with the epoxy and placed into vials with the tissue. Gradually, the epoxy-solvent ratio is increased until pure epoxy is used. The pure resin specimens are transferred into molds or capsules containing the resin and are finally placed into an oven where the epoxy components polymerize to form a solid.

Infiltration (and embedding) polymers are mixtures in the liquid state, more or less viscous, which harden through polymerization. Polymerization results from chemical bonds that form between the monomer and one or more hardeners resulting in an intertwining (cross-linking) of the molecules forming a solid network.

There are many infiltration resins available. Besides acrylic resins, epoxy resins are one of the most commonly used for preparation in electron microscopy.

Epoxy resins are generally composed of one or more monomers (mixing resin), one or more hardeners and a reaction accelerator. Classically, the components of an epoxy resin are:

- Mixing Resin: Epons 812 (or substitute)
- Hardeners:
 - o DDSA (dodecenyl succinic anhydride)
 - o NMA (nadic methyl anhydride)
- Accelerator: DMP-10, DMP-30, BDMA (bensyldimethylamine).

The hardness of the Epoxy mixture is controlled by the relative amounts of DDSA and MNS.

For example, to make a medium hardness Epon infiltration and embedding media, we use:

20 mL (24 g) of Resin 812, 22 mL (22 g) of DDSA, 5 mL (6 g) of NMA and 1.4 mL (1.5 g) of BDMA.^[cxix]

Of all the embedding resins, epoxy resins provide the smallest shrinkage rate (2% maximum). Polymerization is uniform but relatively long (from few hours to several days). Their adhesion to most materials is excellent. They are polymerizable under heat (from 57 to 120°C). The last step in the infiltration procedure corresponds to the embedding of the sample.

2.2.6 Embedding or Inclusion

The purpose of embedding using a resin is to enable the biological material to be manipulated and sectioned later. For biological materials, fixed and infiltrated beforehand, embedding resin is the same as that used for infiltration. The sample must present an absolutely clean contact surface free of contaminants and grease or any other dirt, which could prevent the adhesion of the resin around it. The process should not generate a chemical reaction between the resin and the biological material. The resin must be poured (around the sample) in an embedding mold or capsules whose chemical composition does not interact with the components of the embedding polymer. We generally use polyethylene molds whose capsule size fits the ultramicrotome chucks.

2.2.7 Ultramicrotomy Sectioning

Ultramicrotomy is a technique that uses a glass or diamond knife to generate ultrathin slices (30-200 nm) by making a micro-fracture that progressively propagates into the specimen. The crack is induced by the cutting edge of the knife. The sample, which is shaped in a prism, must be hard enough to generate the crack without breaking it into small pieces and plastic enough so that the crack spreads without compression of the specimen. The instrument for performing this technique is called an ultramicrotome. This latter consists of a sample-holder (also called arm) and a knife-support that allows rotation and tilt movements of the knife (**Figure 14**).

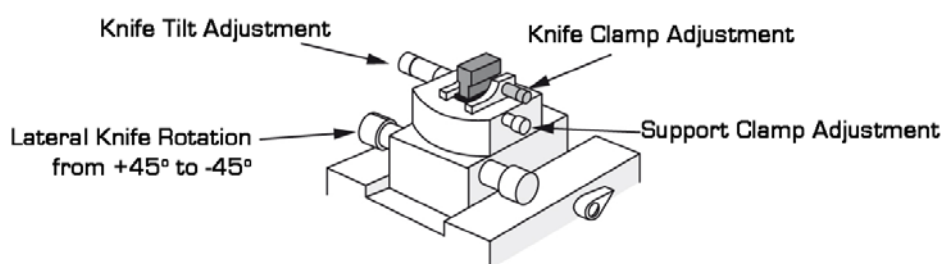


Figure 14: Diagram of the knife holder with main settings.

The sample (in our case a capsule of resin containing prepared cells or tissues) is firmly fixed on the arm that performs either manual or automatic move. This move follows a “D-shaped” trajectory, including a straight-line cutting movement in front of the knife and a lateral clearance. The specimen is cut at a slow rate (generally 1mm/s); the clearance step has a faster rate, with a very small retraction of the arm. At each passage, the arm undergoes an automatic piezoelectric advance, which is programmable between 30 and 200 nm, the knife being immobile. Depending on the cutting thickness required, as well as the sample ductility and brittleness, a glass knife and/or a diamond knife can be used. Diamond knives are recommended to undergo suitable ultrathin sections (thickness < 100 nm) and manufactured with angles varying between 35° and 55°. The larger the knife angle is, the greater the compression on the material will be. Knives with 45° angle are adapted to the average hardness of epoxies used for embedding and are used for routine analyses. Knives used for room temperature ultramicrotomy are usually equipped with a trough filled with very clean filtered water upon which the sections will spread out. The water level in the trough must be

precisely adjusted so as to produce a very low meniscus with the knife cutting edge (**Figure 15**).

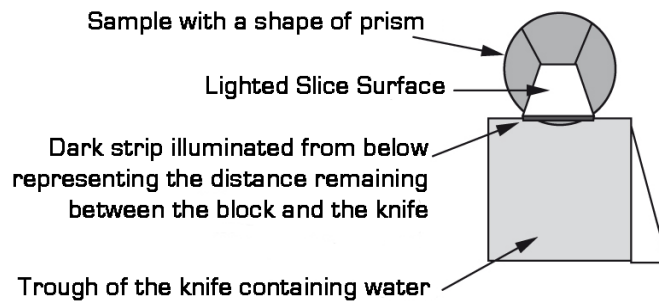


Figure 15: Adjustment of the fine approach of the sample and the knife.

Since biological materials present a poor contrast during TEM observations, ultrathin sections must be stained after the cutting step.

2.2.8 Positive Staining Contrast

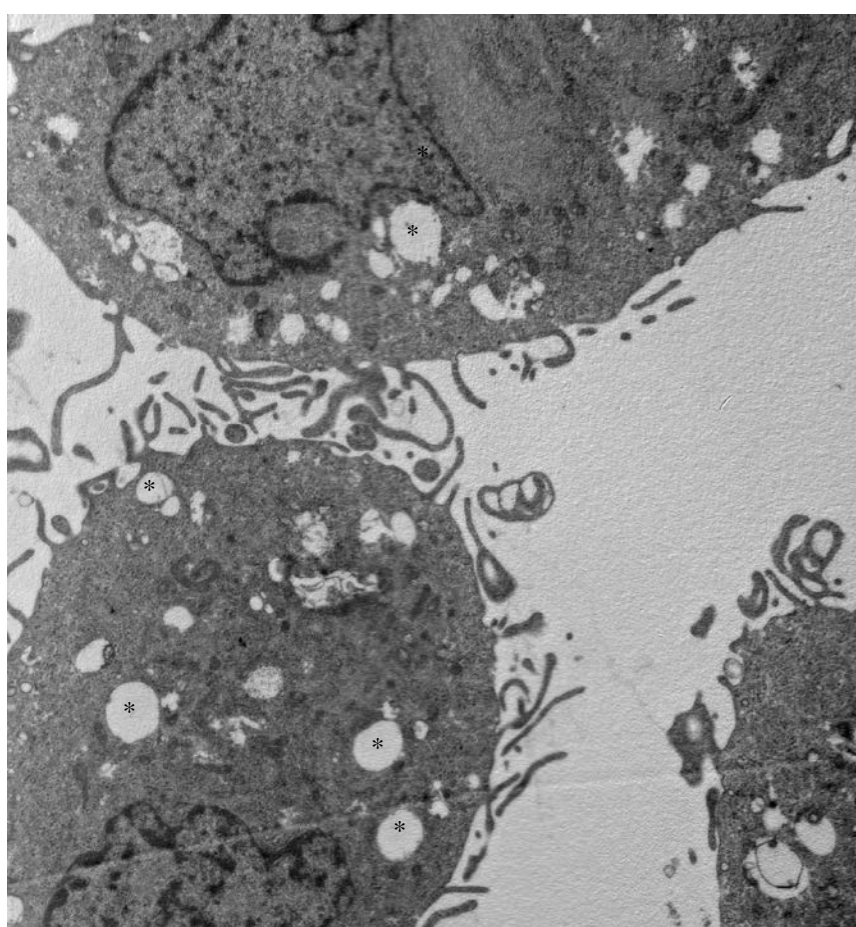
Since image contrast during TEM observations results from variations of electron density within the thin slice of the material, the principle behind positive staining contrast is to make heavy metals react with the structures to be observed in order to stop as large a number of electrons as possible. The addition of this contrast reagent must be selective, i.e., it must act on certain structures and not on others to be able to differentiate them. This contrast is said to be positive in order to differentiate it from another called negative contrast. Positive staining presumes a stable link between the contrast reagent and the structures. Rinsing eliminates excess contrast reagent that has not reacted.

The common metals used as contrast reagents on biological materials are lead (Pb) and/or uranium (Ur). The contrast step is carried out under strict pH and dissolution conditions. Generally, an automatic stainer is used to avoid operator intervention. The mechanism behind the reaction is poorly known and does not appear selective; it appears that it is favored by the prior presence of osmium, for which these contrast reagents have an affinity. In the case of this technique, the sample is chemically modified. Chemical analysis of the sample must take this into account.

2.3 Artifacts in Transmission Electron Microscopy: Main Changes Specific to Biological Materials

All the preparation steps described above denature profoundly the biological material and an artifact can easily be confused with the sample microstructure.

TEM micrographs showed below are examples of the main artifacts induced by: chemical fixation (**Figure 16**), ultramicrotomy technique (**Figures 17, 18 and 19**), the “positive staining” contrast technique (**Figures 20 and 21**) and the substitution-infiltration-embedding technique (**Figure 22**).



Wael RIMA_150.tif
U87 0,6 mM 1h
Cal: 103,196pix/micron
TEM Mode: Imaging

2 microns
HV=200kV
Direct Mag: 7000x
CMES-ST ETIENNE

Figure 16: Bright-field TEM image of a glioblastoma cancer cell, showing a loss of lipids (white holes with asterisks) located in the cytoplasm. The lipids disappeared during chemical fixation. As sectioning was possible, the resin has filled the residual holes, but does not show any contrast.

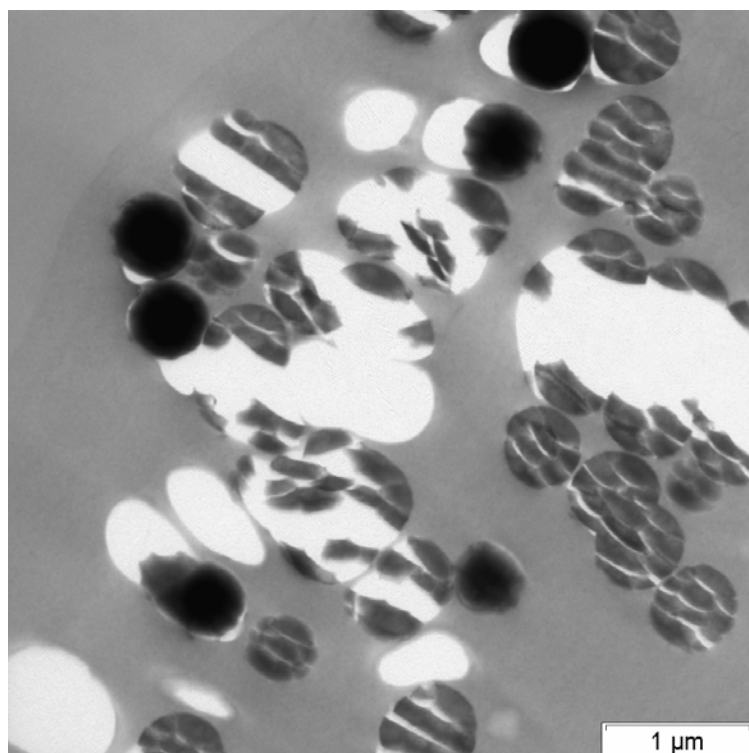


Figure 17: Bright-field TEM image of isolated silica particles embedded in resin and thin-sectioned using ultramicrotomy, showing: (1) tearing due to the difference of hardness of the spheres with the embedding resin, (2) fissures in the spheres, caused by the compression due to the blade followed by a rupture of the material.

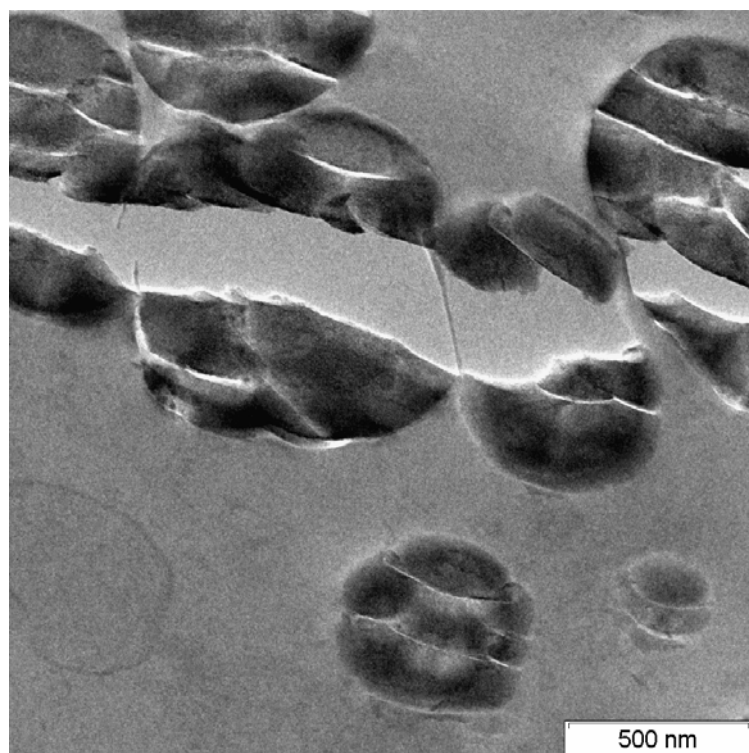
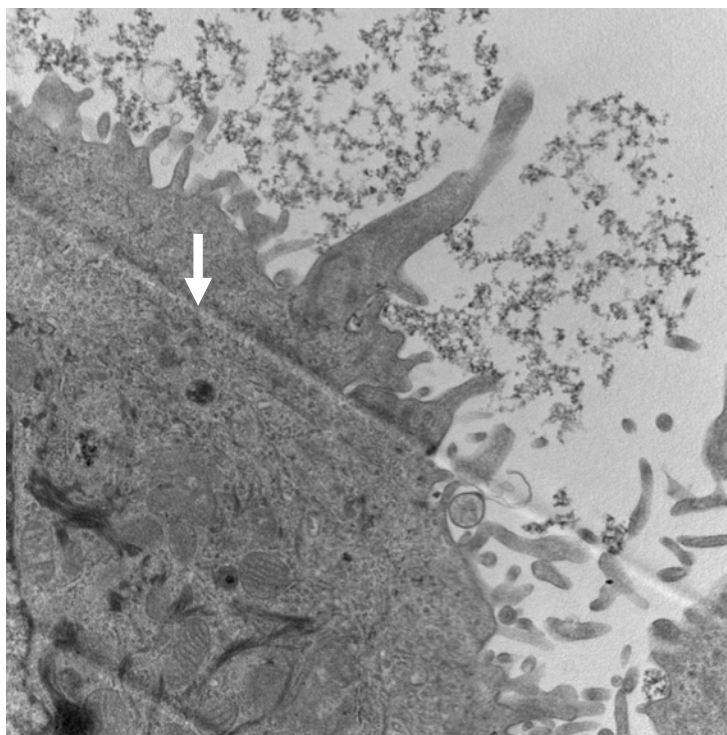
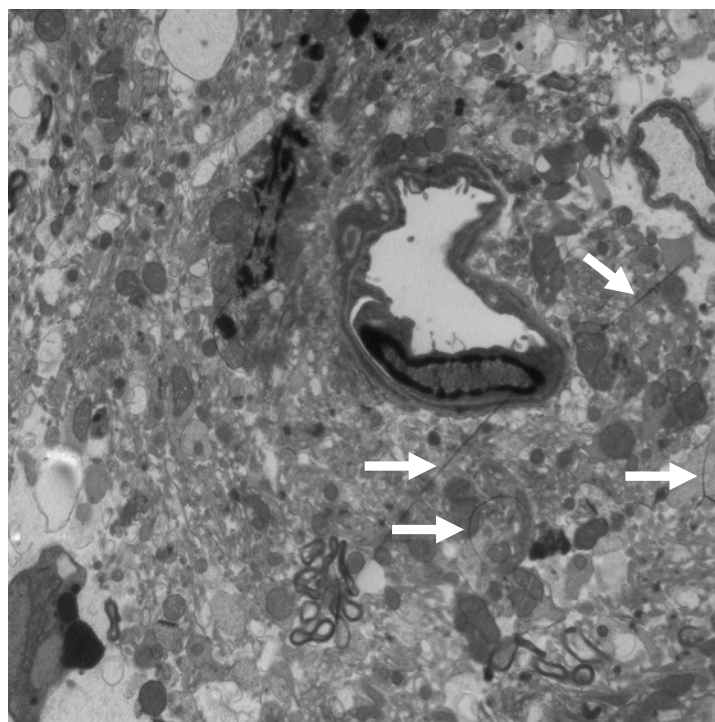


Figure 18: Higher magnification of one area of the previous image, showing fractures and detachments in silica particles. Silica is a hard and brittle material that is difficult to section.



Wael RIMA.395.tif
SQ20B+Gd 2 mM 1h
Lyon Sud
Cal: 176,908pix/micron
2 microns
HV=200kV
Direct Mag: 12000x
CMES-ST ETIENNE
TEM Mode: Imaging

Figure 19: Bright-field TEM image of a cancer cell (SQ20B cell line) embedded in resin and sectioned using ultramicrotomy, showing large knife ridge (white arrow).



Wael RIMA.221.tif
Tumeur R3 20 minutes
Cal: 73,712pix/micron
2 microns
HV=200kV
Direct Mag: 5000x
CMES-ST ETIENNE
TEM Mode: Imaging

Figure 20: Bright-field TEM image of a slice of a rat brain tumor showing needle-shaped uranyl precipitates (white arrows).

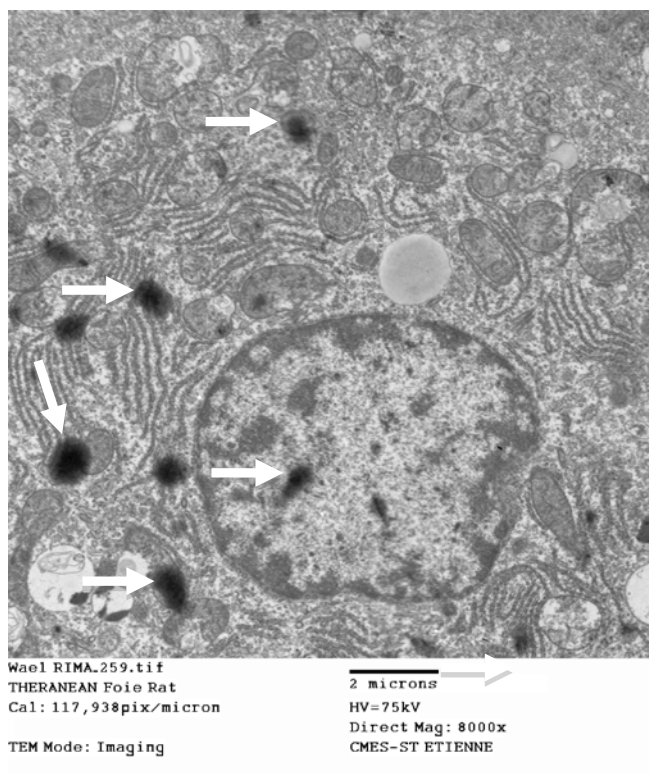


Figure 21: Bright-Field TEM image of a slice of a rat liver showing spherical lead precipitates (white arrows).

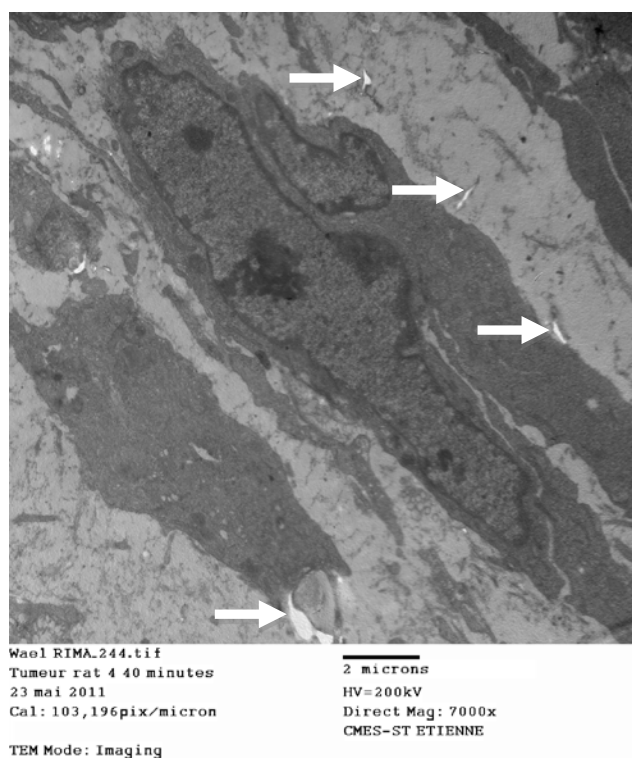


Figure 22: Bright-field TEM image of a slice of rat brain tumor embedded in epoxy resin. This image shows holes in the resin due to incomplete dehydration and embedding (white arrows).

2.4 Techniques Used

2.4.1 Protocol of Sample Preparation for TEM Observations

Biological sample preparation for transmission electron microscopy observations may be classically divided into eight major steps: primary fixation, washing, secondary fixation, dehydration, infiltration with transitional solvents, infiltration with resin, embedding, and curing. **Table 1** shows a basic specimen preparation protocol for TEM commonly used in laboratory.

Table 1: Classical biological sample preparation protocol for transmission electron microscopy.

<i>Activity</i>	<i>Chemical</i>	<i>Time Involved</i>	
		<i>Cells in suspension</i>	<i>Tissues</i>
<i>Primary Fixation</i>	2% Glutaraldehyde + 0.1 M Sodium Cacodylate Buffer	45 minutes several weeks (maximum 1 month)	Several hours to several weeks (depending on the sample's size)
<i>Washing</i>	0.2 M Sodium Cacodylate Buffer	1-12 hours	1-12 hours
<i>Secondary Fixation</i>	1% Osmium tetroxide+0.1 M Sodium cacodylate buffer	1 hour	1-2 hours
<i>Dehydration</i>	30° Ethanol	10-15 minutes	15-30 minutes
	50° Ethanol	10-15 minutes	15-30 minutes
	70° Ethanol	10-15 minutes	15-30 minutes
	80° Ethanol	10-15 minutes	15-30 minutes
	95° Ethanol (2 changes)	10-15 minutes each	15-30 minutes each
	Absolute Ethanol (3 changes)	10-15 minutes each	15-30 minutes each
<i>Transitional Solvent</i>	Propylene Oxide (3 changes)	10 minutes each	15 minutes each
<i>Infiltration of Resin</i>	2/3 Vol. propylene oxide + 1/3 Vol. resin mixture	1 hour	Overnight – 3 days
	1/2 Vol. propylene oxide + 1/2 Vol. resin mixture	1 hour	Overnight – 3 days
	1/3 Vol. propylene oxide + 2/3 Vol. resin mixture	1 hour	Overnight – 3 days
<i>Embedding</i>	Pure Resin Mixture (3 changes)	First change: 12 hours Last two changes: 4 hours each	First change: 12 hours Last two changes: 4 hours each
<i>Curing (at 60°)</i>	Pure resin mixture	1-3 days	1-3 days

2.4.2 Protocol of Sample Preparation for SEM Observations

Many of the steps involved in preparing biological specimens for scanning electron microscopy (SEM) are similar to the initial steps used in preparing samples for TEM. A protocol for preparing specimens for SEM involves rinsing surface to remove debris, stabilizing in a aldehyde fixative followed by osmium tetroxide, rinsing in deionized water, dehydrating, mounting the sample on a specimen holder and coating the specimen with a thin, electrically conductive layer. For bulk biological materials, the specimen is dried using critical point drying technique. **Table 2** shows a basic specimen preparation protocol for SEM commonly used in laboratory.

Table 2: Classical biological sample preparation protocol for scanning electron microscopy.

<i>Activity</i>	<i>Chemical</i>	<i>Specimen: adherent cells</i>
		<i>Time Involved</i>
<i>Primary Fixation</i>	2% Glutaraldehyde + 0.1 M Sodium Cacodylate Buffer	15 minutes-1 hour
<i>Rinsing</i>	0.2 M Sodium Cacodylate Buffer (3 changes)	15 minutes each
<i>Secondary fixation</i>	1% Osmium tetroxide+0.1 M Sodium cacodylate buffer	1 hour
<i>Rinsing</i>	Deionized Water	Quick
<i>Dehydration</i>	30° Ethanol	10 minutes
	70° Ethanol	10 minutes
	95° Ethanol (2 changes)	10 minutes each
	Absolute Ethanol (2 changes)	10 minutes each
	1V absolute ethanol to 1V HMDS	10 minutes
	Pure HMDS (2 changes)	10 minutes each
<i>Metallization</i>		

2.5 Conclusion of Part Two

Biological sample preparation for transmission electron microscopy observations may be classically divided into eight major steps: primary fixation, washing, secondary fixation, dehydration, infiltration in transitional solvents, infiltration with resin, embedding, and curing. Preparation protocol has to be respected carefully to avoid artifacts or sample destruction.

The above-mentioned preparations were systematically carried out to achieve electron microscopy experiments to directly observe nanoparticles/cells interactions. We characterized internalization mechanisms of radiosensitizing sub-5nm gadolinium nanoparticles into radioresistant cancer cells and internalization of submicronic silica nanoparticles in macrophages. The results obtained are presented in parts three and four.

3 Part Three. Internalization Studies of Sub-5 nm Gadolinium-Based Nanoparticles Used as Radiosensitizers

3.1 Introduction of Part Three

Radiation therapy is now an established mainstay for cancer treatment. It benefits thus of intensive study to improve its effectiveness. Two main methods, used separately or combined, exist to optimize radiation therapy and enhance the radiation dose in cancer tissue without delivering intolerable doses to surrounding healthy tissue: (1) the multiport irradiation method, in which the patient is irradiated from multiple directions, and (2) the use of heavy elements that have large photoabsorption cross section.^[cxxx] These high-Z chemicals have been explored on a cellular scale since 1985,^[cxx] and have shown evidence of enhancing radiobiological effects by increasing the production of secondary electrons (Auger electrons) and reactive oxygen species (ROS) that cause strand breaks in the DNA.^{[cxxi][cxxxii]}

More recently, nanoparticles, whose size ranges from a few nanometers to 100 nm, are suggested as promising radiosensitizers because of the possibility to control their affinity or specificity to the target cells or tissues, contrary to chemicals. For example, Fluorouracil (FU), which is commonly used in chemotherapy, is incorporated into cancer tissue. This principle is not sufficient for targeting cancer because FU also accumulates in other actively dividing tissues in the body causing thus side effects.

Among nanoparticles suitable for radiotherapy, gadolinium-based nanoparticles have been very rarely investigated as radiotherapy sensitizers whereas they possess a high $Z=64$. These sub-5nm nanoparticles developed by the LPCML and Nano-H society contain a gadolinium oxide core, a shell encapsulating fluorophores and are functionalized *via* hydrophilic groups such as diethylenetriamine- pentaacetic acid (DTPA) or polyethylene glycol (PEG). They present the advantages of multimodality imaging (optical, magnetic resonance and X-ray imaging) useful to improve diagnoses and, in preliminary trials performed on small animals, have shown their *in vivo* potentialities in radiotherapy.

These particles possess an *in vitro* efficient radiosensitizing effect even at moderate concentration when incubated with head and neck squamous cell carcinoma cells (SQ20B). To further understand this phenomenon and optimize it, we use diverse types of microscopy techniques, in particular electron microscopy that possesses a resolution sufficient to determine the mechanisms responsible for particle uptake.

Article II synthesizes the work done concerning internalization pathways of sub-5nm gadolinium nanoparticles into SQ20B cells and Article III highlights the findings concerning the radiosensitizing effects of these particles on U87 human glioblastoma radioresistant cell line. The last chapter of part three describes a tentative of electron microscopy observations of *in vivo* interactions between gadolinium-based nanoparticles with tumor tissue of rat brain.

3.2 Article II. Internalization Pathways of Gadolinium-Based Radiosensitizing Nanoparticles into Cancer Cells

Wael Rima, Lucie Sancey, Marie-Thérèse Aloy, Emma Armandy, Gustavo B. Alcantara, Thierry Epicier, Annie Malchère, Lucile Joly-Pottuz, Pierre Mowat, François Lux, Olivier Tillement, Béatrice Burdin, Annie Rivoire, Christelle Boulé, Isabelle Anselme-Bertrand, Jérémie Pourchez, Michèle Cottier, Stéphane Roux, Claire Rodriguez-Lafrasse and Pascal Perriat

Status: *Submitted*

3.2.1 Abstract

Over the last few decades, nanoparticles have been studied in theranostic field with the objective of exhibiting a long circulation time through the body coupled to major accumulation in tumor tissues, rapid elimination, therapeutic potential and contrast properties. In this context, sub-5 nm gadolinium-based nanoparticles (GBNs) were developed for imaging-guided radiotherapy. These particles possess an *in vitro* efficient radiosensitizing effect even at moderate concentration when incubated with head and neck squamous cell carcinoma cells (SQ20B). To further understand this phenomenon and optimize it, we use diverse types of microscopy techniques, in particular electron microscopy that possesses a resolution sufficient to determine the mechanisms responsible for particle uptake. Two main cellular internalization mechanisms were then evidenced and quantified: passive diffusion and macropinocytosis. Whereas the amount of particles internalized by passive diffusion is not completely sufficient to induce, *in vitro*, a significant radiosensitizing effect, the cellular uptake by macropinocytosis, which is only significant in a limited range of GBNs incubation concentration, may lead to a successful radiotherapy. Macropinocytosis processes in two steps: formation of agglomerates at vicinity of the cell followed by recuperation of the agglomerate by the lamellipodia (i.e. the “arms”) of the cell. The first step is strongly dependent on the physicochemical characteristics of the particles, especially their zeta potential that determines the size of the agglomerates and their distance from the cell, which are the parameters that render possible their collect *via* the lamellipodia. These results pose interesting challenges for systemic use of GBNs. They should permit to control the quantity of particles internalized in the cell cytoplasm, promising thus ambitious opportunities towards a particle-assisted radiotherapy using lower doses of radiation.

3.2.2 Introduction

Nanoparticles for diagnosis and therapy applications have been suggested over the past few decades^{[cxxxiii][cxxxiv]} because they can present the following advantages: (i) colloidal stability in the blood system to avoid macrophage uptake, (ii) multimodality (the possibility to gather in the same object different properties), and (iii) the capacity to be concentrated in tumors or diseased zones either by Enhanced Permeability and Retention (EPR) effect^{[cxxxv][cxxxvi]} or by the use of targeting biomolecules.^{[cxxxvii][cxxxviii][cxxxix]} The particles suitable for enhancing the radiotherapy efficiency should contain elements with high atomic number Z capable to intensify the production of secondary and Auger electrons or reactive oxygen species (ROS).^[cxxx] Among them, two types of nanoconstructs are presently emerging. Besides gold-based particles^[cxxxii] that were first and widely studied in particular by Hainfeld *et al.*,^{[cxxxii][cxxxiii]} gadolinium-based nanoparticles (GBNs) offer an innovative approach due to their high Z ($Z = 64$) and their capacity to act, *in vivo* and *in vitro*, as powerful contrast agents in Magnetic Resonance Imaging (MRI).^{[xv][c][cxxxiv][cxxxv][cxxxvi]} These multifunctional particles are composed of a gadolinium oxide core and a polysiloxane shell encapsulating fluorophores (Cy5.5) and are functionalized *via* negatively charged diethylenetriamine-pentaacetic acid (DTPA).^{[ci][cxxxvii]} Although photoelectric effect is maximal in the [50-100] keV range, these particles were demonstrated by means of 3-(4,5-dimethylthiazol-2-yl)-2,5-diphenyl tetrazolium bromide (MTT) assays to possess efficient *in vitro* radiosensitizing properties regarding glioblastoma U87 cell line for energies comprised between 660 keV and 6 MeV (Supporting Information). Similarly, these nanoparticles also revealed exceptional radiosensitizing properties using clonogenic assays regarding radioresistant SQ20B human head and neck squamous cells carcinoma cell line (**Figure 23-A**). In both cases (U87 and SQ20B cells), the most efficient radiosensitizing content of GBNs was obtained *in vitro* for moderate incubation concentrations comprised between 0.4 and 0.7 mM in gadolinium (Gd) (i.e. 40 to 70 μ M of nanoparticles). In a previous paper,^[c] we explained this fact by, beyond this threshold, the formation of agglomerates sufficiently large to absorb the killing species and impede them to attain DNA. Therefore, for a better comprehension of this concentration dependence, it is now essential to identify the uptake mechanism of particles into cancer cells with the aim to better control their cellular internalization, provide a feedback for their design and enhance their radiosensitizing effect.

Because of their similar size, nanoparticles (NPs) uptake can follow the same endocytic routes than biological entities such as proteins, viruses or DNA. As a general rule, cellular transport of macromolecules undergoes endocytosis pathways that include phagocytosis, macropinocytosis, clathrin-dependent endocytosis, caveolin-dependent endocytosis and clathrin/caveolin-independent endocytosis.^{[lvii][cxxxviii]} Besides these main pathways, isolated NPs can be internalized through the cell membrane by passive diffusion. This latter consists in a non-metabolic energy phenomenon, related to a chemical concentration gradient between intra and extracellular medium.^[xxviii] The different mechanisms of internalization differ regarding to the size of the endocytic vesicle, the nature of the entering species and the eventual need of specific receptors.^[xxvii] Numerous investigations have showed that slight modifications of physicochemical features have great consequences on the cellular entry and biological processes.^{[xlii][cxxxix][cxl][cxli]} For example, mesoporous silica particles with a diameter of 110 nm were taken up, in presence of human cervical (HeLa) and lung epithelial (A549) cancer cells, *via* a macropinocytosis pathway, evidenced by the presence of membrane ruffling and large cytoplasmic vesicles (macropinosomes).^[cxliii] For 60 nm biodegradable polymeric micelles, the entry pathway in liver hepatocellular (HepG2) cells occurs *via* an unspecified endocytic pathway and a small dose of passive diffusion.^[cxliiii] Concerning the particles with a size inferior to 30 nm, the uptake mechanisms varies even more with their size, morphology, electrical charge as well as the cell type investigated. In many cases, more than one mechanism can be observed (competitiveness of mechanisms). For instance, in the case of internalization of sub-20 nm titanium dioxide nanoparticles into prostate PC-3M cancer cells, no endocytic pathway was privileged so that particles were found to enter either by clathrin-mediated endocytosis, caveolin-mediated endocytosis or macropinocytosis.^[xliii]

The objective of this paper is thus to understand why the maximum of the radiosensitizing efficiency of sub-5 nm GBNs observed for different cell lines relies on an incubation concentration of about 0.6 mM Gd. This will be made by carefully studying the cellular uptake of particles in head and neck squamous cell carcinoma (SQ20B) cells *via* different techniques. SQ20B cell line was chosen for its radioresistance (Survival Fraction at 2 Gy = 0.72) and the high incidence of this tumor type.^{[cxliiv][cxlv]} In this study, the particles chosen correspond exactly to those used in our more recent works upon radiotherapy.^[c] They possess a reduced thickness of polysiloxane shell to limit the presence of inactive matter for radio enhancement. We demonstrate in this paper that these non-targeting sub-5 nm GBNs enter in SQ20B cells by two main mechanisms: by passive diffusion of isolated nanoparticles and, in a

greater amount, by macropinocytosis. Macropinocytosis is rendered possible by the agglomeration of GBNs in solution at vicinity of the cell. The agglomeration state has been evidenced by Fluorescence correlation spectroscopy (FCS). It strongly depends on the concentration, especially the size of the agglomerates and their distance from the cell. This explains why, according to the concentration, particles collect by the macropinocytosis lamellipodia (i.e. the “arms” of the cell) is possible or not. Indeed, only for concentrations around 0.6 mM, the agglomerate size and their distance from cell are small enough to enable their significant recuperation by cell lamellipodia. Therefore, we demonstrate that, in addition to the hypothesis already formulated to explain the exceptional radiosensitizing effect demonstrated for incubation concentrations around 0.6 mM, this effect should be first correlated to the quantity of particles accumulated in the cell cytoplasm.

3.2.3 Results and Discussion

3.2.3.1 Need of a Microscopic Study to Understand the Correlation Between Internalization and Radiotherapy Results

Extracellular and intracellular gadolinium contents in different cell lines (SQ20B, U87 and Human T Lymphocytes LTH) were first estimated using the macroscopic Inductively Coupled Plasma (ICP) technique. The quantities of gadolinium attached to the cell were shown to differ according to the cell line used. Gd content in U87 and SQ20B is found to increase almost linearly with nanoparticles concentration and is significantly higher than that measured in healthy T lymphocytes, which are able to internalize only a very weak amount of GBNs (Figure 23-B). This indicates that, unlike the latter, SQ20B and U87 cells display a large permeability that favors internalization in large proportion and are then relevant cell line models. Gd uptake is not expressed in pg/cell (the unit directly given by ICP measurements) but in mmol per liter of cells (mmol/L or mM), which is feasible knowing the size of the cell. It is then possible to use the same unit (mmol/L) in the incubation medium (per volume of solution) and in the cells (per volume of cell). Concerning SQ20B cells, Gd concentration is found 17 times greater in the cells than in the solution so that the almost linear law between the gadolinium content in the solution and in the cell is not affected by the change in cell viability that occurs for concentrations higher than 1 mM (Supporting Information). Thus, this accumulation of Gd particles reveals that the cells, dead or alive, should act as gadolinium

pumps from the incubation medium towards the cell. This is beneficial for further association with radiotherapy since it implies that a significant amount of radiosensitizers can accumulate in tumor cells. In particular, particles appear as better candidates than molecules for clinical applications since, in comparable conditions, complexes of gadolinium Gd-DTPA (Magnevist[®]) accumulate less (around only 6 times) within the cells.

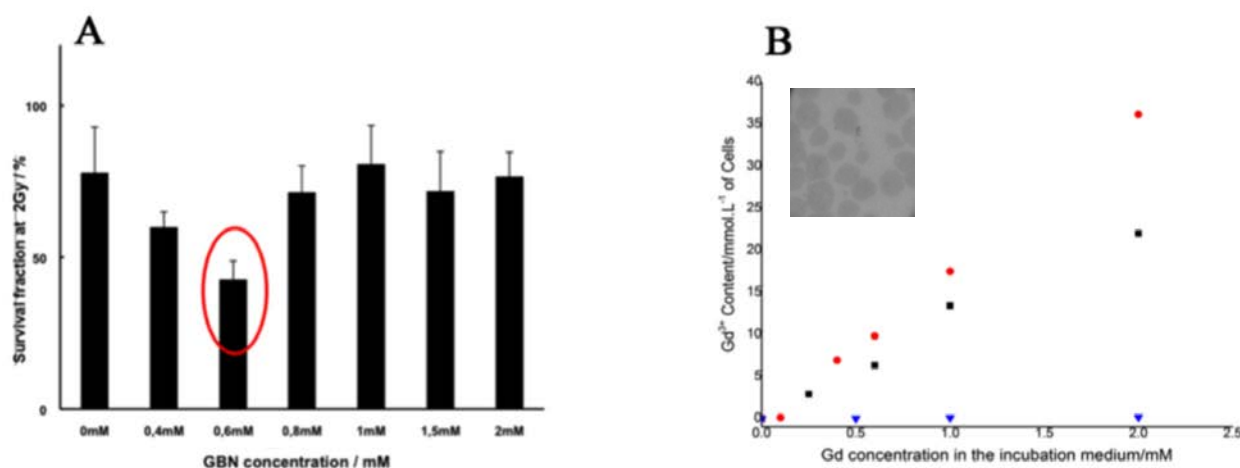


Figure 23: A) Percentage of surviving cell determined by clonogenic survival assays after a 2 Gy irradiation for different Gd incubation concentration; B) ICP quantification, after prolonged cell washing, of extracellular and intracellular gadolinium contents in SQ20B (circles), U87 (squares) and LTH (triangles) cell lines.

Surprisingly, the efficient concentration of nanoparticles for radiosensitizing effect (≈ 0.6 mM, as stated in Figure 23-A) does not match with the maximum concentration of internalization (Figure 23-B), which, in the case of SQ20B, is found by ICP to be equal to 2 mM (after 2 mM, the quantity of particles internalized decreases). Such a phenomenon was already observed in the case of the other type of tumor cell line studied, U87 (Supporting Information). To explain this discrepancy, we now hypothesize that it could be assigned to a difference in the GBNs location within the cell related to the incubation concentration. Indeed, the particles that are quantified by ICP can lie within the cell at close proximity of DNA or, on the contrary, at cell surface far from the cell nucleus. Since the killing species resulting from X-ray/particles interactions (Auger electrons, ROS...) have a mean free path in the cell of only a few hundreds of nm (to be compared with the SQ20B size of around $15 \mu\text{m}$), the location of the particles within the cell seems very important. The macroscopic concentration given by global chemical analysis is then not sufficient to appreciate the radiosensitizing efficiency of the particles and a GBNs classification according to their location in the cell requires observations at a smaller scale. This was achieved using confocal

microscopy whose resolution is submicron (a few hundreds of nm). However, (i) to make the distinction between particles agglomerates and single particles (size < 5 nm), (ii) to establish histograms of agglomerates size distribution or (iii) to precise the particles location among the different compartments of the cell, electron microscopy is needed. In fact, even if single particles can be easily imaged when they are isolated (i.e. simply deposited on a carbon grid), they become indiscernible when they are internalized in cells. This complication is due to the absence of particles contrast when these latter are observed within a cell sample with a thickness of 70-80 nm. Electron microscopy will be then principally used for agglomerate observation and determination of agglomerate size distribution within the cytoplasm. On the contrary, confocal microscopy will be applied to determine quantitatively the concentration of single particles in samples.

3.2.3.2 Particle and Cell Characterizations

Before studying the interactions between particles and cells, these entities were separately characterized.

3.2.3.2.1 Particle Characterization

Concerning GBNs that consist of core (gadolinium oxide)-shell (polysiloxane) particles functionalized *via* diethylenetriamine-pentaacetic acid (DTPA) ligands, their morphology was first studied by different techniques such as Photon Correlation Spectroscopy (PCS), Fluorescence Correlation Spectroscopy (FCS) and transmission electron microscopy (TEM). The hydrodynamic size distribution of the gadolinium oxide cores was measured in DEG after their synthesis for a concentration of 15 mM. The distribution is characterized by an average diameter of 1.1 ± 0.1 nm and a mean standard deviation of 0.4 ± 0.1 nm (**Figure 24-A**). After polysiloxane encapsulation and functionalization, the GBNs possess an average diameter of 2.9 ± 0.2 nm and a mean standard deviation of 1.3 ± 0.1 nm (Figure 24-B). Particles sizes were also measured by FCS thanks to some Cy5.5 molecules that are covalently encapsulated within the polysiloxane shell. FCC measurements were performed in different solutions: water, cell culture media (DMEM) and incubation media (HBSS) for GBNs concentrations ranging between 0.1 and 100 mM, immediately or 90 min after particle dilution in solution. FCS, which is commonly used to characterize the dynamics of fluorescent molecules in solution, deduces particles size from the fluctuations of the fluorescence intensity related to particle diffusion in the solution. Figure 24-C summarizes the results obtained: it shows that

the FCS size is, regardless of the conditions used, close to 2.4 nm and does not depend on particle concentration nor on the nature of the solution. The size determined by FCS (2.4 nm) is in good agreement with that obtained by PCS (2.9 nm). This means that agglomerates formation is never observed in absence of cells and that the colloidal solutions possess an exceptional stability in water and DMEM culture media. This stability is also confirmed by the FCS measurements performed 90 min after dilution since they show again a complete absence of particle agglomeration. Finally, particles were observed by TEM to confirm the information given by PCS and FCS (insets in Figures 24-A and 24-B). High Resolution TEM ($\times 600000$) performed on cores alone confirms their size (1.2 nm), which is in excellent agreement with the average diameter found by PCS (1.1 nm). It shows also that the cores are well crystallized since parallel planes with an inter-reticular distance of 0.311 nm are clearly visible in the inset of Figure 24-A. This distance corresponds to the inter-reticular (222) distance of the Ia3 gadolinium oxide structure (cell parameter: 1.082 nm). Concerning core/shell particles, conventional TEM at lower magnification ($\times 100000$) confirm the architecture of the particle since the image in the inset of Figure 24-B shows effectively a core (inner dark zone) surrounded by a shell (outer grey zone). All these results confirm that the particles studied possess a size below the 5 nm range which renders them particularly attractive for further *in vivo* studies, such small particles being excreted by the renal route. [exlvi]

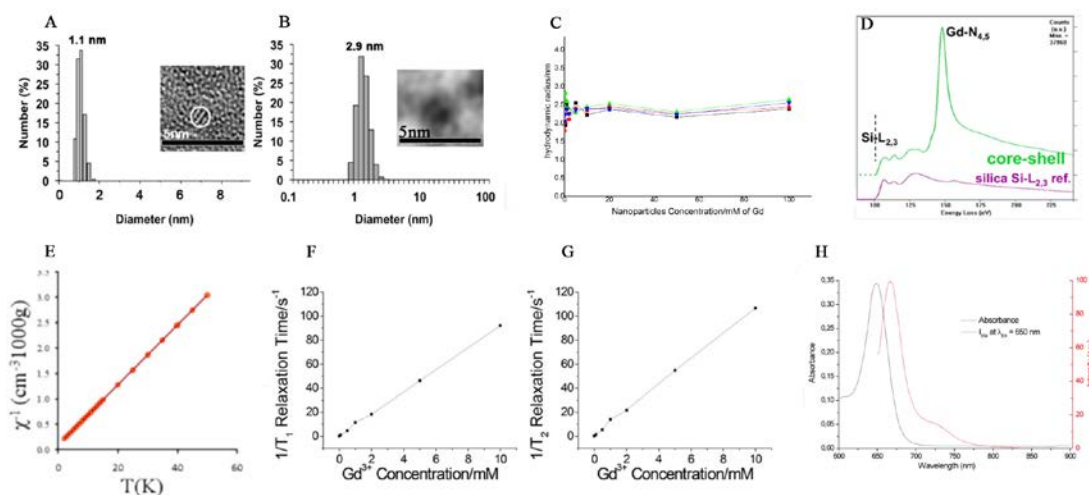


Figure 24: Particle Characterization. A) Hydrodynamic size distribution of gadolinium oxide cores determined by PCS at 15 mM before polysiloxane coating with in inset related HRTEM image; B) Hydrodynamic size distribution of the core-shell particles studied determined by PCS at 15 mM with in inset related TEM image; C) FCS experiments for particle concentration varying from 0.1 to 100 mM in different solutions (in water or HBSS 5 and 90 min after particles dilution): water 5min, green - water 90min, blue - HBSS 5min, black - HBSS 90 min, red; D) EELS spectra of core-shell particles exhibiting Si-L₂₃ and Gd-N₄₅ edges after background subtraction; E) Curie plot of the core-shell particles showing a Neel temperature at 0.1K; Inverse of longitudinal F) and transversal G) relaxation time as a function of Gd concentration; H) Absorbance (black spectrum) and fluorescence emission spectrum (in red) with an excitation at 650 nm for GBNs with cyanine 5.5 covalently grafted on polysiloxane. The emission takes

place near infrared region. (Figures 24-A, 24-B and 24-D were reprinted with permission from G. Le Duc et al., ACS Nano. 2011, 5, 9566. Copyright 2011, American Chemical Society).^[cxxxv]

Electron Energy Loss Spectroscopy (EELS) analysis (Figure 24-D) performed on the GBNs confirm the presence of Si and Gd in the nano-construct thanks to the spectrum that displays two peaks located at 102 and 149 eV and corresponding to the Si-L₂₃ and Gd-N₄₅ transitions. Additional chemical analyses showed that each particle contains 20 % mass of Gd so that the Gd concentration of the particles is equal to: $c_{Gd/particle} = 2.8 \cdot 10^{-12} \text{ mmol}/\mu\text{m}^3$ (2.8 $\cdot 10^{-12}$ mmol of Gd per μm^3 of particles). Moreover, the particles are paramagnetic at room temperature as inferred from the Curie plot (Figure 24-E) that shows that the Néel temperature related to the antiferro/paramagnetic transition is equal to 0.1 K. This relatively low value for T_N, compared to 18 K in macroscopic samples is entirely explained by the small size of the particles.^[cxlvii]

Particles relaxivities (Figures 24-F and 24-G), measured at 60 MHz after dispersion in aqueous solutions containing NaCl (0.9%), are equal for r_1 to 9.15 $\text{mM}^{-1} \cdot \text{s}^{-1}$ (a value similar to that of DOTA (Gd), one of the most frequently used MRI contrast agent (Dotarem®) and for r_2 to 10.6 $\text{mM}^{-1} \cdot \text{s}^{-1}$. Particles are also luminescent as shows Figure 24-H that displays their emission spectrum for an excitation at 633 nm. The spectrum presents a peak at 695 nm, the same value than does a solution of pure Cy5.5, which indicates that the fluorophores encapsulation in polysiloxane does not alter the main characteristics of the luminescent ligand. The magnetic and optical properties so evidenced confirm that the particles studied are effectively attractive for further *in vivo* studied, the following of the particles in the blood stream and their accumulation in tumors being possible by both optical and Magnetic Resonance Imaging. Finally, one of the most important parameter characterizing the particles is the value of their zeta potential at pH 7.4: $\zeta_{pH 7.4} = -8 \text{ mV}$. This value is negative as expected from the presence on particles surface of DTPA ligands characterized by low pK_{AS}. In addition to the entropic repulsion, the colloidal stability of the solution is then also ensured at pH 7.4 by an electrostatic repulsion between the particles. Also the isoelectric point, corresponding to the pH for which the zeta potential is equal to 0 mV is equal to: pH_e = 6.6 ($\zeta_{pH 6.5} = 1 \text{ mV}$; $\zeta_{pH 6.6} = -1 \text{ mV}$) (data not shown).

3.2.3.2.2 Cell Characterization

The objective to quantify precisely the particle quantities that have been internalized within the cells requires the knowledge of the cell size distribution. The determination of this distribution has been performed using electron microscopy observations of resin samples (70

nm thin sections prepared by ultramicrotomy) containing some slices of cells. Due to the nature of the objects examined, the diameter of a so-cut cell slice is not equal to the cell diameter (the value of interest) but inferior or, at best, equal to it. Therefore, when measuring a size distribution from several images of the cells, one obtains the size distribution of the cell sections and not that of the cells, which is the distribution searched (for instance, in the case of a *homogeneous* size distribution of cells with a diameter \bar{D}_{cell} , $\bar{D}_{cell} = \frac{4}{\pi} \bar{D}_{cell\ section}$ with $\bar{D}_{cell\ section}$ the average diameter of the cell section i.e. the diameter experimentally obtained). It is then necessary to establish a mathematical formulation that permits to obtain the size distribution of the cells knowing that of the cell slices (Supporting Information). In the case of SQ20B cell line, the cells are shared between two distinct populations and are described by two Gaussian distributions, a first distribution with an average diameter of $\bar{D}_1 = 12.5 \mu\text{m}$ and a mean standard deviation of $\sigma_1 = 2 \mu\text{m}$ and a second distribution with an average diameter of $\bar{D}_2 = 16 \mu\text{m}$ and a mean standard deviation of $\sigma_2 = 2 \mu\text{m}$. Very striking is that the ratio of the average volumes of the two populations (\bar{V}_1 and \bar{V}_2) is equal to : $\frac{\bar{V}_2}{\bar{V}_1} = 2$. This ratio is perfectly consistent with the 24 h cycle followed by each cell (with a volume \bar{V}_2). Indeed, the cycle contains a mitosis phase corresponding to a division into two daughter cells with half volume (\bar{V}_1). The facts that the mean standard deviations relative to both populations (the cells before and after mitosis) are small and that the volume ratio is exactly 2 indicates that, during the cycle, both division and growth processes should occur rapidly (the proportion of cells with intermediate volumes comprised between \bar{V}_1 and \bar{V}_2 being almost negligible). Even if the duration of the growth process (G_1) is of about 9 h, this is perfectly true for the division process (M) that lasts only 30min (Supporting Information for additional data upon the cell cycle).^[cxlviii]

3.2.3.3 TEM Observations of Nanoparticle Cellular Uptake as a Function of Concentration and Incubation Time

3.2.3.3.1 Lecture Key of TEM Micrographs

After particles incubation with cells, samples were prepared for TEM analysis. A careful examination of more than 300 images confirms that, the sub-5 nm single particles are not

visible regardless of the magnification used (from 120000 to 1000000). As illustrated in **Figures 25-A, 25-B and 25-C** that display diverse cell zones, only agglomerates with a size comprised between 150 and 900 nm can be imaged. Since the cells have been stained by different heavy metals, it is crucial to verify that the agglomerates observed correspond to the internalized particles (osmium tetroxide for instance leads very often to 5 nm clusters that can gather in certain cell compartments). This has been made by performing additional electron imaging using Energy Filtered Transmission Electron Microscopy (EFTEM), a technique particularly suitable for lanthanide identification. Selecting the only electrons that have lost 150 eV in the thin sample observed (150 eV corresponds to the Gd-N₄₅ transition), it is possible to specifically image the zones rich in gadolinium, i.e. the GBNs. Figures 25-D and 27-E display the images of the same cell, one taken with a conventional electron microscope in bright field conditions and the other obtained in filtered conditions i.e. by electrons that have lost 150 eV. Due to a sufficient contrast, this latter image has not been corrected from the contributions of the pre and post N_{4,5}-edges. Whereas the agglomerates appear in black in the image of Figure 25-D (revealing that these latter certainly contain heavy elements), they are clearly brighter in Figure 25-E. This means that, as expected, the agglomerates contain a high content of gadolinium and have been formed by the gathering of several GBNs. This result has been reinforced by Energy Dispersive X-ray spectroscopy analyses. Indeed, these latter have systematically evidenced that, when the electron beam is focused on the agglomerates, some of the X-rays emitted are characteristic of the electron transitions of Gd (L α 6.056 keV, M 1.185 keV) (data note shown).

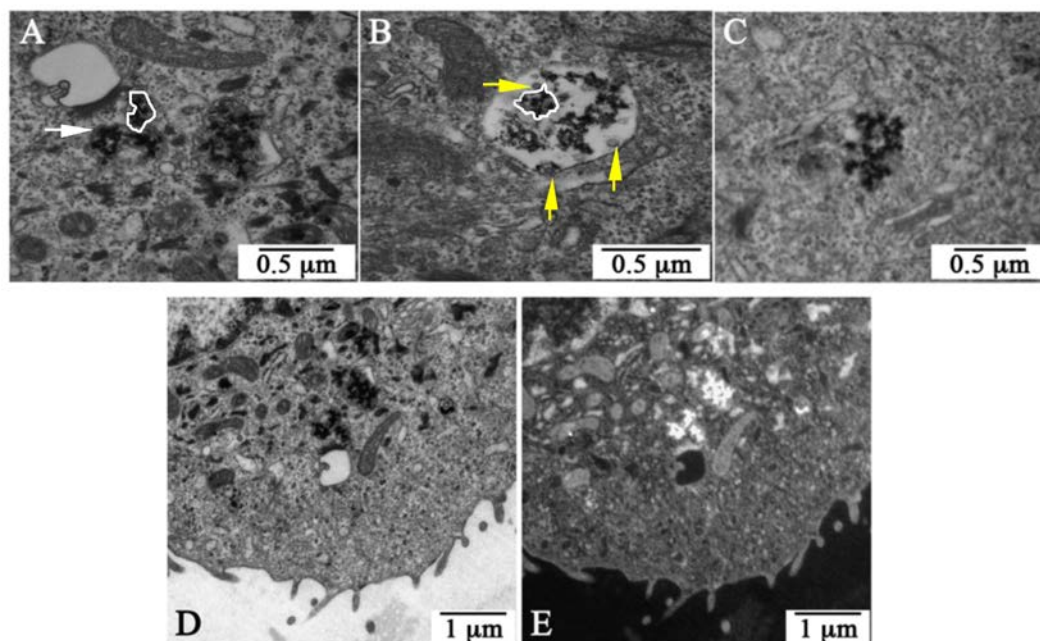


Figure 25: TEM image of A) particles gathered in vacuoles (white outline) separated from the rest of the cytoplasm by a double barrier (white arrow), B) vacuoles of particles (white outline) gathered in a multivesicular body that could contain degradation enzymes (yellow arrows) and C) agglomerated particles within the cytoplasm but outside the vesicles. Bright field (D) and its corresponding EFTEM image (E) acquired at the N_{45} edge of Gd (150 eV).

Very frequently the agglomerates are trapped in vacuoles clearly delineated by a membrane. This latter, that separates the agglomerates from the cytoplasm by a double barrier (see white arrow in Figure 25-A), has been underlined for clarity in certain zones of the Figures 25-A and 25-B (white outline). Two types of vacuoles containing agglomerates can be observed: vesicles (V) with a size comprised between 100 and 600 nm and, in a less proportion, multivesicular bodies (MVB) ranging between 500 and 900 nm. The Vs that contain agglomerates consist in early (or sorting) endosomes. The MVBs are always surrounded by a limiting membrane and consist in organelles that result from the gathering of several Vs, sometimes of different types. Since MVBs are themselves endocytic intermediates, they can internalize *via* endocytic pathways smaller vesicles (40 – 90 nm) such as the vesicles visible in Figure 25-B (see yellow arrow).

A small proportion of the agglomerates do not possess the above-mentioned double barrier that separates them from the cytoplasm (Figure 25-C). Since the few single particles that enter in the cell by passive diffusion cannot agglomerate within the cell (Supporting Information), the absence of the membrane should probably result from a vesicle bursting (a phenomenon very commonly observed in the cellular cytoplasm).

Also, a care examination of the agglomerates shows that these latter do not consist directly in the agglomeration of sub-5 nm GBNs but rather of entities (the aggregates) with a size comprised between 15 and 40 nm. Since these latter appear almost completely dense in the electron images, they should result from the aggregation of the GBNs. Moreover, whereas the agglomerates lie isolated in the large MVBs (each MVB containing between 1 and 10 agglomerates), the membranes of the vesicle almost exactly conform to the shape of the agglomerate. Under these conditions, the filling ratio of the particles within the vesicles can be estimated: after observation of more than 50 vesicles corresponding to different incubation conditions and taking into account different assumptions (such as the GBNs form a compact stacking within the aggregates), the filling ratio, f_r , does not depend significantly on the incubation conditions such as the concentration or the time and is equal to $f_r = 0.15$.

3.2.3.3.2 Effect of Concentration

With the objective to understand the mechanisms of particle internalization, the two main parameters controlling the incubation conditions, particle concentration and incubation time were successively changed. To study the effect concentration, we chose an incubation time of 1 h and a range of concentration comprised between 0.1 and 2 mM in order to retrieve the conditions for which the radiosensitizing effect of particles is maximal (clonogenic assays showed that the best radiosensitizing effect corresponds to an incubation for 1 h at a concentration of 0.6 mM). In a first step, the whole cells were characterized by Scanning Electron Microscopy. This technique that permits to observe the morphology of the cells shows that the quantity of particles attached on cell surface increases with the concentration (**Figure 26**). Indeed, whereas the cell surface is almost exempt of GBNs for an incubation concentration of 0.1 mM, large portions of the cell surface are completely coated by several shells of agglomerates for a concentration of 0.6 mM. The cells were carefully rinsed several times before observation; the images indicate then that at the vicinity of cells, particles tend to strongly agglomerate and adhere to their surface. Since it has been shown that, in absence of cells, the GBNs remain colloidally stable in different media (water, HBSS, DMEM) for a very large range of incubation concentration, the agglomeration observed here must be undoubtedly attributed to the presence of cells. This suggests that the particle internalization should take place in two steps, an agglomeration of particles followed by an agglomerate uptake.

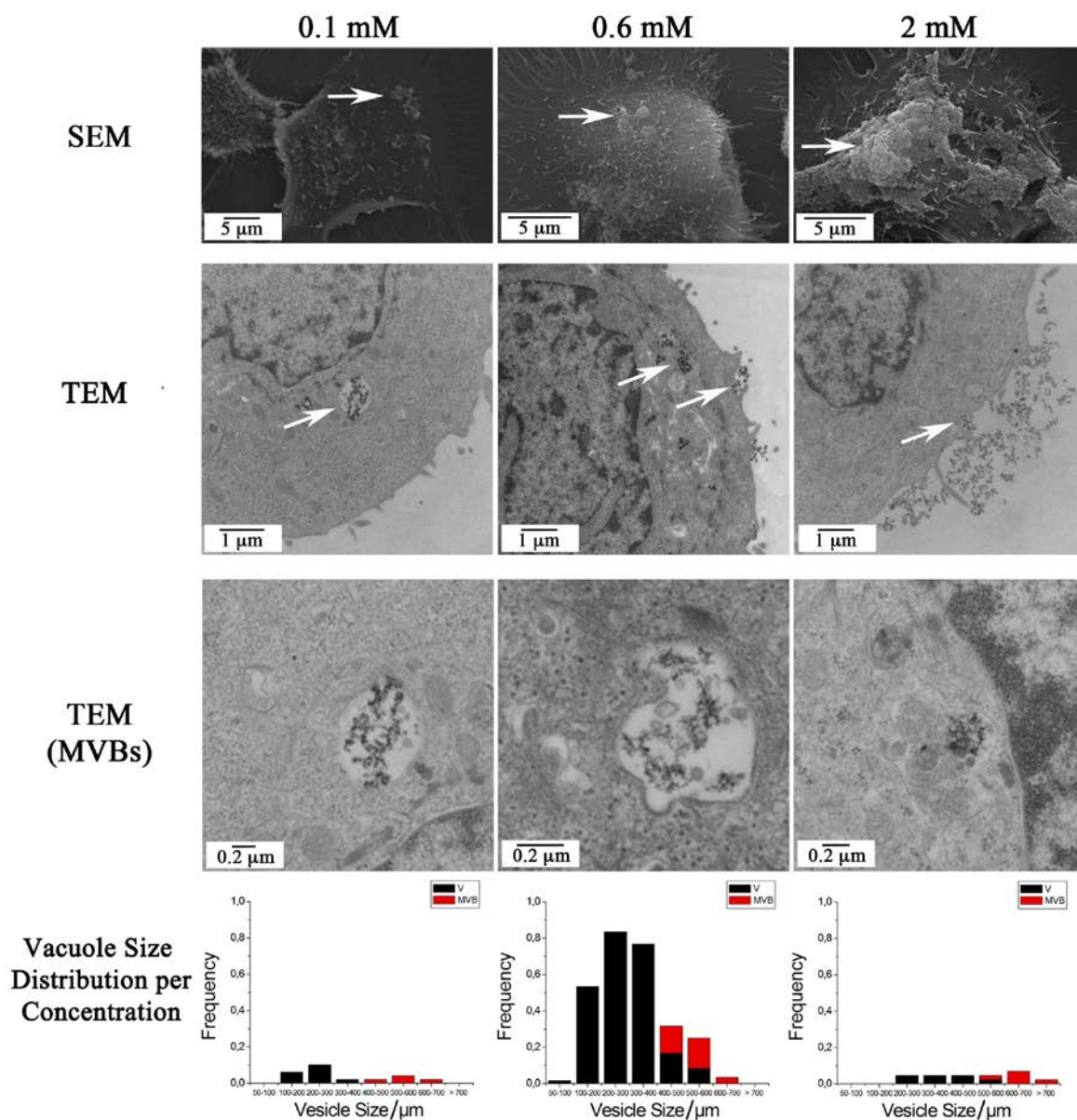


Figure 26: Visualization of particles adhering on cell membrane by SEM and TEM for incubation concentration of 0.1, 0.6 and 2 mM GBN. White arrows indicate the NPs aggregates. High magnification TEM images for vesicles (V in black) and multivesicular bodies (MVB in red) size distributions (from up to down).

To further characterize the agglomerates that have been internalized within the cell, TEM clichés were taken to visualize different cell sections for the same three concentrations already used. The presence of external agglomerates at close vicinity of the cells and the increase of their number with concentration permitted to confirm the information already given by the SEM technique. However, the agglomerates are not strongly bounded to the surface but are found to lie at a certain distance of the cell (inferior to a few micrometers). This suggests that

the forces responsible for the presence of agglomerates near cells are not of a chemical nature but originates from physical interactions (probably electrostatic).

To establish the size distribution of the vacuoles sections (vacuoles being either V or MVB), these latter were counted on a large number of thin cell sections (70 nm) comprised between 50 and 70. The size distributions presented in Figure 26 were normalized by the number of cells investigated. To avoid counting two times the same vacuole, the cells slices cut by ultramicrotomy were observed only in twenty (the distance between two slices studied being then superior to the size of a vacuole). For an incubation time of only 1h, the MVBs generally contain only one agglomerate even for high concentration (as in Figure 26; TEM MVBs, 2 mM). The presence of several agglomerates in the MVBs constitutes a very unusual situation that can be observed for all concentrations including the lowest (as in Figure 26; TEM MVBs, 0.1 and 0.6 mM). Therefore, in the case of an incubation time of 1 h, the size distribution of the vacuoles coincides almost exactly to that of the agglomerates.

For concentration varying from 0.1 to 0.6 mM, the number of vacuoles per cell increases before decreasing for the concentration of 2 mM (see graphics in Figure 26). Surprisingly, the number of agglomerates per cell (i.e. per vacuole) does not still increase with concentration but reaches a plateau for concentrations around 0.6 mM. Moreover, the average size of both vesicles and MVBs sections are found to increase with concentration. Taking into account that the average size of the vacuoles sections, $\overline{D}_{vac.section}$, is lower than that of the vacuoles, $\overline{D}_{vac.}$ (the exact relation between these two entities being: $\overline{D}_{vac.} = \frac{4}{\pi} \overline{D}_{vac.section}$ (see Supporting Information)), one can conclude that the average size of the vacuoles (V+MVBs) quantitatively increases from 0.1 mM (271 nm), up to 0.6 mM (406 nm) and 2 mM (612 nm). The increase of the vesicle size with concentration indicates that the agglomerates formed at vicinity of the cell are larger for high concentration, which is consistent with the general laws of the agglomeration processes. Concerning MVBs, the same increase can be simply explained by the fact that greater agglomerates-containing vesicles fuse with other types of vesicles to form larger MVBs.

All these results are very important, relatively to the objective of the paper that consists in understanding why the maximum of therapy efficiency is observed for an incubation concentration of 0.6 mM. Indeed, this concentration of 0.6 mM seems to simply correspond to the more efficient internalization of GBNs as agglomerates in the cell cytoplasm.

3.2.3.3.3 Effect of Incubation Time

Studying the kinetics of internalization into the cells should permit to precise the mechanisms of particles entry. First, kinetics has been macroscopically evaluated by means of ICP using cells that have been incubated for different times (30 min, 1 h and 2 h) and carefully rinsed before analysis. Since 0.6 mM is the most effective dose for radiosensitizing (Figure 23-A), this concentration has been chosen for all the experiments. According to **Figure 27-A**, internalization seems to follow approximately the classical Fick's law of diffusion characterized by a high rate at the beginning of the process followed by a strong deceleration. Here, the deceleration occurs after 1h, the increase in the quantity of particles internalized or attached on cells surface between 1 and 2 h being smaller than 15 %. More precisely, Figures 27-B, 27-C and 27-D show that the vesicles seems lying in a stationary state since their size distribution does not undergo significant modifications with time: for instance the average vesicles size are equal to 359 nm at 1 h and 350 nm at 2 h. This means that the quantity of agglomerates internalized into vesicles is almost exactly compensated by that of vesicles fusing into MVBs. In the same time one can remark both an increase in the quantity of particles internalized in MVBs and in the average size of MVBs, this latter varying from 682 to 801nm between 1 and 2 h of incubation. This last result is consistent with the fact that the new vesicles formed by agglomerate entry can themselves fuse to the MVBs already present in the cytoplasm. Under these conditions (2 h of incubation), the MVBs can contain more than one agglomerate, which is effectively observed by electron transmission. Indeed, contrary to low time incubation (<1 h) for which each MVB generally encapsulate only one agglomerate, more than 1/3 of the MVBs contain 2 or more agglomerates for an incubation of 2 h (data not shown).

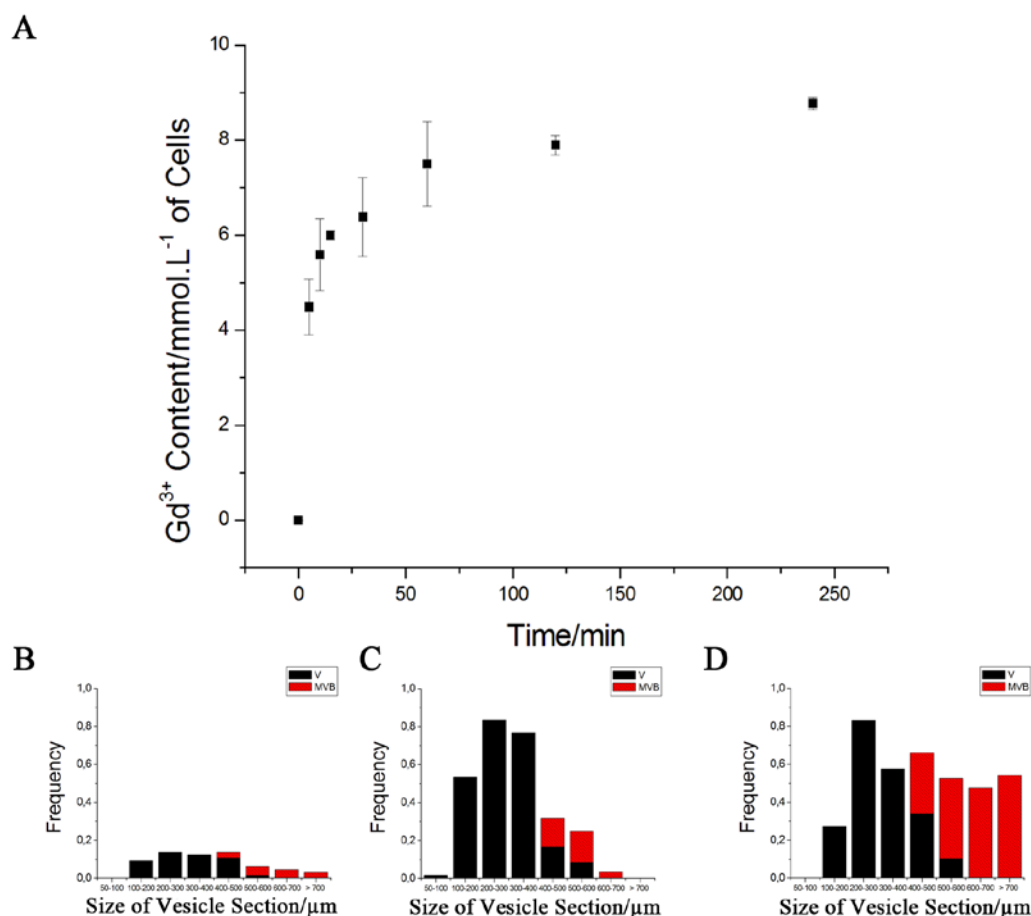


Figure 27: Kinetics of particle entry for an incubation concentration of 0.6mM (Gd). A) Chemical analysis of Gd content by ICP after prolonged cell washing for different incubation times varying from 5 to 240 min. TEM size distribution of vesicles (black) and multivesicular bodies (red) in cells for different incubation times: B) 30 min, C) 60 min and D) 120 min.

All these results show that the kinetics of particle internalization process is very similar to that followed by molecules or proteins^[cxlix], which indicates that the entry of agglomerates of a few hundreds of nanometers is quite similar to that of the smaller species usually involved in the cell metabolism. Generally, the cells used the trafficking from early endosomes (the vesicles) to late endosomes (MVBs) and lysosomes to degrade different types of molecular species. During the endocytic pathways (of species to vesicles), the species are rapidly (< 2 min) exposed to a drop in pH from neutral to pH 5.9-6.0 in the lumen of early recycling vesicles, with further decrease from pH 6.0 to 5.0 during progression from late endosomes to lysosomes.^{[cl][cli]} It seems then that the particles are taken in charge by the cell to provoke their destruction under acidic conditions before their eventual rejection out of the cell (not observed here for the duration of incubation used).

3.2.3.4 Macropinocytosis as the First Entry Mechanism of GBNs at a Moderate Dose

3.2.3.4.1 First Indication of a Macropinocytosis Process

After having specified the internalization process as a function of the incubation conditions (concentration and time), we now focus on the early stage of particles entry that seems characteristic of a macropinocytosis process. Indeed, according to the micrographs of **Figure 28** that details the particles motion through the membrane, it can be seen that, in presence of GBNs agglomerates at vicinity of cell surface, there is some extension of the plasma membrane towards the extracellular medium. Precisely, the membrane tends an « arm » (lamellipodium) to pick up the particles agglomerates before curving the arm and locking the agglomerate in the so formed vesicle that has a size comprised between 100 nm and 600 nm.

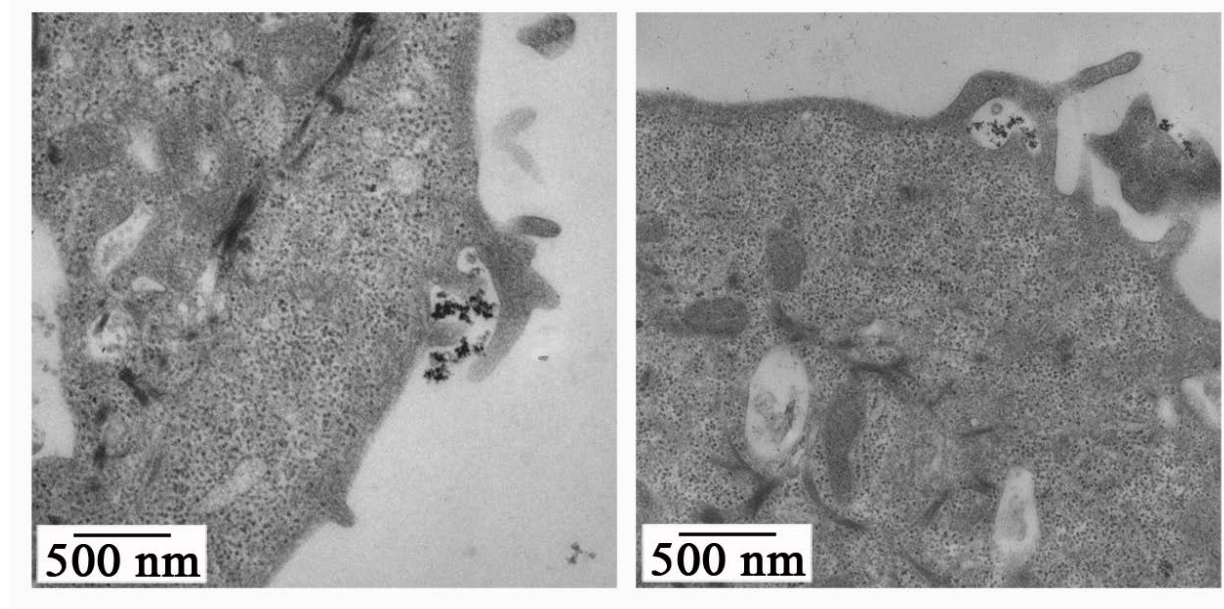


Figure 28: TEM images showing macropinosome formation. Left: rising and bending of a single lamellipodia inducing circular (or curved) ruffle containing nanoparticles. Right: ruffle after lamellipodia collapse giving rise to a protrusion (early macropinosome) that will fuse with the plasma membrane and penetrate into the cytoplasm.

Macropinocytosis is the only entry process that possesses these characteristics especially considering the deformation undergone by the membrane and the size of the entity internalized. Indeed, it is characterized by some membrane ruffling induced on cell surface and/or formation of membrane protrusions. These protrusions do not zipper up along the particle but collapse onto and fuse with the membrane to generate large endocytic vesicles, called macropinosomes (200 nm to 2 μ m in diameter).^[xxvii] These characteristics that can be retrieved in Figure 28 are absent in the other mechanisms of internalization. For instance, in

the clathrin-mediated endocytosis, the coated vesicle has a size of approximately 120 nm and is formed after membrane invagination (not seen here), scission and release into the cell. Similarly, caveolin-mediated endocytosis first processes by flask-shaped 50-60 nm invaginations at cell surface that further pinch off to form vesicles. Also clathrin and caveolin-independent cholesterol microdomains (also called rafts) have a size of 40-50 nm that can diffuse freely on the cell membrane. Since the size of the vesicles observed here is generally comprised between 150 and 600 nm (Figures 26 and 27) and that no invagination containing GBNs was observed on SQ20B cells membrane, the different types of endocytosis can not be responsible for internalization of particles agglomerates. Also the phagocytosis, a highly regulated process involving specific cell-surface receptors, can be eliminated since these receptors are only present on the membrane of specialized cells such as macrophages and monocytes. The phagocytosis is recognized by the formation of cell-membrane extensions that zipper up around the particle to engulf it.^[cliii] Macropinocytosis seems then to be the major possible pathway for agglomerate internalization into SQ20B cells.

3.2.3.4.2 General Description of the Complete Entry Mechanism Involving Two Successive Steps: GBNs Agglomeration at Vicinity of the Cell and Internalization via Lamellipodia (Macropinocytosis)

To check if the formation of agglomerates is really favored by the presence of cells, FCS measurements were performed in order to estimate the size of the particles as a function of their distance from the cell. Measures were made directly after dilution of the GBNs in the medium (HBSS or water) as well as 90 min later, as a function of particles concentration. By moving the laser excitation perpendicularly to the surface supporting the cell, it was possible to obtain FCS signal at a distance of 5 μm from the cell until some hundreds of μm using a step of 10 μm . As indicated in **Figure 29**, the particles gather effectively in agglomerates in the solution at a distance from the cell that depends on the concentration and whose order of magnitude is of some tenths of micrometers (Supplementary Information).

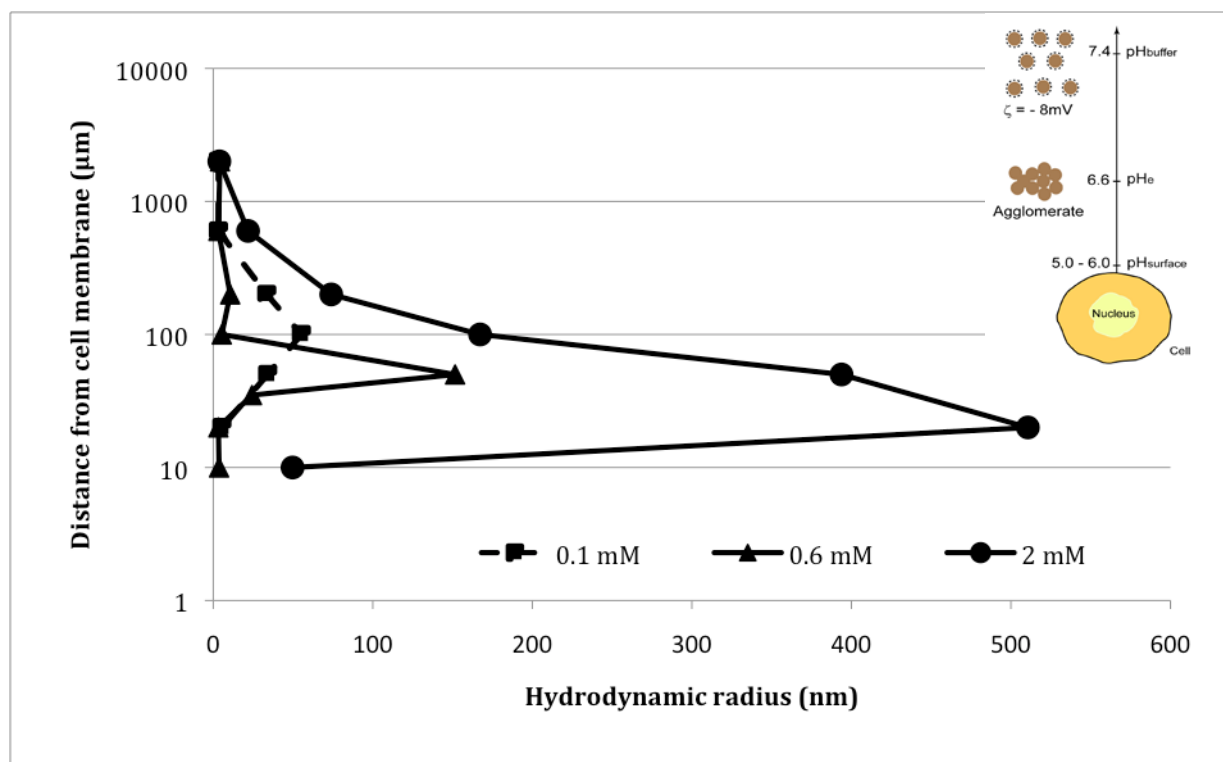


Figure 29: Particle agglomeration as a function of the distance to cell. Fluorescence correlation spectroscopy measurements of the hydrodynamic radius as a function of the distance to cell membrane for different particle concentrations (0.1, 0.6 and 2 mM) in HBSS media.

Since no agglomeration is observed in absence of cells regardless of the medium and the particles concentration, this latter is necessarily related to the presence of cells. Indeed, it is well known that cells modify at their vicinity some parameters of the solution such as the ionic force, the osmolarity or the pH. In our opinion, it is this latter parameter, in conjunction with the fact that the isoelectric point of the particles is equal to $pH_e \approx 6.6$ that influences the possibility of agglomeration. As already mentioned, cells are negatively charged with, at vicinity of the membrane, a pH inferior to that found in normal tissues, typically $pH_{surf.} \approx 5-6$. Now when the distance from the cell increases, pH should vary simultaneously from the value near the cell, $pH_{surface} \approx 5-6$, to that of the buffer, $pH_{buffer} \approx 7.4$ (see inset in Figure 29). Since the particles are negatively charged at pH 7.4 ($\zeta = -8 \text{ mV}$) and are characterized by an isoelectric point at $pH_e \approx 6.6$, this latter pH is attained at a certain distance from the cell. At this distance the electrostatic stabilization of the solution completely vanishes so that the particles could lose their colloidal character. This loss of electric repulsion is probably accentuated by the different species such as metal cations that are permanently rejected by the cell and can participate to a strong screening of the repulsion forces. In conclusion, the condition necessary to obtain some particles agglomeration should be that the isoelectric point of the particles

(pH_e) is simply comprised between the pH at close vicinity of the cell ($pH_{surface}$) and that of the buffer (pH_{buffer}), condition that is effectively fulfilled here:

$$pH_{surface} < pH_e < pH_{buffer}$$

By examining precisely the results of Figure 29, the size of the agglomerates increases, as expected, with the particles concentration (150 nm for a Gd incubation concentration of 0.1 mM, 800 nm for 2 mM) while the distance to the cell at which some agglomeration occurs significantly decreases with concentration. For instance, particles agglomerate at 100 μ m for a concentration of 0.1 mM, 60 μ m for 0.6 mM and 20-30 μ m for 2 mM. At vicinity of the cell where more acidic conditions are encountered, the species that lie at the particles surface (such as DTPA or amine groups...) are subjected to a H^+ consumption that locally increases the pH. This leads to a pH increase near the cell that induces some particles agglomeration at a distance that is smaller when the particles concentration is high. This explanation (which is in complete qualitative agreement with the results of Figure 29) indicates the optimal incubation concentration range that favors the mechanism of macropinocytosis. Indeed, when the agglomerates are too large (which happens for too high incubation concentrations), they are more hardly entrapped by the lamellipodia that lie at an average distance of 500-800 nm one from each other. Similarly, when the agglomerates are too far from the cells (which happens for too small incubation concentrations), they cannot be efficiently recuperated by the lamellipodia. Therefore, the technique of FCS that permits a direct determination of both the location and the size of the agglomerates explains entirely the results of Figure 26 in which it appears that macropinocytosis is efficient only in a limited range located around an incubation concentration of 0.6 mM. In particular, these results might in part explain the reduction of internalization at 2 mM into SQ20B cells due to an excessive agglomeration.

All the results are confirmed by the SEM data of Figure 26. Indeed GBNs seem to agglomerate at vicinity of the cell before entering into cells *via* clearly visible lamellipodia.

3.2.3.4.3 Confirmation of Macropinocytosis by Confocal Microscopy Using Inhibitors

The two previous paragraphs have shown that: (i) some agglomerates are formed at vicinity of the cells that (ii) can cross the membrane with help of cells lamellipodia. Since the size of the agglomerates and the observed membrane strains are consistent with a macropinocytosis route, we used an inhibitor of this process to identify it definitely. Confocal microscopy observations were then performed on fixed cells incubated for 1 hour at 37°C and GBNs

concentration of 0.1, 0.6 and 2 mM in the medium alone or containing, amiloride, the macropinocytosis inhibitor chosen (Supporting Information). In absence of inhibitor, some of the agglomerates are clearly internalized (see the small red dots due to the Cy5.5 encapsulated in GBNs in **Figure 30** for the concentration of 0.6mM). On the contrary, in presence of amiloride, all the agglomerates stay at the cell surface, none of them penetrating in the cytoplasm regardless of the GBN concentration, 0.1, 0.6 or 2 mM. This is the definitive proof that the internalization pathway of the agglomerates consists effectively in macropinocytosis. Finally, this result was confirmed by two different kinds of experiments. (i) First, macropinocytosis is a temperature-dependent process that is also inhibited at low temperature. As expected, a similar inhibition of the agglomerates entry is also observed at 4°C even in absence of amiloride. (ii) Second, it was also proven that the inhibitors of the two more probable alternative pathways for agglomerates internalization (amantadine as the inhibitor of the clathrin-dependent endocytosis and nystatine as the inhibitor of the caveolae-dependent endocytosis inhibitor) are not able to inhibit the agglomerate entry into SQ20B cells (Supporting Information).

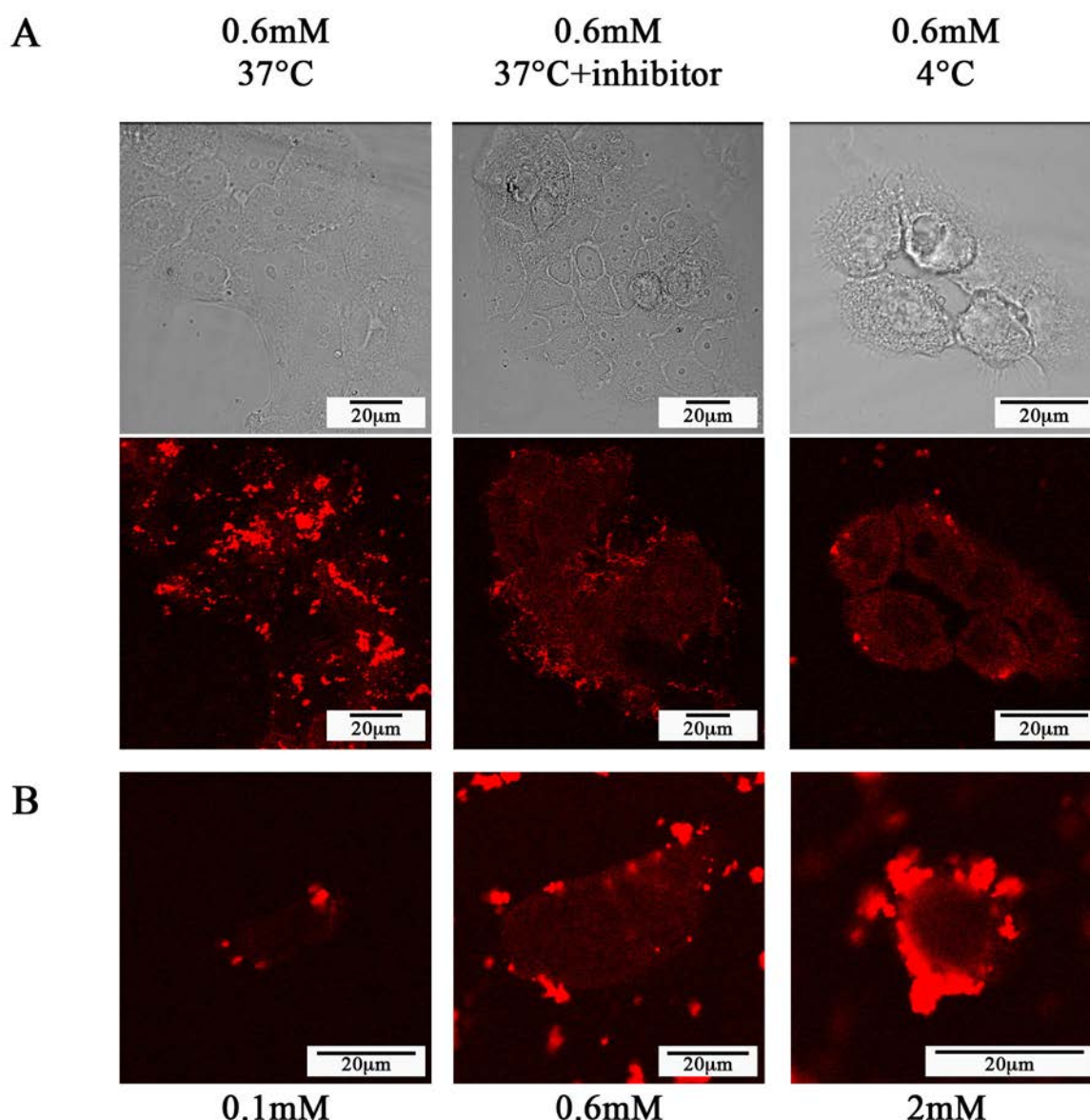


Figure 30 :Internalization of NPs through macropinocytosis and evidence of passive diffusion. A) Phase contrast and fluorescence (excitation power 4%) confocal images of SQ20B cells incubated with particles at a concentration of 0.6 mM during 1 hour (left) at 37°C, (middle) at 37°C in presence of amiloride (macropinocytosis inhibitor), and (right) at 4°C. B) Fluorescence (excitation power 60%) confocal images of SQ20B cells incubated with particles during 1 hour at 4°C for different concentrations: 0.1 mM, 0.6 mM and 2 mM (from left to right).

3.2.3.5 Passive Diffusion as a Second Mechanism for GBNs Entry

An attentive examination of the micrographs of Figure 30-A shows that in absence of macropinocytosis, some particles can nevertheless enter into the cell cytoplasm since this latter appears in a red and uniform color that contrasts with the less red coloration of the nucleus. Since the entry processes of endocytosis and phagocytosis have been already eliminated, this particles entry should be related to some passive diffusion of particles within

the cytoplasm. This internalization pathway that is purely mechanistic and for this reason temperature-independent is confirmed by the fact that for an incubation at 4°C, a temperature that slacken the biological activity of the membrane, the particle entry is quite similar to that observed for internalization at 37°C (see Figure 30-B which shows particles entry into the cytoplasm for incubation concentrations of 0.1, 0.6 and 2 mM at 4°C and so evidences that passive diffusion is more efficient for high incubation concentration).

In conclusion, two different pathways participate to particles entry during cell incubation in the presence of GBNs: macropinocytosis and passive diffusion.

3.2.3.6 Relative Quantification of the Different Internalization Mechanisms and Explanation of Radiotherapy Efficiency at Moderate Dose

From all the results obtained, it is now possible to discriminate, among the quantity of gadolinium attached to the cells (i.e. measured by ICP and expressed in mmol of Gd per liter of cell), the relative proportions of (i) the gadolinium entered by macropinocytosis, (ii) that entered by passive diffusion and (iii) that remaining at the surface. This will be done for the three incubations performed at different incubation concentrations, 0.1, 0.6 and 2 mM for an incubation time of 1 hour.

3.2.3.6.1 Determination of the Quantity of Particles Entered by Macropinocytosis

To determine the quantity of particles entered by macropinocytosis, we used the histograms of Figure 26 resulting from systematic observations of agglomerates by electron microscopy. They give the normalized size distribution of the vesicle sections for the incubation concentrations, 0.1, 0.6 and 2 mM. For each concentration, N cells have been studied and n vesicles have been counted. Agglomerate (or vacuoles under the justified assumption that each vacuole, V or MVB, contain only one agglomerate) distributions have been normalized by a division by the total number of vacuoles, n. The histograms give then also the density of probability, $p(D_{vac.section})$, to find a vacuole section of a given size, $D_{vac.section}$. From the average size of the vacuole sections, $\overline{D_{vac.section}}$, one can derive a satisfying approximation of the average size of the vacuoles, $\overline{D_{vac}}$ using the formula: $\overline{D_{vac}} = \frac{4}{\pi} \overline{D_{vac.section}}$. This relation is valid for spherical vacuoles and narrow size distributions (see Supporting Information) and, as already stated in the case of cells; it indicates that the diameter of a vacuole section is smaller

than the diameter of the vacuole. The average volume of the vacuoles can then be approximated by the relation, $\bar{V}_{vac.} = \frac{4\pi}{3} \left(\frac{\bar{D}_{vac.}}{2} \right)^3$, that is again valid for narrow size

distributions. If one denote z the thickness of the sections observed ($z \approx 70$ nm), the total volume of the cells investigated is then $V_{cell}^{total} = N\pi\bar{D}_{cell\ section}^2 z$ while that of the vesicles is equal to: $V_{ves}^{total} = n\pi\bar{D}_{vac.\ section}^2 z$. In the last formulas, $\bar{D}_{cell\ section}^2 = P_1\bar{D}_{1\ cell\ section}^2 + P_2\bar{D}_{2\ cell\ section}^2$

where $\bar{D}_{1\ cell\ section}$ and $\bar{D}_{2\ cell\ section}$ are the average values relative to the two populations of the cells and P_1 and P_2 their relative proportions. The volume of vacuoles per cell is then equal

to: $V_{vac./cell} = \frac{n}{N} \left(\frac{\bar{D}_{cell\ section}}{\bar{D}_{vac.\ section}} \right)^2 \bar{V}_{cell} = \frac{n}{N} \left(\frac{\bar{D}_{cell}}{\bar{D}_{vac.}} \right)^2 \bar{V}_{cell}$ and the number of vacuoles per cell

$n_{vac./cell} = \frac{(V_{vac./cell})}{V_{vac.}}$. Remembering finally that the filling coefficient of the vacuoles by the

particles is equal to $f_r = 0.15$ (when neglecting the low proportion of MVBs in front of that of Vs) and that the Gd concentration is equal to: $c_{Gd/particle} = 2.8 \cdot 10^{-12}$ mmol of Gd per μm^3 of particles, the concentration of Gd per liter of cell brought by macropinocytosis is equal to:

$c_{Gd}^{macropin.} = n_{vac./cell} f_r c_{Gd/particle} \frac{1}{V_{cell}}$. All these data, completed by the quantity and concentration

of Gd per vacuole ($c_{Gd/vac.}^{macropin.}$ and $c_{Gd/vac.}^{macropin.}$) are given in **Table 3** for the concentrations 0.1, 0.6

and 2 mM taking into account that: $\bar{V}_{cell} = 1583 \mu m^3$.

Table 3: Data concerning the agglomerates entered by macropinocytosis for incubation concentrations of 0.1, 0.6 and 2mM.

Incubation concentration (mM)	0.1	0.6	2
$\frac{n}{N}$	0.225	2.75	0.279
$\overline{D}_{vac. section}$ (nm)	213	319	580
$\overline{D}_{vac.}$ (nm)	271	406	738
$\overline{V}_{vac.} = \overline{V}_{agglomerate}$ (μm^3)	0.01	0.03	0.21
$V_{vac./cell}$ (μm^3)	0.129	35.3	1.18
$n_{vac./cell}$	13	1176	6
$q_{Gd/vac.}^{macropin.}$ (mmol)	$2.8 \cdot 10^{-15}$	$8.4 \cdot 10^{-15}$	$5.6 \cdot 10^{-14}$
$c_{Gd/vac.}^{macropin.}$ (mM)	282	280	280
$c_{Gd}^{macropin.}$ (mM)	0.023	6.24	0.22

3.2.3.6.2 Determination of the Quantity of Particles Entered by Passive Diffusion

To determine now the concentration of particles entered by passive diffusion, results obtained in confocal microscopy were used. Precisely, the particle concentration related to passive diffusion has been determined from the comparison of the optical signals of, on one hand, the vacuoles filled by macropinocytosis and, on the other hand, those of the cytoplasm filled by passive diffusion during incubations at 4°C (Supporting Information). We took into account that the agglomerates entered by macropinocytosis were visualized using an excitation power of 4% whereas the isolated particles internalized by passive diffusion were visualized using a higher power of 60%. Denoting $I_{agglomerate}^{macropin.}$ the pixel intensity of the agglomerates entered by macropinocytosis and $I_{particle}^{passive diff.}$ that of the particles entered by passive diffusion, we find that

the ratio $\alpha = \frac{I_{agglomerate}^{macropin.}}{I_{particle}^{passive diff.}}$ obeys the formula:

$$\alpha = \frac{I_{agglomerate}^{macropin.}}{I_{particle}^{passive diff.}} = \frac{C_{Gd/vac.}^{macropin.}}{C_{Gd/cytoplasm}^{passive diff.}}$$

in which $c_{Gd/vac.}^{macropin.}$ and $c_{Gd/cytoplasm}^{passive\ diff.}$ are respectively the concentration of Gd in the vacuoles entered by macropinocytosis (mmol of Gd per L of vacuole) and that of Gd in the cytoplasm internalized via passive diffusion (mmol of Gd per L of cytoplasm). Again, all the steps needed for calculating the particles concentration related to the passive diffusion pathway ($C_{passive\ diffusion}$) are given in **Table 4**. In this table, we give in particular the ratio α as well as the concentration of Gd entered by passive diffusion, $c_{Gd}^{passive\ diff.}$, that we derive according to

$$\text{the relation: } c_{Gd}^{passive\ diff.} = c_{Gd/cytoplasm}^{passive\ diff.} \cdot \frac{\bar{V}_{cytoplasm}}{\bar{V}_{cell}} \cdot \bar{V}_{cell} = 1583\mu m^3, \bar{V}_{cytoplasm} = 1005\mu m^3.$$

Table 4: Data concerning the particles entered by passive diffusion for incubation concentrations of 0.1, 0.6 and 2 mM.

Incubation concentration (mM)	0.1	0.6	2
α	1500	300	250
$c_{Gd/vac.}^{macropin.}$ (mM)	282	280	280
$c_{Gd/cytoplasm}^{passive\ diff.}$ (mM)	0.19	0.93	1.1
$c_{Gd}^{passive\ diff.}$ (mM)	0.11	0.6	0.71

3.2.3.6.3 Recapitulation of the Quantities of Gd Internalized by the Different Entry Pathways (Macropinocytosis and Passive Diffusion) and Adherent on Cell Surface

All the results found until now permit to give the repartition of the gadolinium entered by macropinocytosis or passive diffusion as well as the gadolinium adhering at the cell surface. These data are given in **Table 5**.

Table 5: Concentrations of Gd internalized by the different entry pathways (macropinocytosis and passive diffusion) and attached on cell surface.

Incubation concentration/Time of incubation	0.1 mM / 1 hour	0.6 mM / 1 hour	2 mM / 1 hour
Gd measured by ICP, C_{Gd}^{ICP} (mM)	0.13	9.8	36.2
Gd entered by macropinocytosis, $C_{Gd}^{macropin.}$ (mM)	0.023	6.2	0.22
Gd entered by passive diffusion, $C_{Gd}^{passive\ diff.}$ (mM)	0.11	0.6	0.71
Gd adhering at surface, $C_{Gd}^{cell\ surface}$ (mM)	≈ 0	3.0	35.2

The evolution of the quantity of Gd adhering at cell surface (obtained by difference according to the formula: $C_{Gd}^{cell\ surface} = C_{Gd}^{ICP} - C_{Gd}^{macropin.} - C_{Gd}^{passive\ diff.}$) is in very good agreement with the SEM micrographs of Figure 26 that shows that this latter significantly increases with the incubation concentration. On the contrary, the complete absence of correlation between on one hand the surface Gd quantity (Table 5) and the radiotherapy efficiency (Figure 23-A) indicate that the gadolinium at cell surface has strictly no effect upon radiotherapy. As already mentioned, this can be easily explained by the fact that the killing species generated during X-ray irradiation (Auger electrons and ROS) have a mean free path (≈ 200 nm) too small to reach the cell nucleus DNA.

Concerning the macropinocytosis pathway, we have already discussed the fact that this entry route is strongly favored for incubation concentrations around 0.6 mM. Indeed, only for this concentration range, the cell lamellipodia are able to recuperate the particles agglomerates formed in the solution at a few micrometers of the cell. However, a care comparison of the radiotherapy efficiency (Figure 23-A) and data of Table 5 shows that, even if the concentration of Gd entered by macropinocytosis is, for an incubation concentration of 0.6 mM, ten times higher than that internalized *via* passive diffusion (6.24 against 0.6 mM), the related increase in the radiotherapy efficiency is only of 100 %. In other words, the radiosensitizing effect of isolated Gd particles is 10 times higher than that of Gd

agglomerates. This validates the fact that, in agglomerates of a few hundreds of nanometers, the killing species encounter large difficulties to escape from the agglomerates and reach the cell nucleus.

Finally, concerning passive diffusion, very striking is that, for the incubation concentrations of 0.1 and 0.6 mM, the particles concentration inside and outside the cell are almost exactly the same (external concentration: the incubation concentration; internal concentration: $c_{Gd}^{passive\ diff}$). This result indicates that some equilibrium is reached relatively to the transport phenomena through the cell membrane. For identical concentrations inside and outside the cell indeed, the Gd flow, which is, according to the Fick's law, proportional to the concentration gradient of Gd completely vanishes. On the contrary, this observation is false for higher incubation concentration (2 mM). This is a very comprehensible result since for high concentrations; these latter must be replaced in the Fick law by the activities that depend also on the nature of the medium. For high concentrations, the process is also certainly limited by the particles transport within the solution so delaying equilibrium establishment. This last explanation is reinforced by the fact that, for all the experiments performed; the ratio between the quantity of cells and that of particles has been maintained constant (1 million of cells against 1.8 μ mol of particles).

In conclusion, particles internalization is preponderant for the concentration of 0.6 mM, which lies in the limited range in which macropinocytosis can act in significant proportion. The more probable explanation for radiosensitization is then that, even if agglomerates are 10 times less efficient than particles, radiosensitization is optimal when a maximum of particles enter within the cells and thus reside at proximity of the nucleus. Indeed, whatever the killing species involved in *in vitro* effect of radiotherapy (Auger electrons or ROS), these ones require being at a small distance (typically some hundreds of nanometers) from the nucleus to efficiently degrade its content. The question will be now to correlate those observations to the results obtained *in vivo* in the case of rats bearing glioblastoma. In this paper the amount of Gd entered *in vitro* is of about 1000 ppm (0.1 %) by macropinocytosis and 100 ppm by passive diffusion for the optimal incubation concentration (0.6 mM). *In vivo*, it has been shown that the Gd concentration within the tumor able to induce a significant radiosensitizing effect was in the order of magnitude of 10-100 ppm. This indicates that, *in vivo*, the gadolinium-based entities internalized within the tumors should be under a particulate form since, at the concentration of 10-100 ppm, agglomerates are found here to be unable to cause a significant radiosensitizing effect. Such a conclusion is reinforced by the fact that, during

GBNSs intravenous injection, the particles circulating in the blood stream without agglomeration should be recuperated one after one by the brain tumor.

3.2.4 Conclusions

It has been shown that the sub-5 nm gadolinium-based nanoparticles (GBNs) developed by our group possess an *in vitro* efficient radiosensitizing effect even at moderate concentration when incubated with SQ20B. To further understand this phenomenon and optimize it, we used different types of microscopy techniques, in particular electron microscopy that possesses a 10 nm resolution sufficient to determine the mechanisms responsible for particles uptake. Two main cellular internalization mechanisms were then evidenced and quantified: passive diffusion and macropinocytosis. Whereas the amount of particles internalized by passive diffusion is hardly sufficient to induce *in vitro* radiosensitization, the cellular uptake by macropinocytosis, significant only in a limited range of GBNS incubation concentration, permits to obtain a clear radiosensitizing effect of the particles. This is true even if macropinocytosis only allows the internalization of agglomerates, which are less efficient radiosensitizing agents than particles since the killing species (Auger electrons and reactive oxygen species) encounter great difficulties to escape from such constructs and then reach the nucleus DNA. Precisely, macropinocytosis processes in two steps: formation of agglomerates at vicinity of the cell followed by their recuperation by the cell lamellipodia (i.e. the cell “arms”). The first step is strongly dependent on the physicochemical characteristics of the particles, especially their isoelectric pH. Indeed it is this value that determines the size of the agglomerates and their distance from the cell, which are the two relevant parameters that render possible their collect *via* the lamellipodia. All these results pose interesting challenges for clinical use of GBNS. They should permit to control the quantity of particles internalized in the cell cytoplasm so promising opportunities towards a particle-assisted radiotherapy using lower doses of radiation.

3.2.5 Experimental Section

3.2.5.1 Nanoparticle Characterization

3.2.5.1.1 Size Measurement and Structural Characterization

Direct measurement of the size distribution of the Nanoparticles was performed with the size analyzer NanoS PCS from Malvern Instruments. Measurements were directly taken on the colloid after surface modification of the nanoparticles. Confirmation of sizes was obtained from high-resolution transmission electron microscopy (HRTEM) performed at CLYM (Centre Lyonnais de Microscopie) with a JEOL 2010F microscope equipped with a Gatan Digi-PEELS energy filter in order to analyze the Si-L₂₃ and Gd-N₄₅ ionization edges with electron energy-loss spectroscopy (EELS). Drops of colloidal solutions were deposited on dedicated TEM carbon grids and observed after natural drying.

3.2.5.1.2 Fluorescence Correlation Spectroscopy (FCS)

Fluorescence correlation spectroscopy and laser scanning microscopy (LSM) were carried out on a commercial system consisting of a LSM510 and a ConfoCor2 (Zeiss, Jena, Germany). The 633 nm line of a He-Ne laser was directed *via* a 633 dichroic mirror onto the back aperture of a Zeiss C-Apochromat 40×, N.A. = 1.2, water immersion objective. The measurements were carried out at room temperature in 8-well Lab-Tek I chambered cover glass (Nalge Nunc International, Illkirch, France). The 633 nm He-Ne laser beam was focused into 50 μL solutions at 150 μm over the cover glass.

The fluorescence emission was collected through a 90-μm pinhole. To remove any residual laser light, a 650 nm-long pass emission filter was employed. Photon counts were detected by an Avalanche PhotoDiode at 20 MHz for 30 seconds. For each sample, FCS measurements were repeated 10 times. The fluorescence signals were software-correlated and evaluated with the Zeiss FCS Fit software (Zeiss, Jena, Germany). Most of the intensity autocorrelation curves were fitted using a free diffusion model with two components: the NP coupled to the fluorochrome alone (mono-NP) and the fluorescent aggregates (the average of the aggregates). Structural parameter and triplet fraction were fixed. Moreover, a calibration step with 1-4 nmol/L (dye) made it possible to evaluate the size of the confocal volume ($\approx 1 \mu\text{m}^3$).

3.2.5.1.3 Zeta Potential

Direct determination of the zeta potential of the nanoparticles was performed with the Zetasizer 3000HSa (laser He-Ne (633 nm)) from Malvern Instruments. Prior to the experiment, the solution was diluted in an aqueous solution containing 0.01 M NaCl and adjusted to the desired pH.

3.2.5.1.4 Relaxivity

Relaxivities were determined with MQ60 NMR analyzer (Bruker Instruments, Marne la Vallée, France) at 60 MHz after heating 5 min at 37°C.

3.2.5.1.5 Absorbance

Absorbance was determined on 50 Scan UV-visible spectrophotometer (Varian, Toulouse, France).

3.2.5.2 Cell Lines and Culture Conditions

The SQ20B cell line was established from a patient with recurrence of a squamous cell carcinoma of the larynx after radiation. The cells were grown in Dulbecco's Modified Eagle Medium (DMEM) enriched with 4.5 g/L glucose and supplemented with 1% L-glutamine, 10% fetal bovine calf serum, 100 units/ml penicillin, 100 µg/ml streptomycin, 0.1% fungizone and 0.4mg/mL hydrocortisone. U87MG (Human radioresistant gliosarcoma) cells were grown in DMEM supplemented with 10 % fetal bovine serum. LTH (Jurkat, immortalized Human T lymphocytes) were grown in RPMI supplemented with 10% fetal bovine serum. All the cell lines were cultured at 37 °C in a humidified 95% air / 5% CO₂ atmosphere.

3.2.5.3 Particles Internalization in SQ20B Cells

Exponentially growing cells (10×10^6 cells / sample) were incubated for 30 minutes, 1 hour and 2 hours in presence of particles (4Si-DTPA) at varying concentrations: 0.1 mM, 0.6 mM and 2 mM of Gd in HBSS medium. For the blocking internalization studies, the conditions are similar as those in the confocal microscopy section.

3.2.5.4 Determination of Uptake by Inductively Coupled Plasma (ICP)

The gadolinium concentration of labeled cells was measured using Inductively Coupled Plasma Optical Emission Spectroscopy. For this, 1:200 μL of 65% (vol/vol) nitric acid was added during 2 hours to a known number of pelleted cells (comprised between 3 and $4 \cdot 10^5$). The solution obtained was diluted in 5 % (vol/vol) nitric acid to reach a gadolinium concentration in the measurable range [1-100 ppb]. The exact gadolinium concentration ($\mu\text{g/mL}$) was then measured at 336.22 nm in a sample with a volume comprised between 3 and 4 mL using a Varian 710-ES ICP-OES apparatus (Varian, Les Ullis, France).

3.2.5.5 Clonogenic Survival Assay at 2 Gy

Cell survival assay was assessed by a standard colony formation assay ^[cliii] with minor modifications. One million of cells were incubated for 1 hour with GBNSs at different concentrations (0.4 to 2mM) and after two washes with PBS, irradiated in fresh medium at 2Gy. Immediately after exposure, cells were trypsinized and re-seeded at different concentrations into 25 cm^2 flasks to yield 10-120 colonies after six cellular divisions. Colonies containing more than 64 cells were scored and the percentage of surviving cells was calculated. The surviving fraction after each treatment was normalized to the surviving fraction for the corresponding control (plating efficiency).

3.2.5.6 Transmission Electron Microscopy

Samples of fresh cells were fixed for at least 1 hour at room temperature with 2% glutaraldehyde in 0.1 M sodium cacodylate buffer at a pH of 7.4. Samples were then rinsed three times of 10 minutes each in 0.1 M sodium cacodylate buffer and postfixed with 1% osmium tetroxide in 0.1 M sodium cacodylate buffer for 1 hour. After washing steps, the samples were dehydrated in a graded ethanol series of ethanol ending with propylene oxide. Samples were then embedded in EPON. About 70 nm thin sections were prepared with a Reichert Ultracut E ultramicrotome. The sections were observed using a Philips CM120 electron microscope operating at 120 kV. To map the distribution of gadolinium Nanoparticles in the sample, a LEO 912 microscope operating at 120 kV equipped with an omega filter was used. The images were acquired at the Gd - N_{45} ionization edge.

3.2.5.7 Scanning Electron Microscopy

Samples of fresh adherent cells were fixed for at least 1 hour at room temperature with 2% glutaraldehyde in 0.1 M sodium cacodylate buffer at a pH of 7.4. Samples were then rinsed three times of 10 minutes each in 0.1 M sodium cacodylate buffer and postfixed with 1% osmium tetroxide in 0.1 M sodium cacodylate buffer for 1 hour. After washing steps, the samples were dehydrated in a graded ethanol series of ethanol ending with HMDS and finally metalized with Au-Pa. Scanning Electron Microscopy (SEM) images of particles were performed using the ESEM XL30-FEI microscope equipped with a thermal Field Emission Gun (FEG).

3.2.5.8 Confocal Laser Scanning Microscopy

SQ20B cells were grown for 24 hours on 16-mm round cover glasses placed in the wells of a 24-well plate (seeding density of 50 000 cells per well). Immediately before running the experiment, cells were starved 1 hour and then incubated with Hank's buffered salt solution (HBSS) alone or containing macropinocytosis inhibitor amiloride at 3 mmol/L for another 1 hour at 37 °C, 5% CO₂. Then, 0.6 mmol/L of GBNS (4Si-DTPA coupled to Cy5.5, batch 74-4Si) were added to the culture medium for 1 hour. Cells were rinsed and fixed with PFA 4% for 10 minutes RT before incubating with Hoechst 5 µmol/L for 10 minutes. Cells were rinsed again and cover glasses were removed, mounted on slide with Fluoroprep. Confocal microscopy was performed on the Axiovert 200 LSM510 LNO Meta microscope (Carl Zeiss, Jena, Germany) using a 40x oil immersion objective of 1.2 Numeric Aperture (N.A.). The 633 nm laser intensity was set up at 10 % of its maximum intensity and the emission was collected at 650-705 nm.

In a preliminary study, dextran (10 kDa, 0.5 mg/ml) compound specific of macropinocytosis was used to determine the inhibitors efficiency concentration. Dextran was labeled by Alexa-543 and excited at 543 nm and its fluorescence was collected at 560-615 nm (see supporting information).

3.2.6 Supporting Information

“Internalization Pathways of Gadolinium-Based Radiosensitizing Nanoparticles into Cancer Cells”

by Wael RIMA *et al.*

3.2.6.1 Radiosensitizing Efficiency of Particles upon another Type of Cells (U87)

Supplementary Figure I: *In vitro* radiosensitizing effect of gadolinium oxide nanoparticles at 10Gy upon the U87 cells (radiation at 660 keV).

The potentiality of the gadolinium-based nanoparticles (GBNSs) to be efficient radiosensitizers was evaluated in the case of U87 cells by using the single-cell gel electrophoresis comet assay (instead of the clonogenic survival assay). After incubation under different conditions varying the Gd content, U87 were submitted to a gamma irradiation at the energy of 660 keV (^{137}Cs). The irradiation efficiency was evaluated by measuring the mean tail moment which corresponds to the number of DNA damages such as single and double strands breaks, the formation of apurinic sites, the alkylation and oxidative alterations... that occurred during the irradiation. Figure I shows that, whatever the concentration of Gd-based particles, the mean tail moment is greater than that obtained without particles (the moment is always greater than 50 in a.u. whereas it is less than 40 in absence of particles). However, the formation of DNA damage does not systematically increase with the content of particles since Figure I shows that the curve presents a maximum for a Gd concentration of 0.5mM in the incubation solution (i.e. a concentration of 6mM within the cell). We then found in this type of cells the same surprising fact: i.e. the maximum of radiosensitizing efficiency does not correspond to the maximum of Gd internalization. The explanation of such a discrepancy is the objective of the paper. Since this discrepancy is found in different tumour cells, the contradiction to explain is not related to a particular type of cell but, on the contrary, consists in a general phenomenon.

3.2.6.2 Determination of the Size Distribution of the Cells From that of the Cell Sections Obtained by Electron Microscopy: Mathematic Formulation

The determination of the cell size distribution has been performed by TEM on resin samples (70 nm thin sections prepared by ultramicrotomy) encapsulating cells. Under these conditions, it is obvious that the diameter of a so-cut cell section is not equal to the cell diameter (the value searched) but is inferior or equal to it. Therefore, when measuring a size distribution from the size measurement of the cells imaged, we obtain the size distribution of the cell sections and not the distribution searched, i.e. that of the cells. It is then necessary to establish a mathematical formulation that permits to obtain the size distribution of the cells knowing that of the cell sections.

3.2.6.2.1 Case of a Homogeneous Distribution of Cells

We denote \bar{R} the radius of the particles (all the particles have the same radius) and $\sigma=0$ the mean standard deviation. In cylindrical coordinates (r,θ,z) , the probability to find an horizontal section comprised between z and $z+dz$ (z being the vertical direction) is simply equal to : $\frac{dz}{R}$. This section has a radius R_{section} , and z and R_{section} are related by the equation:

$$z^2 + R_{\text{section}}^2 = \bar{R}^2 \text{ that implies that: } \frac{-dz}{R} = \frac{1}{R} \frac{R_{\text{section}}/\bar{R}}{\sqrt{1 - \left(R_{\text{section}}/\bar{R}\right)^2}} dR_{\text{section}}. \text{ Since } z \text{ decreases when}$$

R_{section} increases, the probability to find a cell section with a radius comprised between R_{section} and $R_{\text{section}} + dR_{\text{section}}$ ($R_{\text{section}} \leq \bar{R}$) is simply equal to:

$$\frac{1}{R} \frac{R_{\text{section}}/\bar{R}}{\sqrt{1 - \left(R_{\text{section}}/\bar{R}\right)^2}} dR_{\text{section}} = \frac{1}{R} f\left(R_{\text{section}}/\bar{R}\right) dR_{\text{section}}.$$

This density of probability is plotted Figure II-B. Such a density is low for small R_{section} and increases with R_{section} until \bar{R} where the density presents a vertical tangent. As expected:

$$\int_{R_{\text{section}}=0}^{\bar{R}} \frac{1}{R} \frac{R_{\text{section}}/\bar{R}}{\sqrt{1 - \left(R_{\text{section}}/\bar{R}\right)^2}} dR_{\text{section}} = 1$$

which shows that one of the fundamental relations of the probability theory is effectively respected. Finally, when the cell distribution is homogeneous, the average value of the cell section radius $\bar{R}_{section}$ can be easily calculated as a function of the cell radius, \bar{R} , writing that:

$$\bar{R}_{section} = \int_{R_{section}=0}^{\bar{R}} R_{section} \frac{1}{R} \frac{R_{section}/R}{\sqrt{1 - (R_{section}/R)^2}} dR_{section}$$

We find that: $\bar{R}_{section} = \frac{\pi}{4} \bar{R}$ a value, which is obviously inferior to \bar{R} . This relation is important since it shows that, when the cell distribution is approximately heterogeneous (condition that can be experimentally verified when the shape of the size distribution of the cell sections has a shape close to that of Figure II-B), the average radius of the cell distribution is equal to $\bar{R} = \frac{4}{\pi} \bar{R}_{section}$.

3.2.6.2.2 Case of a Heterogeneous Distribution of Cells

When the distribution is heterogeneous (\bar{R} the average radius of the particles, $\sigma \neq 0$), the density of probability (i.e. the size distribution of the cell sections) is modified. If one assumes that the size distribution of the cells is Gaussian, the probability of finding a cell with a radius comprised between R and $R+dR$ is given by the relation:

$$g(R)dR = \frac{1}{\sqrt{2\pi}\sigma} \exp\left(-\frac{1}{2}\left(\frac{R-\bar{R}}{\sigma}\right)^2\right) dR$$

The probabilities of on one hand to find a cell with a radius R and on the other hand to find a section of $\bar{R}_{section} < R$ for a cell with a radius R being independent, the density of probability, $h(\bar{R}_{section})$, to find a cell section of $\bar{R}_{section}$ is simply equal to:

$$h(\bar{R}_{section}) = \int_{R=\bar{R}_{section}}^{\infty} g(R) \frac{f(R_{section}/R)}{R} dR \quad (1)$$

The density of probability, $h(\bar{R}_{section})$, is plotted Figure II-D for different standard mean deviation σ of the cell distribution. It shows that, for low $\bar{R}_{section}$, $h(\bar{R}_{section})$ is, regardless σ , very close to the distribution of the cell sections found in the case of an homogeneous cell distribution, $\frac{1}{R} f\left(\frac{R_{section}}{R}\right)$. On the contrary, for larger $\bar{R}_{section}$, the distribution is modified

essentially by a broadening of the peak at \bar{R} . However, the maximum of this peak is only slightly shifted towards low $\bar{R}_{section}$ since, when σ is multiplied by 100, such a maximum is shifted from 12.5 μm to 12 μm only. Then, if one obtains a size distribution of cell sections with a marked peak, one can conclude that this latter, which is approximately located at \bar{R} , gives immediately the average size of the cell distribution.

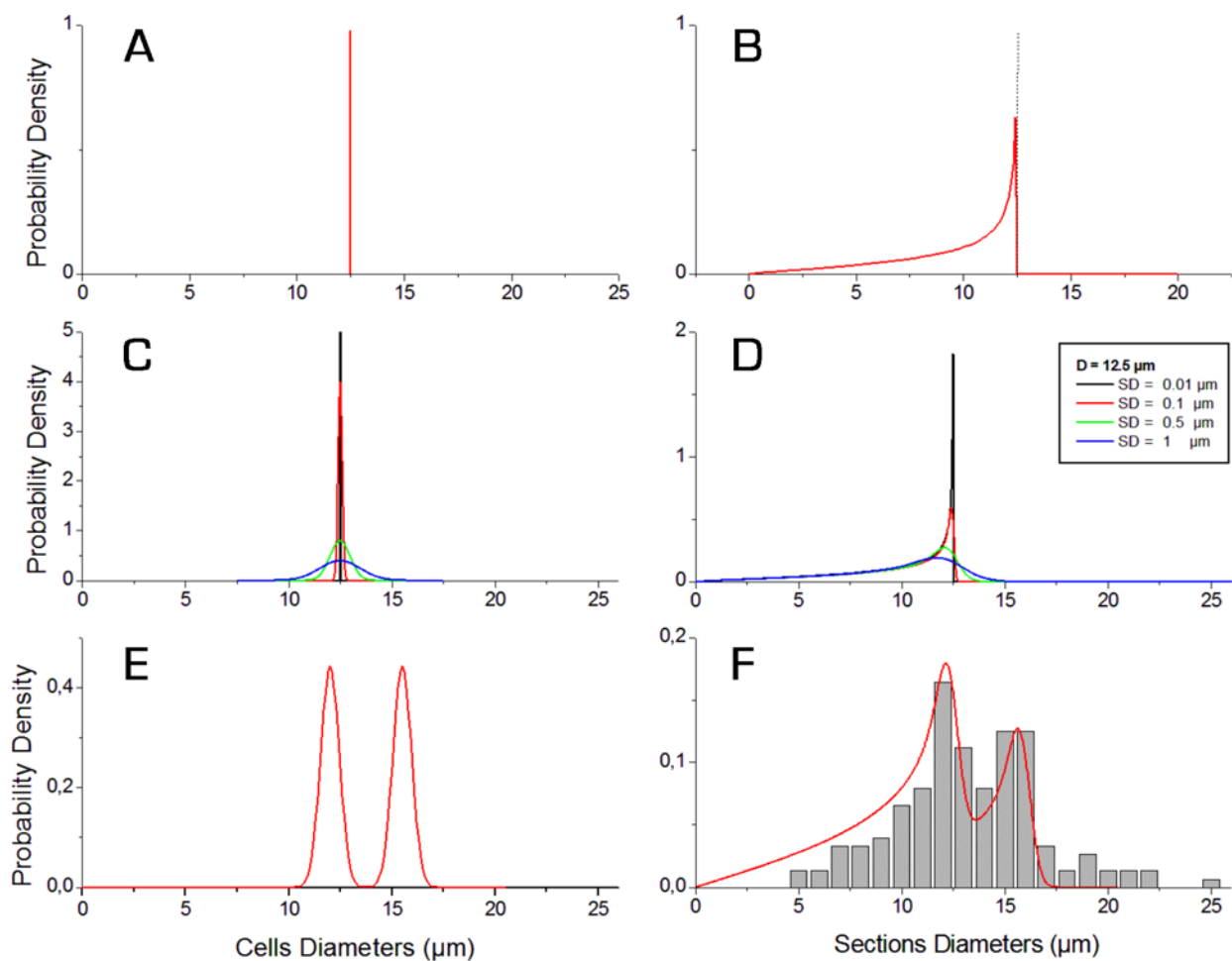
3.2.6.2.3 Size Distribution of the SQ20B Cells

After examination of more than one hundred cell section, one can plot the size distribution of the cell sections, $h(R_{section})$. This latter shows the presence of two maxima peaking respectively at around 12.5 and 16 μm (Figure II-F). Since these maxima are well marked (the full width at middle height being of the order of magnitude of 1 μm), one can infer that the cells are divided in two populations, one with an average radius of around $\bar{R}_1 \approx 6.25 \mu\text{m}$ and the other with $\bar{R}_2 \approx 8 \mu\text{m}$. These results can be improved by the exact calculation of the size distribution of the cells, $g(R)$. To calculate $g(R)$ we first assume that the size distributions of the two cells populations are Gaussian so that $g(R)$ can be written as:

$$g(R) = g_1(R) + g_2(R) = \frac{P_1}{\sqrt{2\pi}\sigma_1} \exp\left(-\frac{1}{2}\left(\frac{R - \bar{R}_1}{\sigma_1}\right)^2\right) + \frac{P_2}{\sqrt{2\pi}\sigma_2} \exp\left(-\frac{1}{2}\left(\frac{R - \bar{R}_2}{\sigma_2}\right)^2\right)$$

$g_1(R)$ and $g_2(R)$ being the Gaussian distributions of the first and second populations respectively. P_1 and P_2 describe the relative proportions of the two populations. Then Relation (1) has been solved by a least-square refinement using the conjugate gradient method. The cell distribution $g(R)$ consists in two Gaussian distributions, a first one concerning 50 % of the cells ($P_1 = 0.5$) with an average diameter of 12.5 μm ($\bar{R}_1 = 6.25 \mu\text{m}$) and a mean standard deviation of 1 μm and a second distribution concerning the other 50 % of the cells ($P_2 = 0.5$) with an average diameter of 16 μm ($\bar{R}_2 = 8 \mu\text{m}$) and a mean standard deviation of 1 μm .

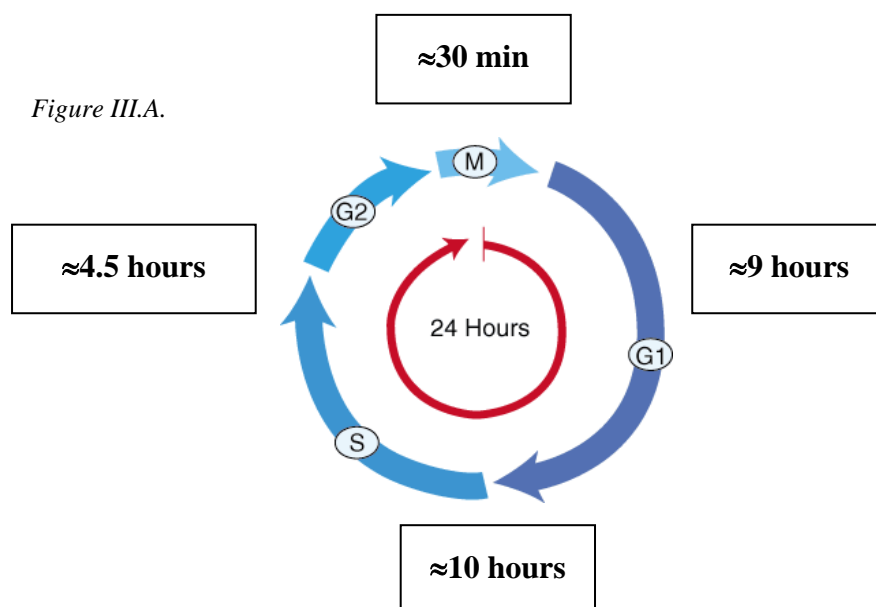
Supplementary Figure II: Measured diameters distribution on thin sections from TEM clichés and cell cycle phases for rapidly replicating human cells.



3.2.6.3 Description of the Cell Cycle

3.2.6.3.1 The Different Phases of a Cell Cycle

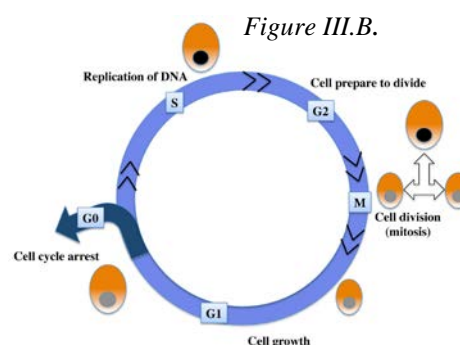
Supplementary Figure III-A: Cell cycle



The cell cycle is divided into four major phases: G1, S, G2 and M. In cycling (replicating) somatic cells, cells synthesize RNAs and proteins during the **G1** phase, preparing for DNA synthesis and chromosome replication during the **S** (Synthesis) phase. After progressing through the **G2** phase, cells begin the complicated process of mitosis, also called the **M** (mitotic) phase when the cell division occurs, yielding two daughter cells (under certain conditions, cells exit the cell cycle during G1 and remain in the G0 state as nondividing cells). Rapidly replicating human cells progress through the full cycle in about 24 hours.

3.2.6.3.2 Relative Duration of Cell Cycle Phases for Rapidly Replicating Human Cells

G1 is typically the longest phase of the cell cycle. This can be explained by the fact that G1 follows cell division in mitosis. Cells usually remain in G1 for about **9 hours** of the 24 total hours of the cell cycle. The length of S phase varies according to the total DNA that the particular cell contains; the rate of synthesis of DNA is fairly constant between cells and species. Usually, cells will take about

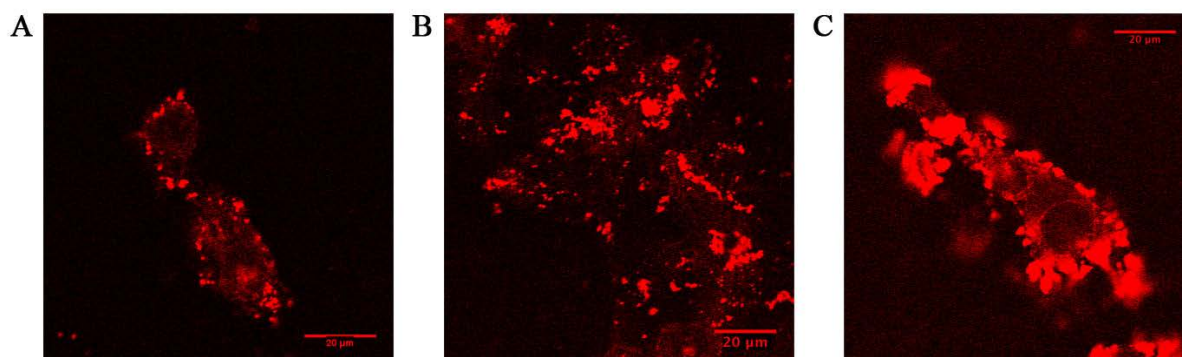


10 hours to complete S phase. G2 is shorter, lasting only about **4.5 hours** in most cells. Mitosis takes about **30 minutes**.

3.2.6.4 Confocal Imaging of the Vesicles Containing Agglomerates as a Function of the Incubation Concentration

After particles incubation with cells at different Gd concentration, confocal imaging can be performed. Agglomerates are also visible as red points due to the fluorescence of Cy5.5 encapsulated within the shell of the GBNSs. As already observed using electron microscopy, the quantity of agglomerates internalized increases when the concentration varies from 0.1 to 0.6 mM. Agglomeration is also observed on the surface cell. In the case of incubation at 2 mM, the quantity of particles attached on particles surface is so large that it impedes a correct visualization of the cell slice to observe (the fluorescence of out-of-focus particles below and above the cell completely masking that of the slice of interest).

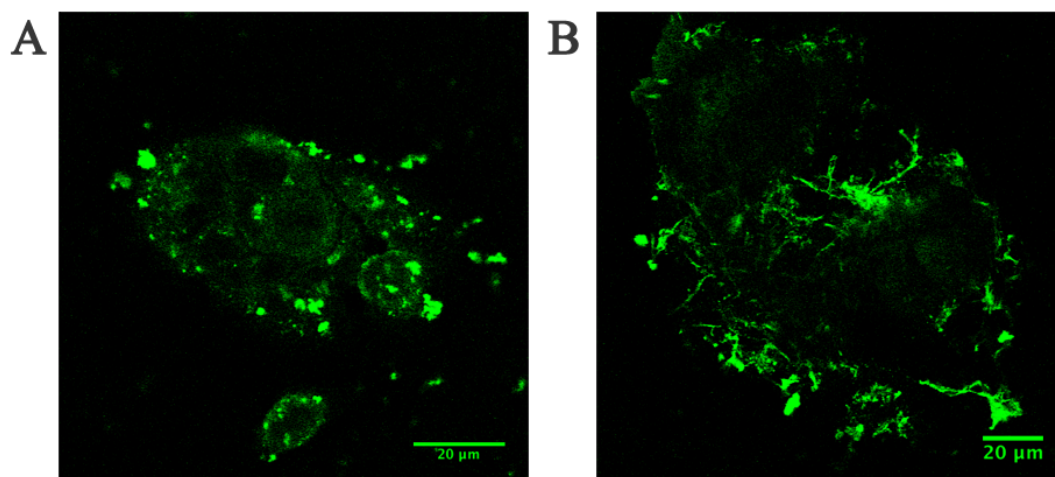
Supplementary Figure IV-A: Evidence of agglomerates entry by macropinocytosis. Fluorescence confocal imaging (excitation power 5 %) of SQ20B cells incubated with particles at a concentration of 0.1 mM (A), 0.6 mM (B), 2 mM (C).



3.2.6.5 Determination of Optimal Concentration of Inhibitors in Order to Evaluate the Entry Process of GBNs into Cells

The optimal concentration of inhibitor of macropinocytosis has been first determined using dextran as the entity to internalize (dextran being known to enter by this process). This concentration has been found equal to 3 mmol/L. Figure V permits to appreciate the efficiency of the inhibitor since it compares the dextran entered by macropinocytosis in absence (Figure V-A) and in presence of amiloride (Figure V-B).

Supplementary Figure IV-B: SQ20B cells incubated with dextran 10kDa (green dots) in HBSS alone (A) or in HBSS containing the inhibitor of macropinocytosis, i.e. the amiloride (B).



Supplementary Table V: Experimental conditions of inhibitors and compounds used for confocal microscopy experiments for macropinocytosis, clathrin- and caveolin-dependant endocytosis.

Mechanism	Inhibitor	Inhibitor optimal concentration	Fluorescent molecule	Fluorescent molecule optimal concentration
Macropinocytosis	Amiloride	3 mM	Dextran	0.5 mg/mL
Clathrin-dependant endocytosis	Amantadine	50 mM	Transferrin	5 μg/mL
Caveolin-dependant endocytosis	Nystatine	0.5 μM	Cholera Toxin B	1 μg/mL

SQ20B cells were grown for 24 hours on 16-mm round cover glasses placed in the wells of a 24-well plate (seeding density of 50 000 cells per well). Immediately before running the experiment, cells were starved 1 hour and then incubated with HBSS alone or containing amiloride 3 mM, amantadine 50 mM or nystatine 0.5 μM for another 1 hour at 37°C, 5 % CO₂. Those inhibitors were used to block macropinocytosis, clathrin and caveolin-coated pits, respectively. Then, 0.6 mM in Gd of gadolinium-based nanoparticles (coupled to Cy5.5 fluorophore) were added to the culture medium for 1 hour. Cells were rinsed and fixed with PFA 4% for 10 minutes at room temperature. Cells were rinsed again and cover glasses were

removed and mounted on slide with Fluoroprep. Confocal microscopy was performed on the Axiovert 200 LSM510 LNO Meta microscope (Carl Zeiss, Jena, Germany) using a 40x oil immersion objective of 1.2 Numerical Aperture. The 633 nm laser intensity was set up at 5 % of its maximum and the emission was collected at 650 – 705 nm.

In a preliminary study, compounds specific of each internalization pathway were used to determine the inhibitors optimal concentration. Dextran (10 kDa, 0.5 mg/mL) was used as a compound internalized through macropinocytosis, Transferrin (5 µg/mL) for clathrin and Cholera Toxin B (1 µg/mL) for caveolin. All these compounds were labeled by Alexa-543 and excited at 543 nm and their florescence were collected at 560 – 615 nm.

3.2.6.6 Additional FCS Results

Supplementary Table VI-A: Fluorescence correlation spectroscopy measurements of the hydrodynamic radius as a function of the distance to cell membrane for different particles concentration in HBSS 1h30 after dilution: 0.1, 0.6 and 2 mM (related to Figure 29). r_{\max} (nm): maximum size of the aggregates; D_{mean} (µm): mean distance of maximum size aggregates from the cell membrane; D_{min} (µm): distance from the cell membrane without aggregates.

Concentration of GBNS	0.1 mM	0.6 mM	2 mM
r_{\max} (nm)	114	681	1099
D_{mean} (µm)	100	50	20
D_{min} (µm)	20	35	10

Supplementary Table VI-B: Fluorescence intensity determined by confocal microscopy in the cytoplasm of SQ20B cells after 1 hour of GBNS incubation. Those measures were made to quantify passive diffusion of the GBNS with laser power at 60% for incubation made at 4°C. In those conditions, fluorescence intensities augmented with GBN dose. For laser power at 5%, the measures were made at 37°C: the maximum of intensity was too high to quantify passive diffusion. The data are related to Figure 30 and expressed as mean of fluorescence intensity in 8-bit pictures (scale from 0 - 256).

	0.1 mM	0.6 mM	2 mM
Laser Power 60%	2	10	12
Laser Power 4%	200	200	200
α	1500	300	250

3.3 Article III. *In Vitro* Radiosensitizing Effects of Ultrasmall Gadolinium-Based Particles on Tumour Cells

Status: *Published in Journal of Nanoscience and Nanotechnology*



Copyright © 2011 American Scientific Publishers
All rights reserved
Printed in the United States of America

Journal of
Nanoscience and Nanotechnology
Vol. 11, 1–7, 2011

***In Vitro* Radiosensitizing Effects of Ultrasmall Gadolinium Based Particles on Tumour Cells**

P. Mowat¹, A. Mignot¹, W. Rima², F. Lux¹, O. Tillement¹, C. Roulin³, M. Dutreix³, D. Bechet⁴, S. Huger⁴, L. Humbert⁴, M. Barberi-Heyob⁴, M. T. Aloy⁵, E. Armandy⁵, C. Rodriguez-Lafrasse⁵, G. Le Duc⁶, S. Roux⁷, and P. Perriat^{2,*}

¹LPCML, UMR 5620 CNRS, Université de Lyon, Université Claude Bernard, Bât. Berthollet, 2ème étage, 22 rue Gaston Berger, 69622 Villeurbanne Cedex, France

²MATEIS, Université de Lyon, INSA-Lyon, 20 av. Albert Einstein, 69621 Villeurbanne Cedex, France

³Institut Curie, Equipe, "Recombinaison et instabilité des génomes", UMR 2027, Orsay, France

⁴Centre de Recherche en Automatique de Nancy (CRAN), Nancy-University CNRS, Centre Alexis Vautrin, Vandœuvre-Lès-Nancy, France

⁵EA 3738, Ciblage Thérapeutique en Oncologie, Equipe 4: Radiorésistance des cellules tumorales, Faculté de Médecine Lyon-Sud, Université Lyon 1, BP 12 69921 Oullins Cedex, France

⁶Biomedical Beamline European Synchrotron Radiation Facility (ESRF), 6 rue Jules Horowitz, BP 220, Grenoble, France

⁷Institut UTINAM, Université Franche-Comté, UMR CNRS 6213, Equipe Nanosciences, Capteurs et Membranes, Besançon, France

Since radiotherapy is widely used in cancer treatment, it is essential to develop strategies which lower the irradiation burden while increasing efficacy and become efficient even in radio resistant tumors. Our new strategy is relying on the development of solid hybrid nanoparticles based on rare-earth such as gadolinium. In this paper, we then evidenced that gadolinium-based particles can be designed to enter efficiently into the human glioblastoma cell line U87 in quantities that can be tuned by modifying the incubation conditions. These sub-5 nm particles consist in a core of gadolinium oxide, a shell of polysiloxane and are functionalized by diethylenetriaminepentaacetic acid (DTPA). Although photoelectric effect is maximal in the [10–100 keV] range, such particles were found to possess efficient *in-vitro* radiosensitizing properties at an energy of 660 keV by using the "single-cell gel electrophoresis comet assay," an assay that measures the number of DNA damage that occurs during irradiation. Even more interesting, the particles have been evidenced by MTT assays to be also efficient radiosensitizers at an energy of 6 MeV for doses comprised between 2 and 8 Gy. The properties of the gadolinium-based particles give promising opening to a particle-assisted radio-therapy by using irradiation systems already installed in the majority of hospitals.

3.3.5 Supporting Information

3.3.5.1 Characterization of Gd-Based Particles

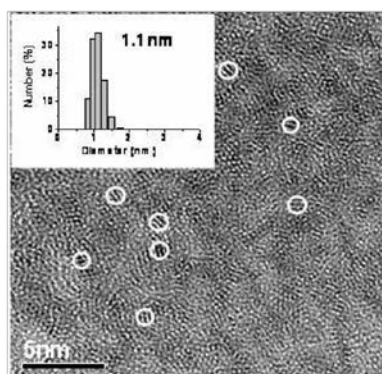


Figure 35: Image of non-irradiated gadolinium oxide nanoparticles obtained by High-Resolution Transmission Electron Microscopy (JEOL 2010F microscope 200kV, Tokyo, Japan) and the size distribution of the cores. The shape of gadolinium oxide cores is nearly spherical and the size distribution is homogenous with an average around 1.1nm.

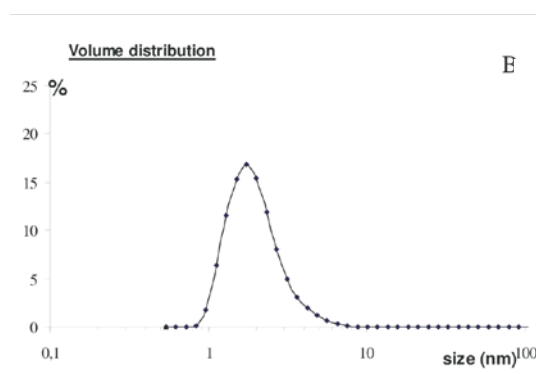


Figure 36: Hydrodynamic size of core/shell particles (sub-5nm).

3.3.5.2 Viability of the U87 Cells after Particles Internalization

Table 6: Viability of U87 glioblastoma cells incubated with Gd-based particles for 1h at 37°C/5%CO₂/100% humidity in complete DMEM.

[Gd] mM	0	0.1	0.2	0.5	1	5
Normalized cells viability (%)	100	100	100	99	68	58

Table 6 shows the viability of cells (normalized in relation to the control), evaluated by the well known technique using Trypan blue after an incubation of 1h, in function of the Gd concentration initially added in the medium. Particles do not present any toxicity for Gd concentrations until 0.5mM. After 1mM, cells are affected.

3.3.5.3 Location of the Particles within the Cytoplasm

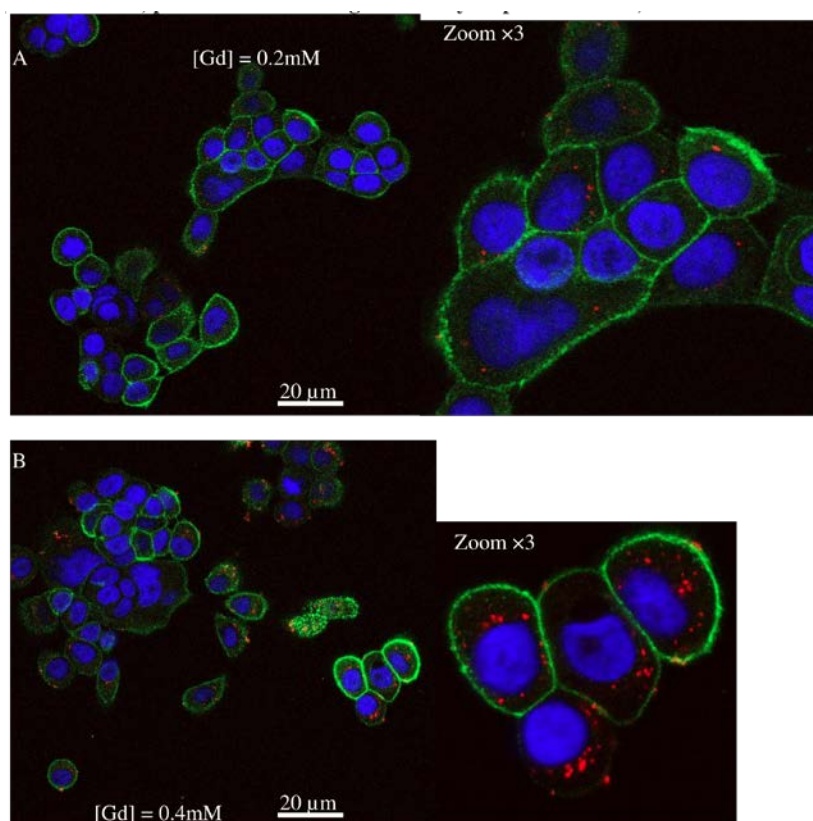


Figure 37: Particles location in cells evaluated by confocal microscopy (G ×63) (nucleus = blue; plasma membrane = green and cy5.5-particles = red).

All the images observed (from confocal or electron microscopy) show that the particles always lie in the cytoplasm. Even in died cells, particles never attain the nucleus.

3.3.5.4 Details upon Comet Assays

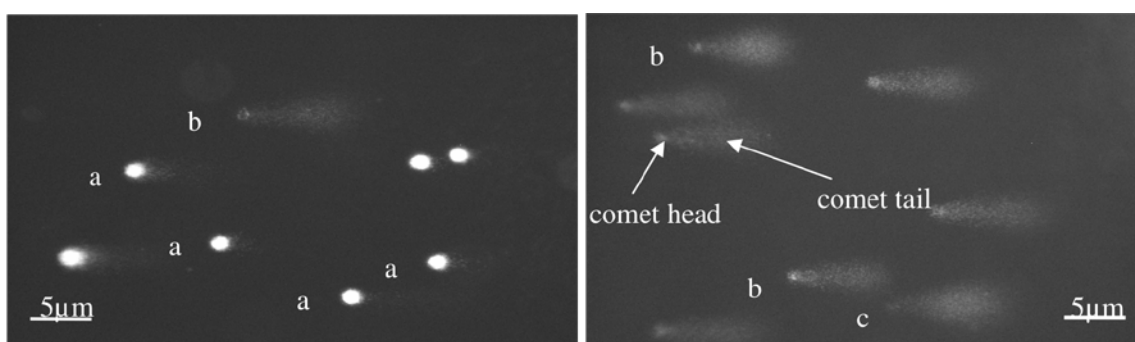


Figure 38: Some images of comets for different alterations of cells. The head of the comets corresponds to DNA without breaks (compact DNA). The tail of comets corresponds to DNA with single-strand breaks (SSB). Three types of comets can be observed: (a) Absence of DNA breaks; (b) Presence of DNA breaks; (c) Entirely broken DNA = apoptotic form.

3.3.5.5 Formation of Particles Aggregates within the Cells

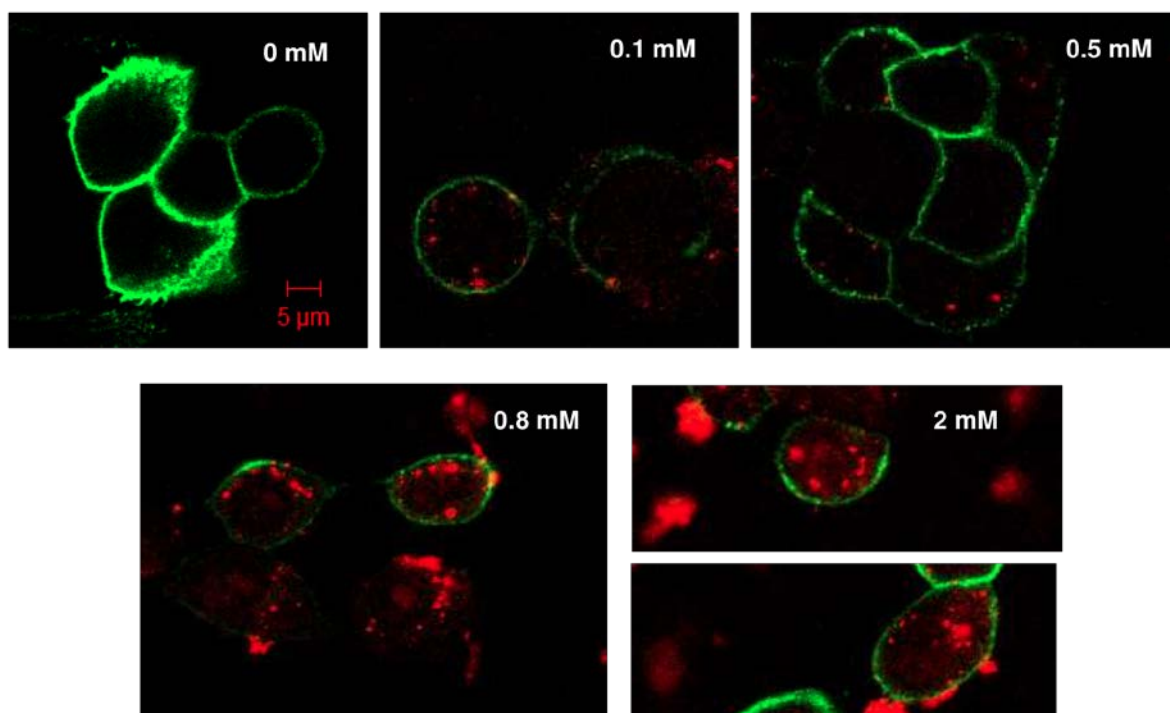


Figure 39: Series of confocal imaging for increasing concentrations.

These series of images clearly show that within the cells, Gd-based particles tend to severely agglomerate. Then there is formation of aggregates whose size increases with the particles concentration (in the images above, the concentration is given in mmol of Gd per liter of solution and corresponds to the concentration of the incubation solution). For the higher concentrations agglomerates can also be formed in the solution.

3.3.5.6 Details on Transmission Electron Microscopy

In order to visualize the particles internalized in the U87 cells, we have used the following procedure. Cells were fixed with 2% glutaraldehyde, centrifuged at 300 g for 10 minutes at room temperature and washed three times in 0.1 M sodium cacodylate buffer. The pellets (i.e. the cells remaining at the bottom of the tubes) were then coated in agarose and postfixed in 1% osmium tetroxide. After washing, samples were dehydrated by graded series of ethanol, embedded in Epon and finally cut by ultramicrotomy. Observations were realized using a Philips CM120 electron microscope operating at 120 keV and equipped with an EDX analysis useful for distinguishing the Gd-based particles from particles rich in ferritin or clusters arising from the gathering of osmium or lead atoms.

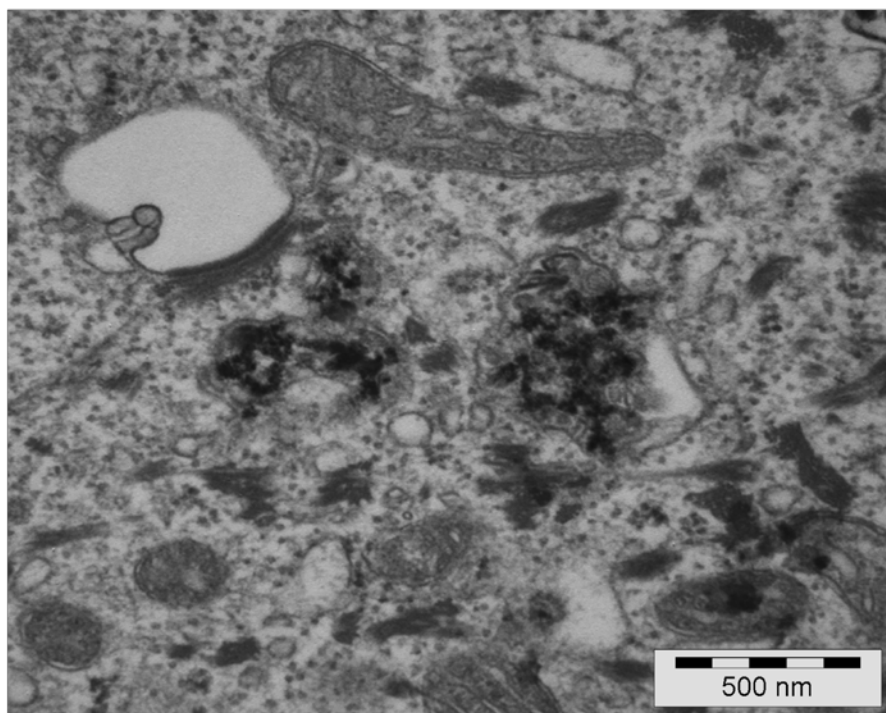


Figure 40: Electron image of Gd-based particles within cells for a concentration of 0.6 mM.

Figure 40 shows that particles enter in cells via endocytosis. They are then gathered in endosomes separated from the rest of the cytoplasm by a double barrier. Within the endosome, the particles form a lot of aggregates. This observation confirms those obtained by optical microscopy that shows that the size of aggregates increases with the particles concentration.

3.3.5.7 Mechanisms of DNA Repair

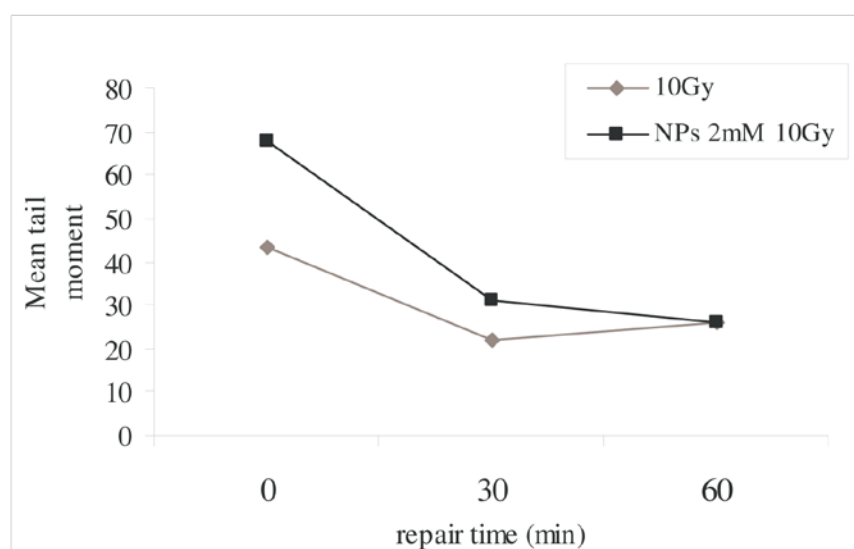


Figure 41: U87 glioblastoma cells repair after irradiation at 10 Gy in the case where cells have been previously incubated in a solution of Gd-based particles at 2mM (black) or not (gray).

Figure 41 shows the mean tail moment (indicator of the number of single-strand DNA breaks) as a function of the repair time after irradiation. Regardless of the repair time, the number of DNA breaks is superior when the cells have been previously incubated in a solution containing particles. This shows that gadolinium oxide based nanoparticles have an *in vitro* radiosensitizing effect. After irradiation, cells are placed under favorable conditions of culture so that some cellular repair can be engaged. Then, the number of DNA breaks decreases for both curves in a similar way. This shows that the repair mechanisms are the same in both cases, which means that the DNA breaks induced in presence of particles are of the same nature than those occurring under irradiation alone.

3.4 Gadolinium-Based Nanoparticles: Towards *in vivo*

Ultrasmall gadolinium-based nanoparticles (GBNs), the same used for *in vitro* studies, induce both positive contrast for magnetic resonance imaging (MRI) and a radiosensitizing effect using microbeam radiation therapy achieving a better selectivity as demonstrated by the studies performed at ESRF. What distinguishes MRT from conventional radiotherapy (broad beam) is that normal tissue is more preserved despite the delivery of high doses. MRT uses arrays of narrow ($\approx 25\text{-}100\ \mu\text{m}$) microplanar beams (peaks) separated by wider ($100\text{-}400\ \mu\text{m}$ center-to-center) microplanar spaces (valleys).^[cxxxv] The application of MRT to the treatment of rats bearing intracerebral 9L glioblastoma (9LGS) led to a greater increase in lifespan of the rats after intravenous injection of GBNs. The radiosensitizing effect of GBNs can be activated by the X-ray microbeams when the gadolinium content is sufficiently high in tumor and low in surrounding healthy tissue (**Figure 42**).

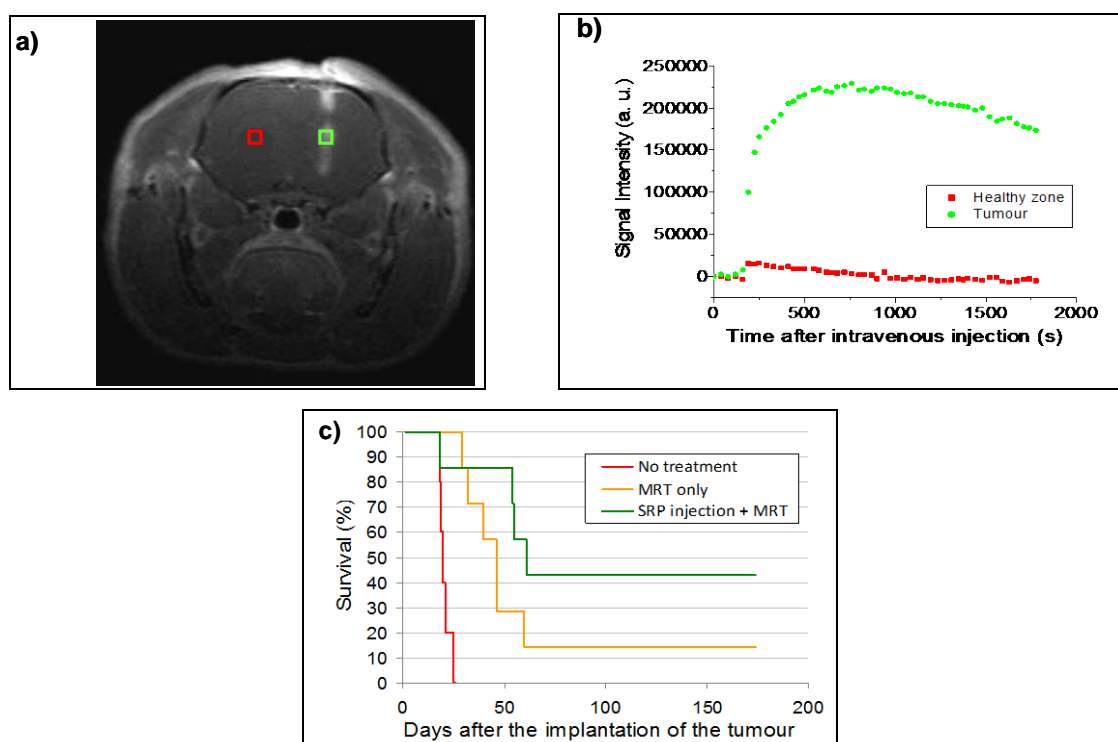


Figure 42: a) T1 weighted image of the brain of a 9LGS-bearing rat 5 minutes after the injection of GBNs. Red area: localization in the healthy zone, green area: localization in the tumoral zone. b) Temporal evolution of the MRI signal in tumour and in normal tissue in the left hemisphere. c) Survival curves comparison obtained on 9LGS-tumour bearing rats without treatment, only treated by MRT, treated by MRT 1 hour after GBNs injection during 175 days after tumour implantation. The MRT irradiation was done in cross-fired mode, using 50 microns wide microbeams, with a spacing of 211 microns in between the beams. The skin entrance dose was set up at 400 Gy for the peak and 20 Gy for the valley.

To observe interactions of GBNs with the tumor at a microscopic scale, the 9LGS-bearing rats were fixed by perfusion with solution of glutaraldehyde. Perfusion was performed in order to obtain satisfactory preservation of the nervous system, which requires rapid and uniform

penetration of the fixing agent into all parts without prior injury to the tissue. The difficulty remains the preservation of the fine structures of neurons, glia, nerve fibers, and synapses. The only way to accomplish this aim is perfusion of the fixing agent through the vascular channels. **Figure 43** below shows a schematic of neuron.

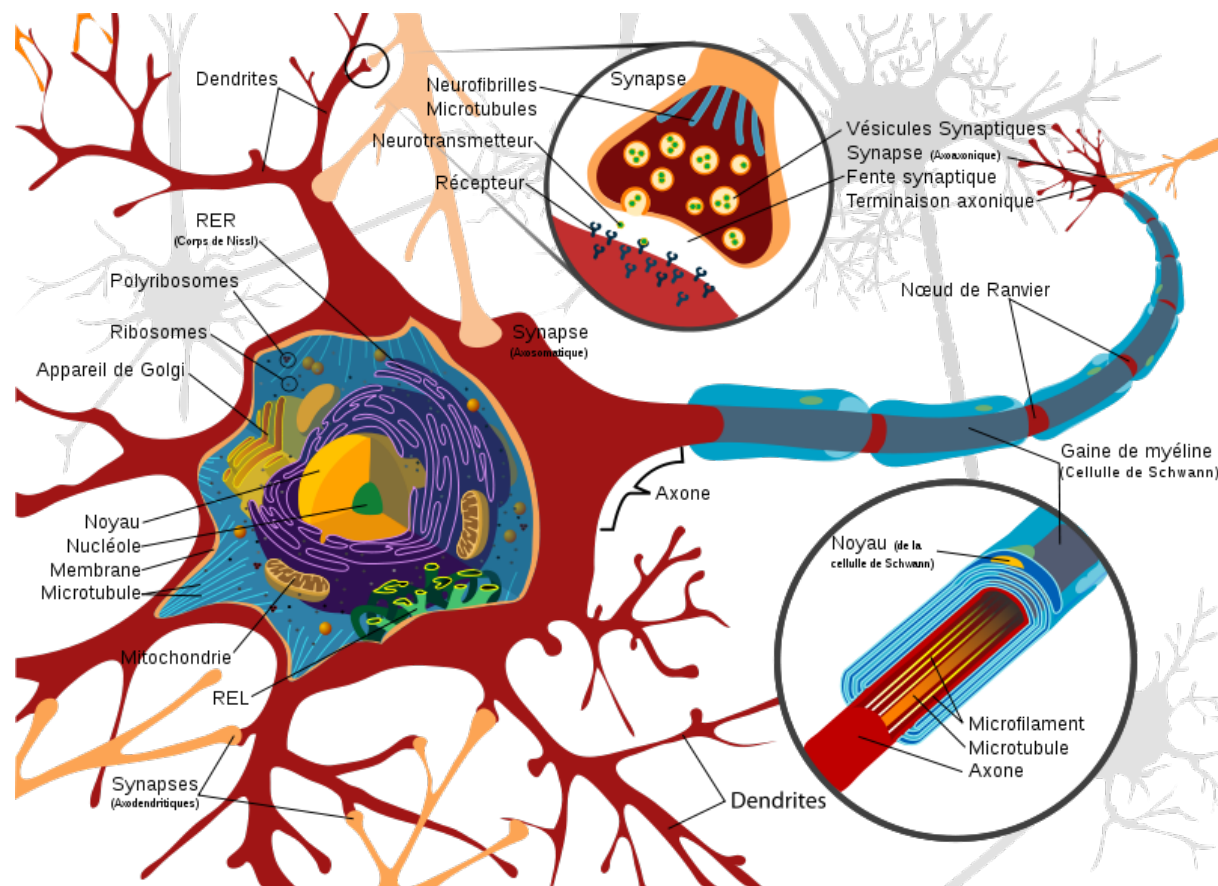


Figure 43: Schematic of neuron.

A neuron has many processes (cytoplasmic extensions), called dendrites, which enter a large, grey cell body at one end. A single process, the axon, leaves at the other end, extending towards the dendrites of the next neuron or to form a motor endplate in a muscle. Dendrites are usually short and divided while the axons are very long and does not branched freely. The impulses are transmitted through the motor neuron in one direction, i.e. into the cell body by the dendrites and away from the cell body by the axon . The cell body is enclosed by a cell (plasma) membrane and has a central nucleus. Granules, called Nissl, bodies are found in the cytoplasm of the cell body. Within the cell body, extremely fine neurofibrils extend from the dendrites into the axon. The axon is surrounded by the myelin sheath, which forms a whitish, non-cellular, fatty layer around the axon. Outside the myelin sheath is a cellular layer called the neurilemma or sheath of Schwann cells. The myelin sheath together with the neurilemma is also known as the medullary sheath. This medullary sheath is interrupted at intervals by the

nodes of Ranvier. Unfortunately, it was very difficult to observe nanoparticles in brain specimen (healthy and cancer tissue) prepared for electron microscopy (**Figure 44**).

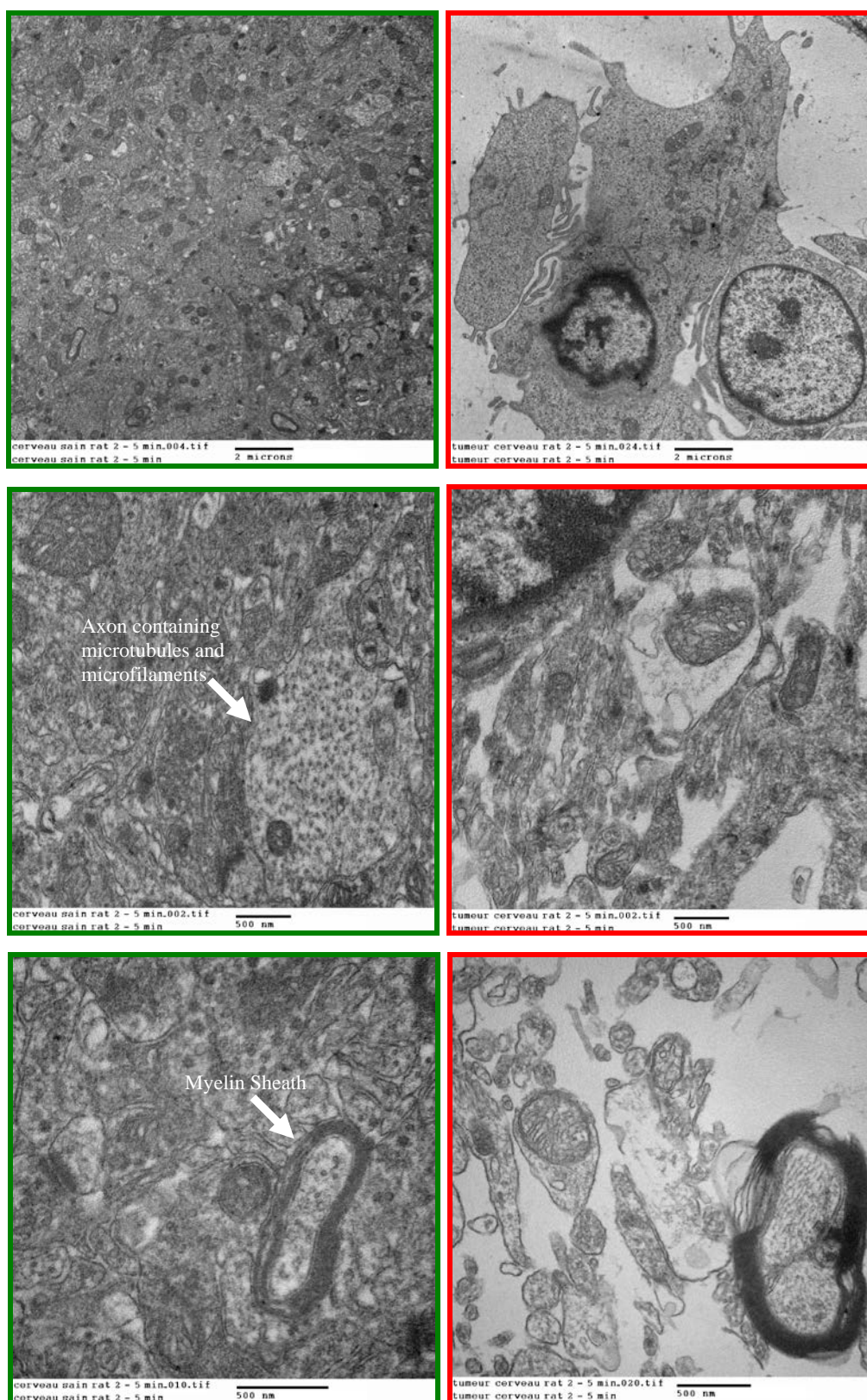


Figure 44: Bright-field TEM images slices of a rat brain tumor (red area) and its corresponding healthy tissue (green area) showing the complexity of the nervous tissue.

Two hypothesis were emitted: (1) gadolinium nanoparticles are present in the brain tumor but they do not agglomerate and, due to their very small size (< 5 nm), it is impossible de distinguish them in the brain ultrastructure, (2) gadolinium nanoparticles were eliminated from brain vascular channels during washing step before fixation.

This study is always in progress. One perspective would be to remove the brain tumor and fixed it by immersion without washing. This will increase the chances of observing the particles in the brain by TEM even if the structure of the latter will not be as well preserved as with fixation by perfusion.

3.5 Conclusion of Part Three

Sub-5 nm gadolinium-based nanoparticles (GBNs), developed for imaging-guided radiotherapy possess an *in vitro* efficient radiosensitizing effect even at moderate concentration when incubated with two radioresistant cancer cell lines: head and neck squamous cell carcinoma cells (SQ20B) and glioblastoma cells (U87).

To further understand this phenomenon and optimize it, we use diverse types of microscopy techniques, in particular electron microscopy that possesses a resolution sufficient to determine the mechanisms responsible for particle uptake in SQ20B cells. Two main cellular internalization mechanisms were then evidenced and quantified: passive diffusion and macropinocytosis. Whereas the amount of particles internalized by passive diffusion is not completely sufficient to induce, *in vitro*, a significant radiosensitizing effect, the cellular uptake by macropinocytosis, which is only significant in a limited range of GBNs incubation concentration, may lead to a successful radiotherapy. Macropinocytosis processes in two steps: formation of agglomerates at vicinity of the cell followed by recuperation of the agglomerate by the lamellipodia (i.e. the “arms”) of the cell. The first step is strongly dependent on the physicochemical characteristics of the particles, especially their zeta potential that determines the size of the agglomerates and their distance from the cell, which are the parameters that render possible their collect *via* the lamellipodia.

Ultrasmall gadolinium-based nanoparticles (GBNs), the same used for *in vitro* studies, induce both positive contrast for magnetic resonance imaging (MRI) and a radiosensitizing effect using microbeam radiation therapy (MRT) achieving a better selectivity as demonstrated by the studies performed at ESRF. The application of MRT to the treatment of rats bearing intracerebral 9L glioblastoma (9LGS) led to a greater increase in lifespan of the rats after intravenous injection of GBNs. The radiosensitizing effect of GBNs can be activated by the X-ray microbeams when the gadolinium content is sufficiently high in tumor and low in surrounding healthy tissue. To observe interactions of GBNs with the tumor at a microscopic scale, the 9LGS-bearing rats were fixed by perfusion with solution of glutaraldehyde. Unfortunately, it was very difficult to observe nanoparticles in brain specimen (healthy and cancer tissue) prepared for electron microscopy due to the complexity of the nervous tissue.

4 Part Four. Internalization Studies of Silica Particles of Variable Sizes

4.1 Introduction of Part Four

The following work concerned: (1) the internalization *in vitro* of fluorescent silica nanoparticles with different sizes and the same surface coating into macrophages, and (2) *in vivo* experiments of silica nanoparticles with a gold core for the diagnosis of human colorectal cancer.

Silica particles were developed according to the synthesis method used by Nano-H society. They were obtained using the inverse microemulsion method that allows the synthesis of a silica core encapsulated in a polysiloxane shell. First, inverse micelles were created by separating the aqueous phase from the apolar organic one. Each micelle served as a nano-reactor accumulating within it all the reagents (silica, silanes, fluorophores, catalysers), creating then compact objects without coalescence of particles nearby. Indeed, during the synthesis, since chemical species are polar, the equilibrium constant of reagents is in favor of the aqueous phase. Nucleation reactions and gelification (sol-gel) will take place inside the micelles. Immobilization of FITC fluorophores took place at the beginning of the reaction during the silica core formation. Synthesis of silica core is performed according to a sol gel procedure in basic medium.^[ccv] The silica core is formed with incorporation of FITC by organic reaction between amniopropyl triethoxylane (NH₂ groups) and the FITC.

The main goal of this part is to bring a better comprehension of the size effect of these particles on the internalization process, biological response and toxicity after 24 hours of contact with macrophages RAW 264.7.

Yuan *et al.*^[clxxvii] tested size-mediated cytotoxicity and apoptosis of FITC-labeled hydroxyapatite nanoparticles (HAPN) in human hepatoma HepG2 cells. They have demonstrated that the size of HAPN in the range 20-180 nm had obvious effect on the cellular uptake and nuclear localization in HepG2 cells. The results showed that the antitumor activity and HAPN-induced apoptosis strongly depended on the size of HAPNS, and the efficacies all decreased in the order of 45 nm > 26 nm > 78 nm > 175 nm. These findings provide strong evidence that the HAPN-induces anti-proliferation affects in HepG2 cells can be modulated by the particle size.

In our study, Nano-H society produced a range of FITC silica nanoparticles with variable sizes functionalized by COOH group. A description of these particles in terms of size, fluorescence, surface coating and concentration is presented in Table 7 below.

Table 7: Recapitulating table of FITC silica nanoparticles with variable sizes.

Name	Date	Expected size (nm)	DLS (nm)	% FITC	Surface function	Volume (mL)	Theoretical number of particles / mL
120-10	1/10/10	150	139 ± 2	3 %	COOH	6	$2,9 \times 10^{13}$
121-10	1/10/10	250	252 ± 4	3 %	COOH	6	$8,2 \times 10^{12}$
122-10	1/10/10	500	492 ± 6	3 %	COOH	6	$9,4 \times 10^{11}$
123-10	1/10/10	850	847 ± 19	3 %	COOH	6	$2,1 \times 10^{11}$

First, physico-chemical parameters of the nanoparticles were examined. Their size distribution was determined using photon correlation spectroscopy (PCS) and transmission electron microscopy (TEM). Their zeta potential was evaluated and fluorescence of FITC was also verified at spectral level.

The following analyses were performed after 24 hours of contact of these different nanoparticles with the macrophages cell line. Internalization of particles was first observed using confocal and electron microscopy, then quantified thanks to the fluorimetry technique coupled with a trypan blue quenching.

This work is detailed in the following publication accepted in *Inhalation Toxicology* journal.

4.2 Article IV. Size of Submicrometric and Nanometric Particles Affect Cellular Uptake and Biological Activity of Macrophages *in vitro*

L. Leclerc, W. Rima, D. Boudard, J. Pourchez, V. Forest, V. Bin, P. Mowat, P. Perriat, O. Tillement, P. Grosseau, D. Bernache-Assollant and M. Cottier.

Status: **Accepted** for publication in *Inhalation Toxicology*

4.2.1 Abstract

Background: Micrometric and nanometric particles are increasingly used in different fields and may exhibit variable toxicity levels depending on their physicochemical characteristics. The aim of this study was to determine the impact of the size parameter on cellular uptake and biological activity, working with well-characterized fluorescent particles. We focused our attention on macrophages, the main target cells of the respiratory system responsible for the phagocytosis of the particles.

Methods: FITC fluorescent silica particles of variable submicronic sizes (850, 500, 250 and 150 nm) but with similar surface coating (COOH) were tailored and physico-chemically characterized. These particles were then incubated with the RAW 264.7 macrophage cell line. After microscopic observations (SEM, TEM, confocal), a quantitative evaluation of the uptake was carried out. Fluorescence detected after a quenching with trypan blue allows us to distinguish and quantify entirely engulfed fluorescent particles from those just adhering to the cell membrane. Finally, these data were compared to the *in vitro* toxicity assessed in terms of cell damage, inflammation and oxidative stress (evaluated by LDH release, TNF- α and ROS production respectively).

Results and conclusion:

Particles were well characterized (fluorescence, size distribution, zeta potential, agglomeration and surface groups) and easily visualized after cellular uptake using confocal and electron microscopy. The number of internalized particles was precisely evaluated. Size was found to be an important parameter regarding particles uptake and *in vitro* toxicity but this latter strongly depends on the particles doses employed.

Key terms: Uptake quantification, macrophages, fluorescent particles, *in vitro* toxicity.

4.3 Silica Nanoparticles: Towards *in vivo*

4.3.1 *Ex vivo* Human Models from Colectomy Specimens for the Diagnosis of Colorectal Cancer with Functionalized Fluorescent Nanoparticles

Status: Draft

Aims and background: The limits of medical and surgical care of colorectal cancer are a late diagnosis and an advanced stage of disease (metastatic), usually not curable. The application of nanobiotechnology to the management of cancer is currently the most important chapter of nanomedicine. However, a major challenge in application of tumor-targeted nanoparticles is tumoral distribution. The development of nanoparticles (NP) specific of colorectal cancer could be a reliable means of detecting dysplastic and cancerous lesions including « flat lesion » during endoscopic procedures. We have developed a spray that can be spread gold fluorescent (fluorescein isothiocyanate, FITC, excitation source 488nm) nanoparticles (40nm of diameter) during endoscopy and surgical procedures. Nanoparticles are conjugated to anti-urokinase activator receptor (anti-uPAR) for active tumor targeting to recognize proteins targets (uPAR) that are overexpressed on the surface of colonic adenocarcinoma cells. The test was performed on two *ex-vivo* post surgical human colectomy specimen.

Materials and methods: On two pieces of right post-colectomy surgery for colon adenocarcinoma tumors pT3 N1, we practiced the vaporization of gold nanoparticles. The amount of NP sprayed for each anatomical area was evaluated by 1 ml of NP-solution. We studied two anatomical regions: tumor (ADK) and healthy tissue (S). The contact time between the NP and the tissues were evaluated on 30 minutes (cell viability of each *ex-vivo*), with and without rinsing with saline solution (5 ml). The biopsies to evaluate the behavior of NP were marked as follows: T = 0 (ADK and S) and T = 30 min (ADK and S), before and after rinsing solution.

Results: We analyzed *ex-vivo* colectomy with a probe detection of FITC during and after contact times with nanoparticles. The validation of these given was made with the analysis of biopsies by ultrastructural electron microscopy using FIB-SEM technique and epifluorescence

microscopy. The results of this initial experience showed an active specific accumulation on the tumor tissue.

Conclusion: Antibody targets will permit the selective use of highly specific-conjugated nanoparticles to accurate fluorescent identification of the malignant lesion. Here we demonstrate that this novel receptor-targeted NP is a potential agent for the detection of colorectal cancer.

4.3.1.1 Utilization of the FIB-SEM Technique

A Focused Ion Beam (FIB) microscope is an instrument that resembles a scanning electron microscope (SEM). While the SEM uses electron beam for imaging, a FIB uses a focused beam of ions for imaging and ablation of materials. Primarily produced commercially for semiconductor industrials, the FIB technique is increasingly used in the biological field due to its ability to provide volumetric information with a voxel dimension down to a few nanometers. Most common FIBs use liquid-metal ion sources (LMIS), especially gallium ion (Ga^+) sources, and may be combined with a SEM in a single instrument (FIB/SEM). In this case, electron and ion columns are positioned to allow the SEM to provide immediate images of the surface milled by the FIB (**Figure 52**).

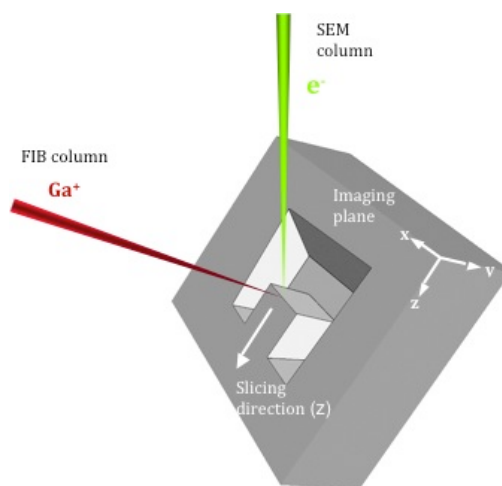


Figure 52: Schematic drawing of the sample in milling position (about 50° tilt, short working distance) with the U-shaped trench milled by the ion beam and the subsequent traces of the slices imaged with the electronic column.

Serial FIB/SEM imaging for this study was performed using a FIB/SEM workstation (NVision 40; Carl Zeiss Microscopy GmbH, Oberkochen, Germany) combining a SIINT zeta FIB column (Seiko Instruments Inc. NanoTechnology, Japan) with a Gemini column. The NVision 40 platform is also equipped with a multiple SIINT gas injection system (GIS). For this instrument, the angle between the FIB and the SEM column is 54°.

The analysed samples were already embedded in resin blocks and the region of interest was rendered plane by a diamond knife. The samples were then glued with a silver paint onto an aluminium stub. To make the surface electrically conductive, the samples were coated with a carbon layer of about 30 nm by (EM SCD500, Leica Microsystems GmbH, Germany). Finally, a carbon layer of about 1 μm of thickness was deposited *in situ* on the region of interest using the gas injection system of the FIB. This thick layer allows achieving sharp edges when cross-sectioning and protects from unwanted sputtering or ion beam changes damage of the outer surface of the specimen.

At low magnification, and using secondary electron imaging (5 kV), the resin block was oriented so that the region of interest and the side of the block to be imaged is facing the operator (**Figure 53-A**). Then the block was oriented so that the face to be imaged lies parallel to the milling beam. This means that electron beam is oriented 36° to this face.

Reaching an ion beam current of 50 pA at 2 kV to erase the amorphous layer due to previous more severe ion milling, a narrow band of resin was removed from the front of the region to be imaged. Figure 53-B shows a view of the block observed with FIB imaging.

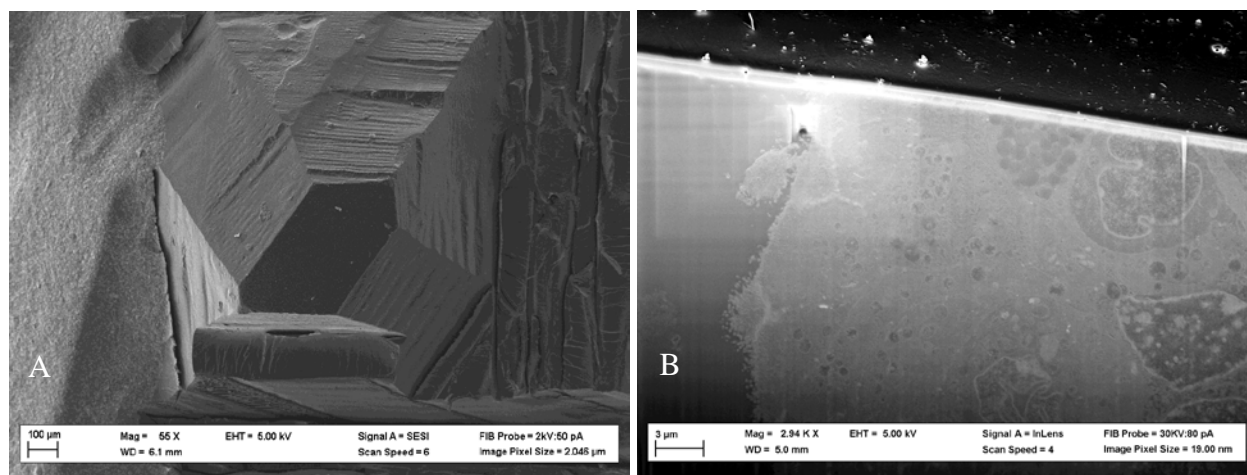


Figure 53: Preparing the block face for FIB/SEM imaging. A) shows illustration of the block and the edge to mill to create the imaging face. B) shows a view of the block observed with FIB imaging (secondary electrons generated by gallium ions) after milling.

To view the milled face and image it, imaging mode was switched to backscattered imaging. A specific BSE detector efficient at low voltage (below 3 kV) was used. Moreover, the electrons collected were filtered with a grid set at a potential inferior to the accelerating voltage (< 1.5 kV). The image obtained possesses a chemical contrast and an enhanced spatial resolution.

In our case, the main advantage of FIB/SEM technique was to image the sample with a representative contrast without using high Z stainers (lead and uranium). Classical bright field TEM micrographs, the first technique used to try to visualize the nanoparticles, were difficult to interpret in presence of these stainers (**Figure 54**).

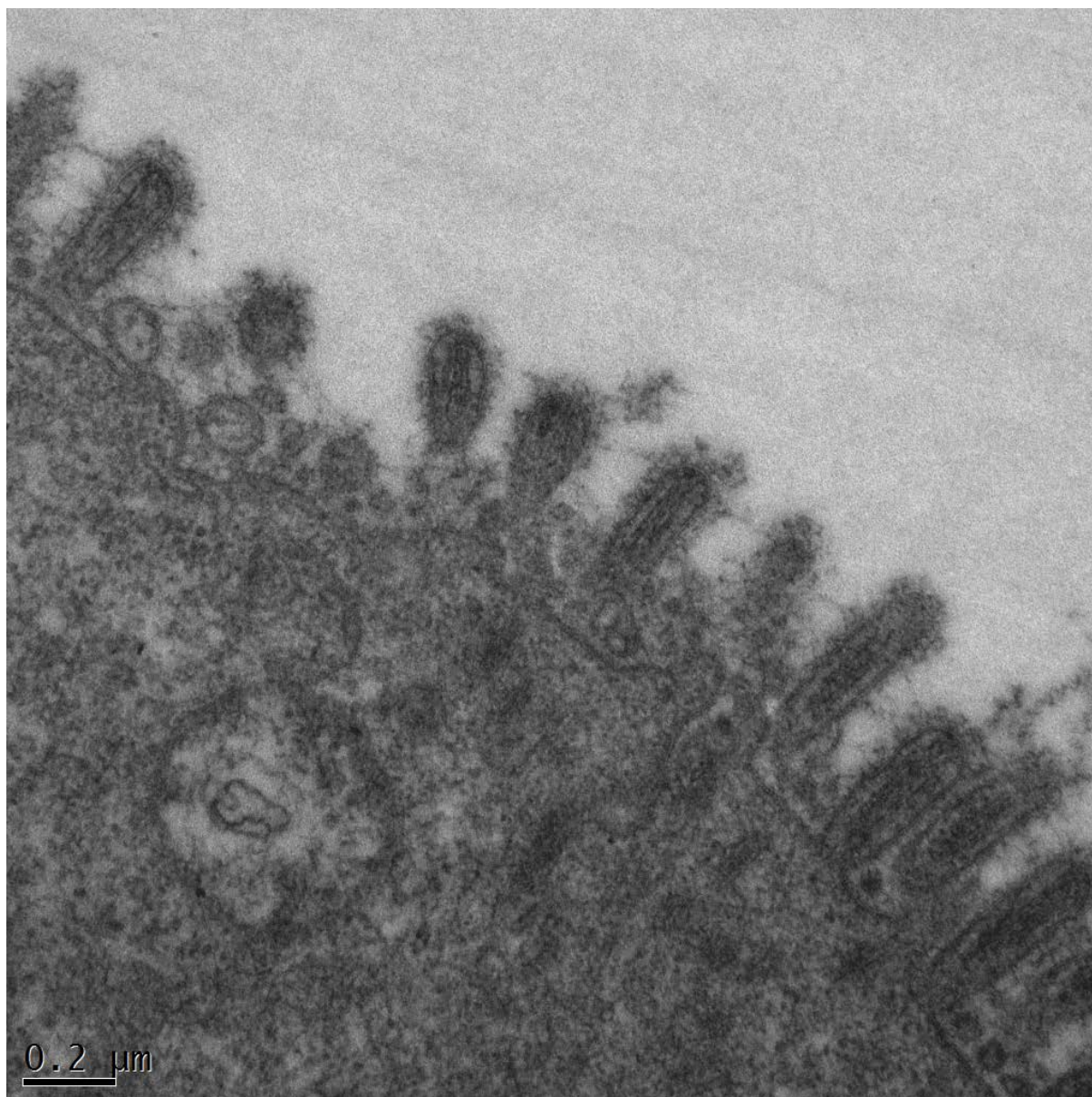


Figure 54: Electron micrograph (longitudinal cut) of an intestinal cell (colon adenocarcinoma tumor pT3 N1) with the microvilli (white arrows).

In FIB/SEM images, organic membrane was visible surrounded by a white border due only to osmium fixation on it. Grey spherical elements (Figure 55, white arrows) with no white border around were visible between microvilli.

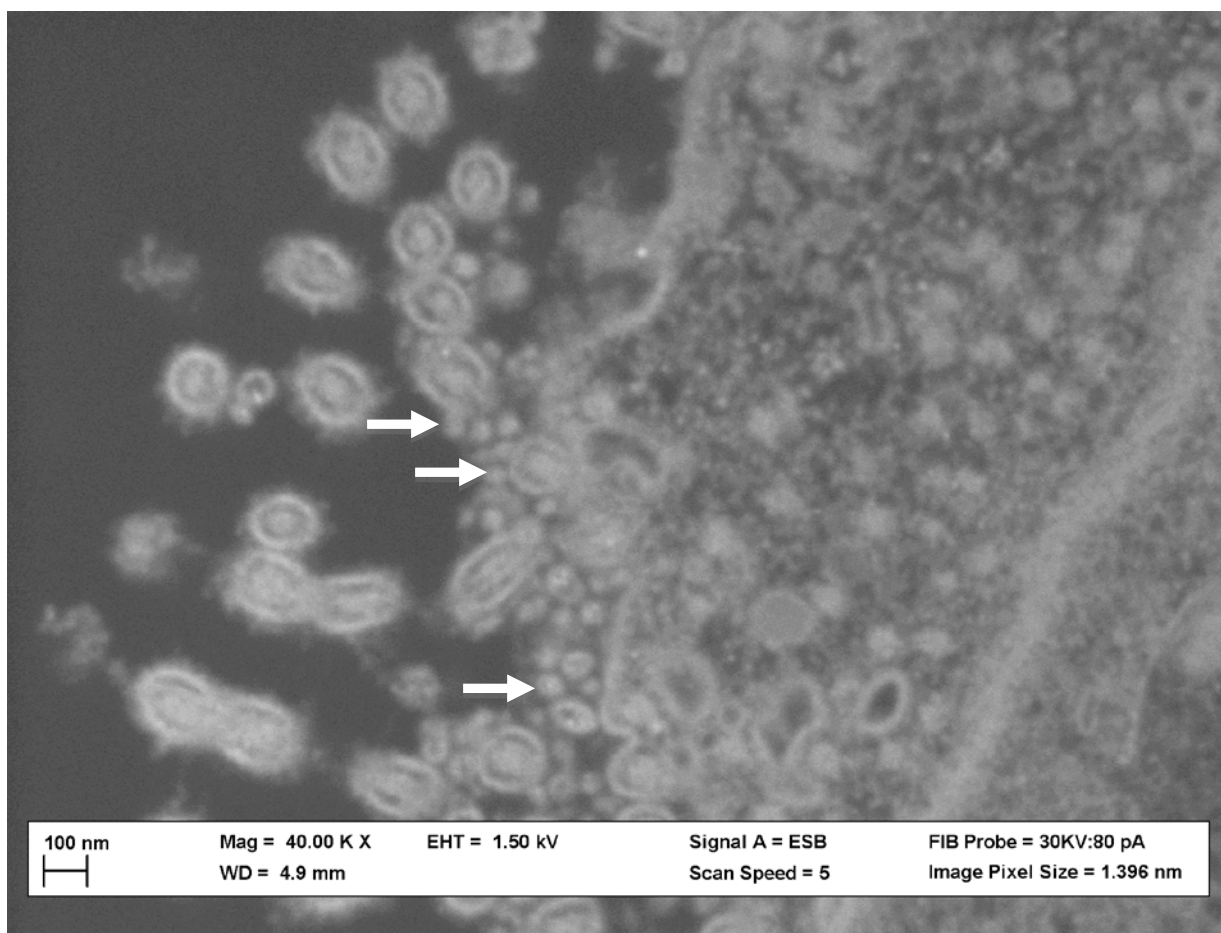


Figure 55: Backscattered image of the block face showing the ultrastructure within a region of the sample. Organic membranes are visible around structures are visible, distinct from silica particles.

Their size (around 40 nm) fits with the announced size of silica particles pulverized. These characteristics lead to the conclusion that the grey spheres observed should be silica nanoparticles concentrated on the cancerous tissue. A chemical analyze (Energy-dispersive X-ray spectroscopy, for example) seems necessary to confirm these observations

As FIB/SEM is a destructive technique, volume is inevitably consumed during the data collection process (Figure 56).

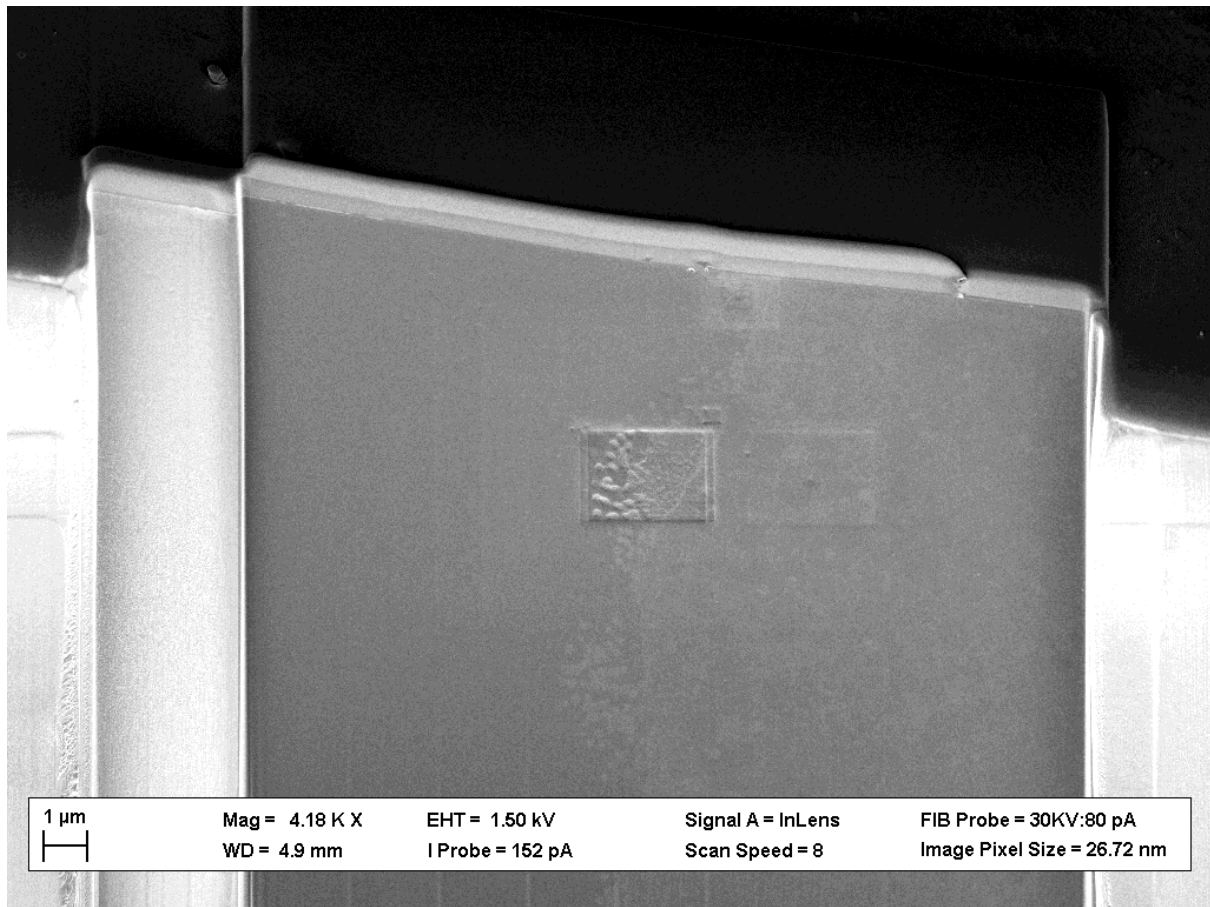


Figure 56: Imaged portions of the sample damaged by electronic irradiation.

4.4 Conclusion of Part Four

In this part, we studied internalization of silica particles of variable size in macrophages *in vitro*. The aim of this study was to determine the impact of the size parameter on cellular uptake and biological activity, working with well-characterized fluorescent particles. They were easily visualized after cellular uptake using confocal and electron microscopy. Size was found to be an important parameter regarding particles uptake and *in vitro* toxicity but this latter strongly depends on the particles doses employed.

For the analyses *ex-vivo* of colectomy with a probe detection of FITC during and after contact times with nanoparticles, validation of observations with epifluorescence may be done using FIB-SEM technique with an active specific accumulation on the tumor tissue. Nevertheless, chemical analyses seem necessary to confirm FIB-SEM observations.

5 General Conclusions and Perspectives

The subject of this thesis is about nanoparticles/living matter interactions and their characterization at a microscopic scale. The main axis of research concerned the study of internalization mechanisms of sub-5nm gadolinium based nanoparticles (GBNs) into cancer cells. It has been shown that the GBNs possess an *in vitro* efficient radiosensitizing effect even at moderate concentration when incubated with SQ20B. To further understand this phenomenon and optimize it, we used different types of microscopy techniques, in particular electron microscopy that possesses a 10 nm resolution sufficient to determine the mechanisms responsible for particles uptake. Two main cellular internalization mechanisms were then evidenced and quantified: passive diffusion and macropinocytosis. Whereas the amount of particles internalized by passive diffusion is hardly sufficient to induce *in vitro* radiosensitization, the cellular uptake by macropinocytosis, significant only in a limited range of GBNs incubation concentration, permits to obtain a clear radiosensitizing effect of the particles. This is true even if macropinocytosis only allows the internalization of agglomerates, which are less efficient radiosensitizing agents than particles since the killing species (Auger electrons and reactive oxygen species) encounter great difficulties to escape from such constructs and then reach the nucleus DNA. Precisely, macropinocytosis processes in two steps: formation of agglomerates at vicinity of the cell followed by their recuperation by the cell lamellipodia (i.e. the cell “arms”). The first step is strongly dependent on the physicochemical characteristics of the particles, especially their isoelectric pH. Indeed it is this value that determines the size of the agglomerates and their distance from the cell, which are the two relevant parameters that render possible their collect *via* the lamellipodia. All these results pose interesting challenges for clinical use of GBNs. They should permit to control the quantity of particles internalized in the cell cytoplasm so promising opportunities towards a particle-assisted radiotherapy using lower doses of radiation.

As the intracellular localization of sensitizers in cells is very important for determining the sensitizing properties of nanoparticles, it would be interesting to measure the distance between nanoparticles and the cell nuclei using a large number of TEM micrographs. An optimized distance from the nuclei may be combined to a given incubation concentration and time. Moreover, it has generally been believed that presence of sensitizers in nucleus gives higher sensitization due to the higher resulting efficiency in producing DNA damage. But recent results suggest that the killing of cells by radiation might be caused by energy deposition in the cytoplasm, mitochondria and the rafts structure in the membrane system

being proposed as the lethal targets. It would be interesting to measure distances separating nanoparticles from cell nuclei, mitochondria and plasmic membrane by exploiting TEM micrographs furthermore. Moreover, studies are beginning to emerge on the impact of nanoparticles internalization related to the cell cycle.^[ccxxi] This parameter appears important and still little studied. It might be interesting to complete our studies by conducting kinetics of internalization of gadolinium nanoparticles over time in parallel with a cell cycle marker type or a synchronized cell line. Thus, it would be possible to determine the proportion of cells in each phase of the cell cycle and whether or not the nanoparticles disrupt this distribution.

In addition, since the fate on nanoparticles in cells appears as an important factor for toxicology studies, checking the state of gadolinium-based nanoparticles and their localization in the cell (in cytoplasm, on membrane, in organelles, in nucleus, etc.) should generate valuable information about the management of the nanoparticles by the cell.

The second main axis of research concerned the effect of physicochemical parameter "size" on the level of internalization and biological toxicity. A range of four sizes of nanoparticles (150, 250, 500 and 850 nm) has been synthesized and characterized. A new methodology for quantification and observation was finally developed and improved over the work put in place for the microparticles. Quantification of internalization has been reproduced with a trypan blue quenching for fluorimetric applications allowing more accurate quantification. The observations were pushed to the intracellular level with the introduction of TEM observations. This work allowed us to note that smaller nanoparticles (150 nm) are internalized in a dose of 1000 NP / cell used. There is no direct relationship between cellular internalization of nanoparticles and biological toxicity. As the literature data concerning the expression of the metric rates to elicit controversy,^{[clxxix][ccx]} it seems necessary for future analysis to work with three metrics. Thus, the doses should be expressed in number, surface and mass so as to be informative as possible. Indeed in this work, the reasoning in number was used because it seemed most relevant for assessing the internalization. However it became much less relevant to compare the biological activity of nanoparticles in the size range 150-850 nm.

Besides the "size" parameter, the surface charge of nanoparticles is a very important parameter that influences nanoparticles uptake by cell. Following encouraging preliminary studies on the parameter "size", a collaborative work will be continued with a new PhD student (Andrea Kurtz-Chalot – Ecole des Mines de Saint Etienne). Standardized silica nanoparticles of a fixed size (40-60 nm), should be charged positively, negatively and with no surface charge. In addition to macrophages, the analyzes should be performed in parallel on dendritic cells in collaboration with the Grenoble team of Dr. Christian Villiers (Institut

Albert Bonniot INSERM / UJF U823) to also take into account the differences in behavior of these two cell types involved in the forefront of interactions with antigen particles. Thus, the objective of this new thesis aims to better understand the interactions between the internalization, the physical chemistry of nanoparticles and their biological activity by taking into account new data (surface charge). Complementary TEM observations should provide additional information at a nanoscale dimension about interactions mechanisms of silica nanoparticles with variable charge surface with macrophages and dendritic cells.

In this context, recent data from the literature on the concept of "corona" emerge and involve taking into account future investigations, in addition to the physicochemical parameters, the adsorption of biomolecules on nanoparticles.^{[ccxx][ccxxii]} The crown of proteins adsorbed on the surface of nanoparticles in biological media (corona) such as the culture medium could alter the charge and therefore the steady state. The development of analysis methods of the effect of the charge of nanoparticles should take account of this important phenomenon in future analyses.

Generally talking, when nanoparticles are applied to theranostic field, the important question is how specific the action of a given compound can be to the target tissue. In cancer treatment for instance, we need to think of the variety of forms of cancer tissue, as well as the modification that chemicals undergo due to metabolism. Moreover, in designing new nanoparticles for medical application, nontoxicity or low toxicity to cells and to the human body is considered to be the top priority. A large risk assessment of nanotechnology must accompany all these new opportunities, as quickly as possible, before committing to commercial interests. Researchers are then rightly empowered on topics such as the potential toxicity of the new created materials. But the impact of these technologies on our lives and the speed at which they shape our societies is such that the debate on their use goes beyond the scientific framework. Scientists have a moral responsibility but they are clearly not entirely responsible for any drift or benefits of nanotechnology in society. The urgency is to construct an explicit project, common to scientists and non-scientists, to decide the place we want to give to these new technologies in our lives and our societies.

In this whirlwind of discussions and debates, let's be careful not to lose sight of the problems where nanotechnology can provide solutions. Nanotechnology is inevitably one of the keys to our future because it is not involved in a single application. It weighs in all areas of our lives: the environment, energy, medicine, communication, etc. Not develop nanotechnology would be foolish. It's so crucial to the future of humanity, bearing in mind our current non-environmental friendly industrial processes.

6 References

- ⁱ Editorial. Why small matters, *Nat. Biotechnol.* **2003**, *21*, 1113.
- ⁱⁱ G. M. Whitesides. The ‘right’ size in nanobiotechnology, *Nat. Biotechnol.* **2003**, *21*, 1161.
- ⁱⁱⁱ www.nano.gov (date of visit: September 25, 2010).
- ^{iv} www.enseignement-recherche.gouv.fr (date of visit: September 25, 2010).
- ^v G. Konstantatos *et al.* Nanostructured materials for photon detection, *Nat. Nanotechnol.* **2010**, *5*, 391.
- ^{vi} M. Urbakh *et al.* Nanotribology : The renaissance of friction, *Nat. Mater.*, **2010**, *9*, 8.
- ^{vii} A. Hernandez-Santana *et al.* Nanolithography : Written with light, *Nature Nanotechnol.*, **2010**, *5*, 629.
- ^{viii} S.K. Sahoo *et al.* The present and the future of nanotechnology in human health care, *Nanomedicine.* **2007**, *3*, 20.
- ^{ix} G. Linazasoro. Potential applications of nanotechnologies to Parkinson’s disease therapy, *Parkinsonism Relat. Disord.*, **2008**, *14*, 383.
- ^x World Cancer Report 2008. World Health Organization. International Agency for Research on cancer, **2008**.
- ^{xi} Projection de l’incidence et de la mortalité par cancer en France en 2011. Rapport Technique. Saint-Maurice: Institut de Veille Sanitaire, **2011**.
- ^{xii} J. Kreuter. Nanoparticles – a historical perspective, *Int. J. Pharm.* **2007**, *331*, 1.
- ^{xiii} V.P. Retel *et al.* Review on early technology assessments of nanotechnologies in oncology, *Molecular Oncology.* **2009**, *3*, 394.
- ^{xiv} Otilia M. Koo *et al.* Role of nanotechnology in targeted drug delivery and imaging: a concise review, *Nanomedicine.* **2005**, *1*, 193.
- ^{xv} J.L. Bridot *et al.* Hybrid gadolinium oxide nanoparticles: multimodal contrast agents for in vivo imaging, *J. Am. Chem. Soc.* **2007**, *129*, 5076.
- ^{xvi} C. Esnouf, Caractérisation Microstructurales des Matériaux – Analyse par les rayonnement X et électronique, METIS Lyon Tech, Presses polytechniques et universitaires romandes, **2011**.
- ^{xvii} L. Marton, La microscopie électronique des objets biologiques. Bull. Classe Sci. Acad. Roy. Belg., Series 5, **20**, 439.
- ^{xviii} B.J. Poiesz *et al.* Isolation of a new type C retrovirus (HTLV) in primary uncultured cells of a patient with Sézary T-cell leukaemia, *Nature* **1981**, *294*, 268.
- ^{xix} J.J. Bozzola and Lonnie D. Russel, Electron Microscopy: Principles and Techniques for Biologists, Second Edition. **1999**, Jones and Bartlett Publishers, Inc. United Kingdom.
- ^{xx} Y. Yun *et al.* Revolutionizing biodegradable metals. *Mater. Today* **2009**, *12*, 22.
- ^{xxi} J.C. Middleton *et al.* Synthetic biodegradable polymers as orthopedic devices, *Biomaterials* **2000**, *21*, 2335.
- ^{xxii} A. Ayrš *et al.* Analysis of titanium dental implants after failure of Osseointegration combined histological electron microscopy and X-ray photoelectron spectroscopy approach, *J. Biomed. Mater. Res.* **1998**, *43*, 300.
- ^{xxiii} C.I. Vamanu *et al.* Induction of cell death by TiO₂ nanoparticles: studies on a human monoblastoid cell line, *Toxicol. In Vitro* **2008**, *22*, 1689.
- ^{xxiv} N. Ae. Understanding biophysicochemical interactions at the nano-bio interface, *Nat. Mater.* **2009**, *8*, 543.
- ^{xxv} J.F. Hillyer *et al.* Gastrointestinal persorption and tissue distribution of differently sized colloidal gold nanoparticles, *J. Pharmacol. Sci.* **2001**, *90*, 1927.
- ^{xxvi} W. Busch *et al.* Internalization of engineered nanoparticles into mammalian cells in vitro: influence of cell type and particle properties, *J. Nanopart. Res.* **2011**, *13*, 293.
- ^{xxvii} S.D. Conner *et al.* Regulated portals of entry into the cell, *Nature* **2003**, *422*, 37.
- ^{xxviii} W. Löscher *et al.* Role of drug efflux transporters in the brain for drug disposition and treatment of brain diseases, *Prog. Neurobiol.* **2005**, *76*, 22.
- ^{xxix} G. Oberdörster *et al.* Nanotoxicology: an emerging discipline evolving from studies of ultrafine particles. *Environ. Health Persp.* **2005**, *113*, 823
- ^{xxx} M. Madlova *et al.* Poly(vinyl alcohol) nanoparticle stability in biological media and uptake in respiratory epithelial cell layers in vitro, *Eur. J. Pharm. Biopharm.* **2009**, *72*, 438.
- ^{xxxi} M. Geiser *et al.* Deposition and biokinetics of inhaled nanoparticles Particle and Fiber, *Toxicology* **2010**, *7*, 2.
- ^{xxxii} E. Smythe *et al.* The mechanism of receptor-mediated endocytosis, *Eur. J. Biochem.* **1991**, *202*, 689.
- ^{xxxiii} H. Hillaireau *et al.* Nanocarriers’ entry into the cell: relevance to drug delivery. *Cell. Mol. Life Sci.* **2009**, *66*, 2873.
- ^{xxxiv} A. Kumari *et al.* Biodegradable polymeric nanoparticles based drug delivery systems, *Colloids Surf., B* **2010**, *75*, 1.
- ^{xxxv} V. Schafer *et al.* Phagocytosis of nanoparticles by HIV-infected macrophage: a possibility for antiviral drug targeting. *Pharm. Res.* **1992**, *9*, 541.

- ^{xxxvi} K.Y. Win *et al.* Effects of particle size and surface coating on cellular uptake of polymeric nanoparticles for oral delivery of anticancer drugs, *Biomaterials* **2005**, *26*, 2713.
- ^{xxxvii} A. Vonarbourg *et al.* Parameters influencing the stealthiness of colloidal drug delivery systems, *Biomaterials* **2006**, *27*, 4356.
- ^{xxxviii} U. Gupta *et al.* Non polymeric nano carriers in HIV AIDS drug delivery and targeting, *Adv. Drug Delivery Rev.* **2010**, *6*, 478.
- ^{xxxix} S.C. Wuang *et al.* Heparinized magnetic nanoparticles in vitro assessment Medical Application, *Adv. Funct. Materials* **2003**, *16*, 1723.
- ^{xl} B.G. Jones *et al.* The inhibition of phagocytosis of respirable microspheres by alveolar and peritoneal macrophages, *Inter. J. Pharm.* **2002**, *236*, 65.
- ^{xli} S. Bauer *et al.* Membrane retrieval in neutrophils during phagocytosis, *J. Leuk. Biol.* **2004**, *76*, 1142.
- ^{xlii} K.T. Thurn *et al.* Endocytosis of titanium dioxide nanoparticles in prostate cancer PC-3M cells. *Nanomedicine* **2011**, *7*, 123.
- ^{xliii} L. Von Kleist *et al.* Role of the clathrin terminal domain in regulating coated pit dynamics revealed by small molecule inhibition. *Cell* **2011**, *146*, 471.
- ^{xliv} F.R. Maxfield *et al.* Endocytic recycling, *Nature Rev. Mol. Cell. Bio.* **2004**, *5*, 121.
- ^{xlv} O. Harush-Frenkel *et al.* Targeting of nanoparticles to the clathrin-mediated endocytic pathway, *Biochem. Biophys. Res. Co.* **2007**, *353*, 26.
- ^{xlvi} Z. Gu *et al.* Cellular trafficking of low molecular weight heparin incorporated in layered double hydroxide nanoparticles in rat vascular smooth muscle cells, *Biomaterials* **2011**, *32*, 7234.
- ^{xlvii} J.H. Choy *et al.* Inorganic layered double hydroxides as nonviral vectors. *Angew. Chem. Int. Ed.* **2000**, *39*, 4042.
- ^{xlviii} J.H. Choy *et al.* Inorganic-biomolecular hybrid nanomaterials as a genetic molecular code system, *Adv. Mater.* **2004**, *16*, 1181.
- ^{xlix} S. Singh *et al.* Endocytosis, oxidative stress and IL-8 expression in human lung epithelial cells upon treatment with fine and ultrafine TiO₂: Role of the specific surface area and of surface methylation of the particles. *Toxic. Appl. Pharmac.* **2007**, *222*, 141.
- ^l J.E. Schnitzer *et al.* Caveolae from basic trafficking mechanisms to targeting transcytosis for tissue-specific drug and gene delivery in vivo, *Adv. Drug Del. Rev.* **2001**, *49*, 265.
- ^{li} L. Pelkmans *et al.* Endocytosis via caveolae, *Traffic* **2002**, *3*, 311.
- ^{lii} L.M. Bareford *et al.* Endocytic mechanisms for targeted drug delivery. *Adv. Drug Deliv. Rev.* **2007**, *59*, 748.
- ^{liii} L. Johannes *et al.* Clathrin-dependent or not is it still the question *Traffic* **2002**, *3*, 443.
- ^{liv} J. Kartenbeck *et al.* Endocytosis of Simian Virus 40 into the Endoplasmic Reticulum, *J. Cell Biol.* **1989**, *109*, 2721.
- ^{lv} E. Dauty *et al.* Intracellular Delivery of nanometric DNA particles via the folate receptor, *Bioconjugate Chem.* **2002**, *13*, 831.
- ^{lvi} C. Liu *et al.* Enhanced gene transfection efficiency in CD13-positive vascular endothelial cells with targeted poly lactic acid - poly ethylene glycol nanoparticles through caveolae-mediated endocytosis, *J. Control. Release.* **2011**, *151*, 162.
- ^{lvii} J.A. Swanson *et al.* Macropinocytosis, *Trends Cell Biol.* **1995**, *5*, 424.
- ^{lviii} K.J. Sandgren *et al.* A differential role for macropinocytosis in mediating entry of the two forms of vaccinia virus into dendritic cells. *PLoS Pathog.* **2010**, *6*, e-1000866.
- ^{lix} M.T. Baldrige *et al.* Inflammatory signals regulate hematopoietic stem cells. *Trends Immunol.* **2011**, *32*, 57.
- ^{lx} D.V. Krysko *et al.* Clearance of apoptotic and necrotic cells and its immunological consequences, *Apoptosis* **2006**, *11*, 1709.
- ^{lxi} S. Falcone *et al.* Macropinocytosis: regulated coordination of endocytic and exocytic membrane traffic events, *J. Cell Sci.* **2006**, *119*, 4758.
- ^{lxii} J. Mercer *et al.* A Virus entry by macropinocytosis, *Nat. Cell Biol.* **2009**, *11*, 510.
- ^{lxiii} R.G. Anderson *et al.* A role for lipid shells in targeting proteins to caveolae, rafts, and other lipid domains. *Science* **2002**, *7*, 1821.
- ^{lxiv} B.J. Nichols *et al.* Endocytosis without clathrin coats, *Trends Cell Biol.* **2011**, *11*, 406.
- ^{lxv} K.C. Partlow *et al.* Exploiting lipid raft transport with membrane targeted nanoparticles a strategy for cytosolic drug delivery, *Biomaterials* **2008**, *29*, 3367.
- ^{lxvi} Y.L. Chiu *et al.* The characteristics cellular uptake and intracellular trafficking of nanoparticles made of hydrophobically modified chitosan, *J. Controlled Release* **2010**, *146*, 152.
- ^{lxvii} H.S. Yoo *et al.* Biodegradable polymeric micelles composed of doxorubicin conjugated PLGA-PEG block copolymer, *J. Controlled Release* **2001**, *70*, 63.
- ^{lxviii} Y. Chen *et al.* Multifunctional Mesoporous Nanoellipsoids for Biological Bimodal Imaging and Magnetically Targeted Delivery of Anticancer Drugs, *Adv. Funct. Mater.* **2010**, *21*, 270.

- ^{lxi} A. Musyanovych *et al.* Criteria impacting the cellular uptake of nanoparticles: a study emphasizing polymer type and surfactant effects, *Acta Biomater.* **2011**, *7*, 4160.
- ^{lxx} M.A. Soler *et al.* Interaction of erythrocytes with magnetic nanoparticles, *J. Nanosci. Nanotechnol.* **2007**, *7*, 1069.
- ^{lxxi} X.L. Xing *et al.* Uptake of silica-coated nanoparticles by HeLa cells, *J. Nanosci. Nanotechnol.* **2005**, *10*, 1688.
- ^{lxxii} N.W. Kam *et al.* Carbon nanotubes as intracellular transporters for proteins and DNA: an investigation of the uptake mechanism and pathway, *Angew. Chem., Int. Ed.* **2006**, *45*, 577.
- ^{lxxiii} J.M. Oh *et al.* Cellular uptake mechanism of an inorganic nanovehicle and its drug conjugates: enhanced efficacy due to clathrin-mediated endocytosis, *Bioconjugate Chem.* **2006**, *17*, 1411.
- ^{lxxiv} N. Lewinski *et al.* Cytotoxicity of nanoparticles, *Small* **2008**, *4*, 26.
- ^{lxxv} S.M. Hussain *et al.* Toxicity Evaluation for safe use of nanomaterials recent achievements and technical challenges, *Adv. Mater.* **2009**, *21*, 1549.
- ^{lxxvi} N.A. Franken *et al.* Clonogenic assay of cells in vitro, *Nat. Protoc.* **2006**, *1*, 2315.
- ^{lxxvii} T.T. Puck *et al.* Action of X-ray on mammalian cells, *J. Exp. Med.* **1956**, *103*, 653.
- ^{lxxviii} D. Banasiak *et al.* Comparison between the clonogenic MTT and SRB assays for determining radiosensitivity in a Panel of Human Bladder Cancer Cell Lines and a Urethral Cell Line, *Radiation Oncology Investigations*, **1999**, *7*, 77.
- ^{lxxix} W. Roa *et al.* Gold nanoparticles sensitize radiotherapy of prostate cancer cells by regulation of the cell cycle, *Nanotechnology* **2009**, *20*, 375101.
- ^{lxxx} S. Bisht *et al.* Polymeric nanoparticle-encapsulated curcumin (nanocurcumin) a novel strategy for human cancer therapy, *Journal of Nanobiotechnology* **2007**, *5*, 3.
- ^{lxxxi} Y. Yamakoshi *et al.* Active oxygen species generated from photoexcited fullerene C60 as potential medicines *J. Am. Chem. Soc.* **2003**, *125*, 12803.
- ^{lxxxii} W.F. Vevers *et al.* Genotoxic and cytotoxic potential of titanium dioxide TiO₂ nanoparticles on fish cells in vitro, *Ecotoxicology* **2008**, *17*, 410.
- ^{lxxxiii} A.A. Shvedova *et al.* Inhalation vs. aspiration of single-walled carbon nanotubes in C57BL-6 mice inflammation fibrosis oxidative stress and mutagenesis, *Am. J. Physiol. Lung Cell Mol. Physiol.* **2008**, *295*, L522.
- ^{lxxxiv} F. Wang *et al.* Oxidative stress contributes to silica nanoparticle-induced cytotoxicity in human embryonic kidney cells, *Toxicol. In Vitro* **2009**, *23*, 808.
- ^{lxxxv} S.J. Soenen *et al.* Cellular toxicity of inorganic nanoparticles common aspects and guidelines for improved nanotoxicity evaluation, *Nano Today* **2011**, *6*, 446.
- ^{lxxxvi} S. Laurent *et al.* Magnetic iron oxide nanoparticles synthesis stabilization vectorization physicochemical characterizations and biological applications, *Chem. Rev.* **2008**, *108*, 2064.
- ^{lxxxvii} N. Li *et al.* Ultrafine particulate pollutants induce oxidative stress and mitochondrial damage, *Environ. Health Perspect.* **2003**, *111*, 455.
- ^{lxxxviii} D.M. Huang *et al.* The promotion of human mesenchymal stem cell proliferation by superparamagnetic iron oxide nanoparticles, *Biomaterials* **2009**, *30*, 3645.
- ^{lxxxix} C.F. Jones *et al.* In vitro assessments of nanomaterial toxicity, *Adv. Drug Delivery Rev.* **2009**, *61*, 438.
- ^{xc} M. Pozzolini *et al.* Interference in MTT cell viability assay in activated macrophage cell line, *Anal. Biochem.* **2003**, *313*, 338.
- ^{xci} R. Pieters *et al.* In vitro drug sensitivity of cells from children with leukemia using the MTT assay with improved culture conditions, *Blood* **1990**, *76*, 2327.
- ^{xcii} T. Mosmann *et al.* Rapid colorimetric assay for cellular growth and survival: application to proliferation and cytotoxicity assays, *J. Immunol. Methods* **1983**, *65*, 55.
- ^{xciii} P. Price *et al.* The use of non-clonogenic assays in measuring the response of cells in vitro to ionizing radiation, *Eur. J. Cancer* **1994**, *30*, 838.
- ^{xciv} S. Lanone *et al.* Comparative toxicity of 24 manufactured nps in human alveolar epithelial and macrophage cell lines, *Part. Fibre Toxicol.* **2009**, *6*, 14.
- ^{xcv} J.Y. Koh *et al.* Quantitative determination of glutamate mediated cortical neuronal injury in cell culture by lactate dehydrogenase efflux assay, *J. Neurosci. Meth.* **1987**, *20*, 83.
- ^{xcvi} A. Kroll *et al.* A Current in vitro methods in nanoparticle risk assessment Limitations and challenges, *Eur. J. Pharm. Biopharm.* **2009**, *72*, 370.
- ^{xcvii} N.A. Riviere-Monteiro *et al.* Limitations and relative utility of screening assays to assess engineered nanoparticle toxicity in a human cell line, *Toxicol. Appl. Pharmacol.* **2009**, *234*, 222.
- ^{xcviii} Y. Ko *et al.* Toxicity of amorphous silica nanoparticles in mouse keratinocytes, *J. Nanopart. Res.* **2009**, *11*, 15.

- ^{xcix} O. Ostling *et al.* Microelectrophoretic study of radiation-induced DNA damages in individual mammalian cells, *Biochem. Biophys. Res. Commun.* **1984**, *123*, 291.
- ^c P. Mowat *et al.* In vitro radiosensitizing effects of ultrasmall gadolinium based particles on tumor cells, *J. Nanosci. Nanotechnol.* **2011**, *11*, 7833.
- ^{ci} J. Fizet *et al.* Multi-luminescent hybrid gadolinium oxide nanoparticles as potential cell labeling, *J. Nanosci. Nanotechnol.* **2009**, *9*, 5717.
- ^{cii} W. Lin *et al.* In vitro toxicity of silica nanoparticles in human lung cancer cells, *Toxicol. Appl. Pharmacol.* **2006**, *217*, 252.
- ^{ciii} B.D. Chithrani *et al.* Determining the size and shape dependence of gold nanoparticles uptake into mammalian cells, *Nano Lett.* **2006**, *6*, 662.
- ^{civ} H.B. Na *et al.* Development of a T1 contrast agent for magnetic resonance imaging using MnO nanoparticles *Angew. Chem.* **2007**, *119*, 5493.
- ^{cv} A. Moore *et al.* Tumoral distribution of long-circulating dextran-coated iron oxide nanoparticles in a rodent model, *Radiology* **2000**, *214*, 568.
- ^{cvi} B.P. Pichon *et al.* Magnetotunable hybrid films of stratified iron oxide nanoparticles assembled by the layer-by-layer technique, *Chem. Mater.* **2011**, *23*, 3668.
- ^{cvi} F. Dilnawaz *et al.* Dual drug loaded superparamagnetic iron oxide nanoparticles for targeted cancer therapy, *Biomaterials* **2010**, *31*, 3694.
- ^{cvi} C.L. Chen *et al.* A new nano-sized iron oxide particle with high sensitivity for cellular magnetic resonance imaging, *Mol. Imaging Biol.* **2011**, *13*, 825.
- ^{cix} M.D. Butterworth *et al.* Preparation of ultrafine silica- and PEG-coated magnetite particles, *Colloids Surf., A* **2001**, *179*, 93.
- ^{cx} W.R. Viali *et al.* Investigation of the molecular surface coating on the stability of insulating magnetic oils, *J. Phys. Chem. C* **2010**, *114*, 179.
- ^{cx} N. Nitin *et al.* Functionalization and peptide-based delivery of magnetic nanoparticles as an intracellular MRI contrast agent, *J. Biol. Inorg. Chem.* **2004**, *9*, 706.
- ^{cxii} J. Lu *et al.* Mesoporous silica nanoparticles as a delivery system for hydrophobic anticancer drugs, *Small* **2007**, *3*, 1341.
- ^{cxiii} M.L. Di Giorgio *et al.* Effects of single and multi walled carbon nanotubes on macrophages: cytotoxicity and electron microscopy. *Mutat. Res.* **2011**, *722*, 20.
- ^{cxiv} A. Simon-Deckers *et al.* In vitro investigation of oxide nanoparticle and carbon nanotube toxicity and intracellular accumulation in A549 human pneumocytes, *Toxicology* **2008**, *253*, 137.
- ^{cxv} K. Soto *et al.* Cytotoxic effects of aggregated nanomaterials, *Acta Biomater.* **2007**, *3*, 351.
- ^{cxvi} M. Knoll and E. Ruska. **1932.** Beitrag zur geometrischen elektronoptik. *Ann. Physik* *12*: 607-61.
- ^{cxvii} J. Ayyache, L. Beaunier, J. Boumendil, G. Ehret G. and L. Daniele L. **2010.** *Sample Preparation Handbook for Transmission Electron Microscopy, Methodology*, New York, Springer Editions, 250 pages.
- ^{cxviii} J. Ayyache, L. Beaunier, J. Boumendil, G. Ehret G. and L. Daniele L. **2010.** *Sample Preparation Handbook for Transmission Electron Microscopy, Techniques*, New York, Springer Editions, 338 pages.
- ^{cxix} A.M. Glauert. **1991.** Epoxy resins: an update on their selection and use. *Microsc. and Analysis*, 12-20.
- ^{cxix} K. Shinohara *et al.* Enhanced killing of HeLa cells pre-labeled with 5-bromodeoxyuridine by monochromatic synchrotron radiation at 0.9 Å: an evidence for Auger enhancement in mammalian cells, *J. Radiat. Res. (Tokyo)* **1985**, *26*, 334.
- ^{cxix} H. Maezawa *et al.* Effects of monoenergetic X-rays with resonance energy of bromine K-absorption edge on bromouracil-labelled E. coli cells, *Int. J. Radiat. Biol. Relat. Stud. Phys. Chem. Med.* **1988**, *53*, 301.
- ^{cxix} D. Larson *et al.* Auger electron contribution to bromodeoxyuridine cellular radiosensitization, *Int. J. Radiat. Oncol. Biol. Phys.* **1989**, *16*, 171.
- ^{cxix} C. Rivière *et al.* *Ann. Chem. Sci. Mater.* Nanosystems for medical applications: Biological detection, drug delivery, diagnosis and therapy, **2006**, *31*, 351.
- ^{cxix} B. Godin *et al.* Emerging applications of nanomedicine for the diagnosis and treatment of cardiovascular diseases, *Trends Pharmacol. Sci.* **2010**, *31*, 199.
- ^{cxix} S.K. Hobbs *et al.* Regulation of transport pathways in tumor vessels: Role of tumor type and microenvironment, *Proc. Natl. Acad. Sci. U.S.A.* **1998**, *95*, 4607.
- ^{cxix} H. Maeda *et al.* Vascular permeability enhancement in solid tumor: various factors, mechanisms involved and its implications, *Int. Immunopharmacol.* **2003**, *3*, 319.
- ^{cxix} M. Ferrari. Cancer nanotechnology: opportunities and challenges, *Nat. Rev. Cancer* **2005**, *5*, 161.
- ^{cxix} M. Lewin *et al.* Tat peptide-derivatized magnetic nanoparticles allow in vivo tracking and recovery of progenitor cells, *Nat. Biotechnol.* **2000**, *18*, 410.
- ^{cxix} J. Kim *et al.* Multifunctional nanostructured materials for multimodal imaging, and simultaneous imaging and therapy, *Chem. Soc. Rev.* **2009**, *38*, 372.

- ^{cxxx} K. Kobayashi *et al.* Enhancement of radiation effect by heavy elements, *Mutat. Res., Rev. Mutat. Res.* **2010**, *704*, 123.
- ^{cxxxi} C. Alric *et al.* Gadolinium chelate coated gold nanoparticles as contrast agents for both X-ray computed tomography and magnetic resonance imaging, *J. Am. Chem. Soc.* **2008**, *130*, 5908.
- ^{cxxxii} J.F. Hainfeld *et al.* The use of gold nanoparticles to enhance radiotherapy in mice, *Phys. Med. Biol.* **2004**, *49*, 309.
- ^{cxxxiii} J.F. Hainfeld *et al.* Radiotherapy enhancement with gold nanoparticles, *J. Pharm. Pharmacol.* **2008**, *60*, 977.
- ^{cxxxiv} P. Sharma *et al.* Gd nanoparticulates: from magnetic resonance imaging to neutron capture therapy, *Adv. Powder Technol.* **2007**, *18*, 663.
- ^{cxxxv} G. Le Duc *et al.* Toward an Image-Guided Microbeam Radiation Therapy Using Gadolinium-Based Nanoparticles, *ACS Nano* **2011**, *5*, 9566.
- ^{cxxxvi} G. Le Duc, *et al.* French Patent, n° 07.58348, **2007**.
- ^{cxxxvii} F. Lux *et al.* Ultrasmall Rigid Particles as Multimodal Probes for Medical Applications, *Agew. Chem. Int. Ed.* **2011**, *50*, 12299.
- ^{cxxxviii} P. Xu *et al.* Intracellular Drug Delivery by Poly(lactic-co-glycolic acid) Nanoparticles, Revisited, *Mol. Pharm.* **2009**, *6*, 190.
- ^{cxxxix} A. Kumari *et al.* Cellular interactions of therapeutically delivered nanoparticles, *Expert Opin. Drug Delivery* **2011**, *8*, 141.
- ^{cxl} Z. Wang *et al.* Size and dynamics of caveolae studied using nanoparticles in living endothelial cells, *ACS Nano* **2009**, *3*, 4110.
- ^{cxli} S. Dufort *et al.* Physico-chemical parameters that govern nanoparticles fate also dictate rules for their molecular evolution, *Adv. Drug Delivery Rev.* **2012**, *64*, 179.
- ^{cxlii} H. Meng *et al.* Aspect ratio determines the quantity of mesoporous silica nanoparticle uptake by a small GTPase-dependent macropinocytosis mechanism, *ACS Nano* **2011**, *5*, 4434.
- ^{cxliii} H.S. Yoo *et al.* Biodegradable polymeric micelles composed of doxorubicin conjugated PLGA-PEG block copolymer, *J. Control. Release* **2001**, *70*, 63.
- ^{cxliv} T.M. Johnson *et al.* Squamous cell carcinoma of the skin (excluding lip and oral mucosa), *J. Am. Acad. Dermatol.* **1992**, *26*, 467.
- ^{cxlv} Z. Salehi *et al.* Significance of eIF4E expression in skin squamous cell carcinoma, *Cell. Biol. Int.* **2007**, *31*, 1400.
- ^{cxlvi} H.S. Choi *et al.* Design considerations for tumour-targeted nanoparticles, *Nat. Nanotechnol.* **2010**, *5*, 42.
- ^{cxlvii} B. Mutelet *et al.* Size-induced effect upon the Neel temperature of the antiferro/paramagnetic transition in gadolinium oxide nanoparticles, *Appl. Phys. A: Mater. Sci. Process.* **2011**, *15*, 215.
- ^{cxlviii} H. Lodish *et al.* in *Molecular Cell Biology*, 5th ed. (Eds. W.H. Freeman and Company), United States of America, New York, **2004**, pp. 657-935.
- ^{cxlix} L. Sancey *et al.* Clustering and internalization of integrin alphavbeta3 with a tetrameric RGD-synthetic peptide, *Mol. Ther.* **2009**, *17*, 837.
- ^{cl} P. Watson *et al.* Intracellular trafficking pathways and drug delivery: fluorescence imaging of living and fixed cells, *Adv. Drug Delivery Rev.* **2005**, *57*, 43.
- ^{cli} F.R. Maxfield *et al.* Endocytic recycling, *Nat. Rev., Mol. Cell Biol.* **2004**, *5*, 121.
- ^{clii} M. Edidin. Shrinking patches and slippery rafts: scales of domains in the plasma membrane, *Trends Cell Biol.* **2001**, *11*, 492.
- ^{cliii} M. T. Aloy *et al.* Protective role of Hsp27 protein against gamma radiation-induced apoptosis and radiosensitization effects of Hsp27 gene silencing in different human tumor cells, *Int. J. Radiation Oncology Biol. Phys.* **2008**, *70*, 543.
- ^{cliv} A. G. Cuenca *et al.* Emerging implications of nanotechnology on cancer diagnostics and therapeutics, *Cancer* **2006**, *107*, 459.
- ^{clv} S. H. Cho *et al.* The dosimetric feasibility of gold nanoparticle-aided radiation therapy (GNRT) via brachytherapy using low-energy gamma-/x-ray sources, *Phys. Med. Biol.* **2009**, *54*, 4889.
- ^{clvi} F. Van den Heuvel *et al.* Beam energy considerations for gold nano-particle enhanced radiation treatment, *Phys. Med. Biol.* **2010**, *55*, 4509.
- ^{clvii} J.F. Hainfeld *et al.* Gold nanoparticles enhance the radiation therapy of a murine squamous cell carcinoma, *Phys. Med. Biol.* **2010**, *55*, 3045.
- ^{clviii} S. Roux *et al.* Multifunctional nanoparticles: from the detection of biomolecules to the therapy, *Int. J. Nanotechnol.* **2010**, *7*, 781.
- ^{clix} A. R. Collins. The comet assay for DNA damage and repair: principles, applications, and limitations *Mol. Biotechnol.* **2004**, *26*, 249.
- ^{clx} A. Yacoub *et al.* Melanoma differentiation-associated 7 (interleukin 24) inhibits growth and enhances

- radiosensitivity of glioma cells in vitro and in vivo, *Clin. Cancer Res.* **2003**, *9*, 3272.
- ^{clxi} K.E. Hovinga *et al.* Radiation-enhanced vascular endothelial growth factor (VEGF) secretion in glioblastoma multiforme cell lines--a clue to radioresistance? *J. Neurooncol.* **2005**, *74*, 99.
- ^{clxii} H. F. Li *et al.* Radiation-induced Akt activation modulates radioresistance in human glioblastoma cells, *Radiat Oncol.* **2009**, *4*, 43.
- ^{clxiii} P.L. Olive. The comet assay. An overview of techniques, *Methods Mol Biol.* **2002**, *203*, 179.
- ^{clxiv} J. Carmichael *et al.* Evaluation of a tetrazolium-based semiautomated colorimetric assay: assessment of radiosensitivity, *Cancer Res.* **1987**, *47*, 936.
- ^{clxv} F. Shikata *et al.* In vitro cellular accumulation of gadolinium incorporated into chitosan nanoparticles designed for neutron-capture therapy of cancer, *Eur. J. Pharm. Biopharm.* **2002**, *53*, 57.
- ^{clxvi} C. L. Tseng *et al.* Gadolinium hexanedione nanoparticles for stem cell labeling and tracking via magnetic resonance imaging, *Biomaterials.* **2010**, *31*, 5427.
- ^{clxvii} T. Kong *et al.* Enhancement of radiation cytotoxicity in breast-cancer cells by localized attachment of gold nanoparticles, *Small* **2008**, *9*, 1537.
- ^{clxviii} A. Luciani *et al.* Magnetic targeting of iron-oxide-labeled fluorescent hepatoma cells to the liver, *Eur Radiol.* **2009**, *9*, 1087.
- ^{clxix} Z. Zhang *et al.* Superparamagnetic iron oxide nanoparticle-labeled cells as an effective vehicle for tracking the GFP gene marker using magnetic resonance imaging, *Cytotherapy* **2009**, *11*, 43.
- ^{clxx} K. K. Liu *et al.* Endocytic carboxylated nanodiamond for the labeling and tracking of cell division and differentiation in cancer and stem cells, *Biomaterials* **2009**, *30*, 4249.
- ^{clxxi} K. Jihyun *et al.* Comparison of stability of WSiX/SiC and Ni/SiC Schottky rectifiers to high dose gamma-ray irradiation, *Appl. Phys. Lett.* **2008**, *84*, 371.
- ^{clxxii} X.D. Zhang *et al.* Irradiation stability and cytotoxicity of gold nanoparticles for radiotherapy, *Int. J. Nanomedicine* **2009**, *4*, 165.
- ^{clxxiii} R. Okayasu *et al.* Repair of DNA damage induced by accelerated heavy ions in mammalian cells proficient and deficient in the non-homologous end-joining pathway, *Radiat. Res.* **2006**, *165*, 59.
- ^{clxxiv} R. Pathak *et al.* Response to high LET radiation 12C (LET, 295 keV/microm) in M5 cells, a radio resistant cell strain derived from Chinese hamster V79 cells, *Int. J. Radiat. Biol.* **2007**, *83*, 53.
- ^{clxxv} R. Pathak *et al.* Cell killing, nuclear damage and apoptosis in Chinese hamster V79 cells after irradiation with heavy-ion beams of (16)O, (12)C and (7)Li, *Mutat. Res.* **2007**, *632*, 58.
- ^{clxxvi} J. F. Ward. The complexity of DNA damage: relevance to biological consequences, *Int. J. Radiat. Biol.* **1994**, *66*, 427.
- ^{clxxvii} Yuan Yuan *et al.* Size-mediated cytotoxicity and apoptosis of hydroxyapatite nanoparticles in human hepatoma HepG2 cells. *Biomaterials* **2008**, *31*, 730.
- ^{clxxviii} D.B. Warheit *et al.* Comparative pulmonary toxicity assessment of single-wall carbon nanotubes in rats, *Toxicol. Sci.* **2004**, *77*, 117.
- ^{clxxix} G. Oberdorster *et al.* Nanotoxicology: an emerging discipline evolving from studies of ultrafine particles. *Environ. Health Perspect.* **2005**, *113*, 823.
- ^{clxxx} C.M. Sayes *et al.* Assessing toxicity of fine and nanoparticles: comparing in vitro measurements to in vivo pulmonary toxicity profiles, *Toxicol. Sci.* **2007**, *97*, 163.
- ^{clxxxii} P. Haberzettl *et al.* Actin plays a crucial role in the phagocytosis and biological response to respirable quartz particles in macrophages, *Arch. Toxicol.* **2007**, *81*, 459.
- ^{clxxxiii} M.J. Clift *et al.* The impact of different nanoparticle surface chemistry and size on uptake and toxicity in a murine macrophage cell line, *Toxicol. Appl. Pharmacol.* **2008**, *232*, 418.
- ^{clxxxiv} A. Aderem *et al.* Mechanisms of phagocytosis in macrophages, *Annu. Rev. Immunol.* **1999**, *17*, 593.
- ^{clxxxv} G. Fenteany *et al.* Cytoskeletal remodeling in leukocyte function, *Curr. Opin. Hematol.* **2004**, *11*, 15.
- ^{clxxxvi} F. Niedergang *et al.* Signaling and membrane dynamics during phagocytosis: many roads lead to the phagos(R)ome, *Curr. Opin. Cell Biol.* **2004**, *16*, 422.
- ^{clxxxvii} F. Niedergang *et al.* Regulation of phagocytosis by Rho GTPases, *Curr. Top. Microbiol. Immunol.* **2005**, *291*, 43.
- ^{clxxxviii} J. Ravetch *et al.* Phagocytic cells, *Immunol. Rev.* **2007**, *219*, 5.
- ^{clxxxix} R.E. Serda *et al.* Quantitative mechanics of endothelial phagocytosis of silicon microparticles, *Cytometry A* **2009**, *75*, 752.
- ^{clxxxix} B. Fubini. Surface chemistry and quartz hazard, *Ann. Occup. Hyg.* **1998**, *42*, 521.
- ^{exc} B. Fubini *et al.* Relationship between the state of the surface of four commercial quartz flours and their biological activity in vitro and in vivo, *Int. J. Hyg. Environ. Health.* **2004**, *207*, 89.
- ^{exci} M.J. Clift *et al.* The impact of different nanoparticle surface chemistry and size on uptake and toxicity in a murine macrophage cell line. *Toxicol. Appl. Pharmacol.* **2008**, *232*, 418.

- ^{excii} J. Rejman *et al.* Size-dependent internalization of particles via the pathways of clathrin- and caveolae-mediated endocytosis, *Biochem. J.* **2004**, *377*, 159.
- ^{exciii} Y. Hu *et al.* Effect of PEG conformation and particle size on the cellular uptake efficiency of nanoparticles with the HepG2 cells, *J. Control. Release* **2007**, *118*, 7.
- ^{exciv} Y. Su *et al.* Cellular uptake and cytotoxic evaluation of fullerene in different cell lines, *Toxicology* **2010**, *269*, 155.
- ^{excv} F. Yan *et al.* The effect of poloxamer 188 on nanoparticle morphology, size, cancer cell uptake, and cytotoxicity, *Nanomedicine* **2010**, *6*, 170.
- ^{excvi} M.M. Song *et al.* Cytotoxicity and cellular uptake of iron nanowires. *Biomaterials* **2010**, *31*, 1509.
- ^{excvii} J. Hed *et al.* The use of fluorescence quenching in flow cytometry to measure the attachment and ingestion phases in phagocytosis in peripheral blood without prior cell separation, *J. Immunol. Methods* **1987**, *101*, 119.
- ^{excviii} E.S. Van Amersfoort *et al.* Evaluation of a flow cytometric fluorescence quenching assay of phagocytosis of sensitized sheep erythrocytes by polymorphonuclear leukocytes, *Cytometry* **1994**, *17*, 294.
- ^{excix} L. Thiele *et al.* Evaluation of particle uptake in human blood monocyte-derived cells in vitro. Does phagocytosis activity of dendritic cells measure up with macrophages? *J. Control. Release* **2001**, *76*, 59.
- ^{cc} J. Nuutila *et al.* Flow cytometric quantitative determination of ingestion by phagocytes needs the distinguishing of overlapping populations of binding and ingesting cells, *Cytometry A* **2005**, *65*, 93.
- ^{ccj} I. Catelas *et al.* Cytotoxicity and macrophage cytokine release induced by ceramic and polyethylene particles in vitro, *J. Bone Joint. Surg. Br.* **1999**, *81*, 516.
- ^{ccij} K. Donaldson *et al.* The pulmonary toxicology of ultrafine particles, *J. Aerosol. Med.* **2002**, *15*, 213.
- ^{cciii} J. Bruch *et al.* Variation of biological responses to different respirable quartz flours determined by a vector model, *Int. J. Hyg. Environ. Health* **2004**, *207*, 203.
- ^{cciv} C.M. Sayes *et al.* Assessing toxicity of fine and nanoparticles: comparing in vitro measurements to in vivo pulmonary toxicity profiles, *Toxicol. Sci.* **2007**, *97*, 163.
- ^{ccv} A. Van Blaaderen *et al.* Synthesis and characterization of colloidal dispersions of fluorescent, monodisperse silica spheres, *Langmuir* **1992**, *8*, 2921.
- ^{ccvi} W. Wang *et al.* Fabrication of Two- and Three-Dimensional Silica Nanocolloidal Particle Arrays, *J. Phys. Chem. B* **2003**, *107*, 3400.
- ^{ccvii} L. Leclerc *et al.* Quantification of microsized fluorescent particles phagocytosis to a better knowledge of toxicity mechanisms, *Inhal. Toxicol.* **2010**, *22*, 1091.
- ^{ccviii} F. Ahsan *et al.* Targeting to macrophages: role of physicochemical properties of particulate carriers--liposomes and microspheres--on the phagocytosis by macrophages, *J. Control. Release* **2002**, *79*, 29.
- ^{ccix} B. Fubini *et al.* Physico-chemical features of engineered nanoparticles relevant to their toxicity, *Nanotoxicology* **2010**, *4*, 347.
- ^{ccx} D.B. Warheit. Debunking Some Misconceptions about Nanotoxicology, *Nano Lett.* **2010**, *10*, 4777.
- ^{ccxi} S.E. Gratton *et al.* The effect of particle design on cellular internalization pathways, *Proc. Natl. Acad. Sci. U. S. A.* **2008**, *105*, 11613.
- ^{ccxii} F. Castellano *et al.* Actin dynamics during phagocytosis, *Semin. Immunol.* **2001**, *13*, 347.
- ^{ccxiii} S. Etienne-Manneville *et al.* Rho GTPases in cell biology, *Nature* **2002**, *420*, 629.
- ^{ccxiv} F. Niedergang *et al.* Signaling and membrane dynamics during phagocytosis: many roads lead to the phagosome, *Curr. Opin. Cell. Biol.* **2004**, *16*, 422.
- ^{ccxv} F. Niedergang *et al.* Regulation of phagocytosis by Rho GTPases, *Curr. Top. Microbiol. Immunol.* **2005**, *291*, 43.
- ^{ccxvi} P. Haberzettl *et al.* Actin plays a crucial role in the phagocytosis and biological response to respirable quartz particles in macrophages, *Arch. Toxicol.* **2007**, *81*, 459.
- ^{ccxvii} L. Lanzetti. Actin in membrane trafficking, *Curr. Opin. Cell. Biol.* **2007**, *19*, 453.
- ^{ccxviii} T. Yeung *et al.* Lipid signaling and the modulation of surface charge during phagocytosis, *Immunol. Rev.* **2007**, *219*, 17.
- ^{ccxix} J.A. Champion *et al.* Role of Particle Size in Phagocytosis of Polymeric Microspheres, *Pharm. Res.* **2008**, *25*, 1815.
- ^{ccxx} M. Lundqvist *et al.* Nanoparticle size and surface properties determine the protein corona with possible implications for biological impacts, *Proc. Natl. Acad. Sci. U.S.A.* **2008**, *105*, 14265.
- ^{ccxxi} Y. Su *et al.* Cellular uptake and cytotoxic evaluation of fullerene in different cell lines, *Toxicology* **2010**, *269*, 155.
- ^{ccxxii} I. Lynch *et al.* The nanoparticle-protein complex as a biological entity; a complex fluids and surface science challenge for the 21st century. *Adv. Colloid. Interface. Sci.*, **2007**, *134*, 167.